# Biosignature detection in Mars analogue aqueous alteration minerals using Raman spectroscopy

David Hamilton

A Thesis submitted to the Faculty of Graduate Studies in Partial Fulfillment of the Requirements for the Degree of Master of Science

Graduate Program in Earth and Space Science, York University, Toronto, Ontario

August 2016

# Abstract

The Mars Exploration Program Analysis Group states in their documentation regarding science goals, objectives, investigations and priorities, that the number one goal of Mars exploration is to determine if Mars ever supported life[1]. A Raman spectrometer is suggested to be a prime candidate instrument for the detection of organic compounds[2], the building blocks of terrestrial life. Though Raman spectroscopy has no space heritage, both NASA and ESA have Raman instruments planned for their next Mars rovers. The ideal place to search for organic matter which could provide evidence for past or present life would be in the presence of minerals that were formed in water. This study was carried out to determine if a molecular biosignature can be detected in a mixture with either a phyllosilicate or a hydrated sulphate. We present this data at UV excitation wavelength using a prototype in-situ stand off Raman system intended to represent an instrument for a rover platform. Data is also presented for the same samples using green excitation wavelength and a commercial Raman microscope. The spectral resolution of the short focal length prototype in-situ UV Raman system leads to less numerous bands than the green Raman microscope system. Ultraviolet electronic absorption transitions in the samples containing transition metals, either as part of a mineral's crystal structure or as impurities, result in no Raman spectra from the minerals and poor or limited detection of the organic. Only the synthetic calcium sulphate dihydrate, which contains no transition metals, allowed for both acquisition of the mineral spectrum and detection of the embedded biosignature at all concentrations tested using either excitation wavelength. Certain samples allowed for the detection of an organic through the observation of a C-H stretching vibration, but did not provide enough clear peaks to define which organic was present.

## Acknowledgments

I offer my gratitude to my supervisor Professor Mike Daly for his advice and support. I would like to thank Kim Tait, Ed Cloutis, Matt Izawa, Veronica Di Cecco, Brendt Hyde, and Evan Eshelman for being extremely helpful throughout this project. I would also like to thank NSERC for funding a portion of this research.

# Table of Contents

# Contents

# List of Tables

# List of Figures

# 1 Introduction

## 1.1 The ingredients for life on Mars

Our understanding of Mars and the geology present there has increased dramatically over the past 12 years with three successful rover missions. Martian geologic history suggests a past of warmer and wetter climates capable of supporting life [10]. The current barometric and thermal conditions on Mars indicate a higher probability of that planet harbouring life than any other planet in our solar system besides Earth.

Terrestrial life requires liquid water, amino acids, and chemical disequilibrium. Due to the presence of aqueous alteration minerals and fluvial geomorphological features on Mars, confirmed by robotic missions, we know that liquid water existed on the surface at some point. Examinations of Martian meteorites have shown that prebiotic amino acids may have existed on Mars [11]. Chemical disequilibrium can occur as long as there are oxidizing agents present which is obvious given the rusty colour of Mars. However, we note that untapped chemical disequilibrium may be indicative of no biosphere [12]. Since life also requires energy, searching for signs of life where the mineralogy was formed in hot water could optimize our search potential as the presence of these minerals confirms that at some point there was also a heat source. NASA uses the motto "follow the water" when deciding where to explore for signs of life or habitable environments. The ExoMars team has stated that their second goal after searching for life is describing water-related processes. This includes the identification of mineral phases produced by fluid-rock interactions[13].

Since all of these known required factors for life were present on Mars at some point, there exists the possibility that there has been life. Evolution allows organisms to adapt to survive under extreme conditions. Therefore, the conditions under which life can exist could be much more harsh than those under which life could arise. If Mars had a past warmer and wetter climate which allowed life to form, evolution may have caused life to adapt to the harsh present day Martian environment.

Recently it has been found that liquid water currently exists for short periods on Mars in the form of brines[14]. These are salt solutions that lower the freezing point of water such that liquid water could exist temporarily at Martian surface atmospheric conditions. It is hypothesized that narrow streaks which emanate out of the walls of craters on Mars, called recurring slope lineae, are actually formed by liquid brine flowing downhill.

Microorganisms often exist in sediment pore spaces. It is theorized that hydrodynamic sorting which occurs in fluvial environments could concentrate organic carbon into organic rich sections of the sedimentary layers [15]. Martian exploration for preserved signs of microbial life should therefore focus on sedimentary strata. Ancient hydrothermal systems would also be good places to search for signs of life.

The detection of life beyond Earth, either extant and extinct, would have both scientific and philosophical implications. As humans explore more extreme

environments on Earth, we are constantly finding life in places scientists had thought too harsh to habour life [16, 17]. These discoveries expand our understanding of possible lifeforms and in the process, expand our understanding of both biology and geochemistry. Finding evidence of life on Mars would surely motivate further inquiries to understand how that life functions and would also motivate more studies to look for life on other planetary bodies.

In this study we ask questions including *"can we detect a biosignature in Mars analogue aqueous alteration minerals using Raman spectroscopy"?* If so, *"in which of these minerals is that biosignature most easily detected"?* Finally, knowing which excitation wavelengths are planned for upcoming Mars Raman spectrometers, *"should we expect a preferred wavelength for biosignature detection in Mars analogue aqueous alteration minerals"?*

There have been multiple robotic missions to Mars as landers, rovers, and orbiters. These missions have had the primary goals of understanding Martian geology and habitability. The landers and rovers have had an assortment of experiments to study important questions via laser induced breakdown spectroscopy, x-ray fluorescence, gas chromatography, x-ray diffraction, Mossbauer spectroscopy, and alpha particle x-ray spectroscopy, among many others. Previously, mass spectroscopy was the main technique used for detection of organic molecules. However, an instrument which has been suggested to be an optimal technique for detecting organic molecules in-situ, a Raman spectrometer[2, 18], has yet to be deployed to Mars. The European Space Agency's ExoMars mission intends to send a Raman spectrometer in 2020[13] and the National Aeronautics and Space Administration also has a rover planned for the Mars 2020 mission which will have two Raman spectrometers on board, each with a different excitation wavelength[19].

Raman scattering is an inelastic event between light and matter. The difference in energy between the incident and scattered photon corresponds to an excited vibrational state in a molecule or crystal. It only occurs when a molecular vibration induced by an incident electric field causes a change in the polarizability of the electron cloud around the molecule or crystal. Chapter two will provide greater detail about the Raman scattering effect.

Raman spectra are unique for every molecule and mineral and therefore provide a fingerprint for identification. The spectral information obtained by the instrument (number of peaks, peak positions, breadths of peaks, and the peak relative intensities) is related to the composition and structure of a compound. It is the constituent atoms of a molecule, their geometries, and strengths of their bonds that define the quantized vibrational states to which they may be excited, and thus, their resulting Raman spectrum. Stronger bonds have higher energy vibrations. For example, C=C bonds have higher energy vibrations than C-C bonds.

The reason why Raman spectroscopy is suggested to be the best method to detect organic molecules in-situ is because the quantum mechanics of Raman scattering leads to high intensity bands for molecular vibrations of covalent bonds. These electron sharing bonds make up most bonds in organic compounds. Raman scattering intensity is proportional to the square of a change

in the polarizability of a molecule with respect to the vibrational coordinates induced by an incident electromagnetic wave. In a covalent bond, the electrons are held less tightly by each atom and therefore the electron cloud is more easily distorted by incident light (more polarizable).

Minerals with structural or adsorbed water are not easily identified with IR absorption spectroscopy because water has intense IR absorption due to its polarity and has broad absorption bands due to hydrogen bonding. However, water content does not hinder the ability of a UV or VIS Raman system to identify minerals. Raman peaks are usually sharper and the vibrational frequencies of water are not in the same region of the Raman window that is used for fingerprinting minerals. Due to this, Raman spectroscopy can be used for aqueous solutions and would therefore be a great tool for investigating the brines mentioned above. Note that a Raman window refers to the portion of the spectrum in which these vibrations occur. This region is from greater than zero Raman shift up to approximately 4000 $cm^{-1}$. Only the Raman shift for the stretch of hydrogren gas is greater than that.

This Raman study was conducted between the summer of 2014 and the spring of 2016 at the Planetary Exploration Instrumentation Laboratory at York University (Toronto, Canada) under the supervision of Dr. Michael Daly. This study was done with guidance from Dr. Ed Cloutis, whose Planetary Spectrophotometer Facility at the University of Winnipeg (Winnipeg, Canada) provided ultraviolet and visual spectral reflectance data (chapter 7). Raman data was also collected at the mineralogy laboratory at the Royal Ontario Museum (Toronto, Canada) under the guidance of Dr. Kim Tait.

## 1.2 Motivation to utilize UV and green excitation wavelengths

The ExoMars mission has decided on green excitation (RLS Raman Spectrometer) [13], while the Mars 2020 mission has decided on both green (SuperCam) and UV (SHERLOC) excitations [19]. This study used both green and UV lasers to simulate the upcoming missions. However, the green Raman system used is not representative of what would be achievable for a Mars rover platform due to its size, weight, and power requirements. This study used a UV excitation wavelength of 266 nm, while the NASA UV Raman spectrometer will use 248.6 nm[20]. These are close, but may have slight differences in absorption. Also, there is a resonance effect in target organics using 248.6 nm which will not be discussed here. Our investigations with green excitation were done using a 532 nm laser which is the same wavelength selected for both the ESA and NASA missions. More details on the Raman instruments selected for Mars are located in the appendices of this study.

There are both theoretical and practical reasons for selecting a particular excitation wavelength. In the gaseous state, Raman scattering from a molecule is proportional to the fourth power of the excitation frequency. Therefore, UV Raman systems should be better than VIS Raman and much better than NIR Raman. However, once a molecule is in a solid state, the penetration depth

of the incident light becomes important. Near infrared light penetrates deeper than visible light and much deeper than ultraviolet light. Since Raman scattering intensity is proportional to the number of scatterers, deeper penetration means more Raman scattered light. Combining these two factors, it has been determined that a green excitation wavelength, which is approximately in the middle of the visible region, has the highest intensity Raman scattering for minerals in the solid state[21]. Unfortunately, unwanted fluorescence in the visible region can be significantly stronger than the Raman scattering. Therefore, in spite of the low penetration depth with a UV laser, there has been a push to move into the deep UV to avoid the fluorescence [2]. Besides penetration depth, there are also issues in the ultraviolet as a result of electronic absorptions in transition metal complexes. These phenomena are investigated in detail in chapter 7. Since many important target Mars minerals contain iron, the use of UV Raman maybe be hindered on Mars.

When Raman data is returned to Earth from the upcoming missions, this current study may guide researchers in interpreting the results. This study may also be a guide for mission planners deciding on which aqueous alteration minerals to focus their efforts. Finally, though the exploration target of this study was Mars, aqueous alteration minerals have been discovered on other planetary bodies such as the dwarf planet Ceres [22] and organic compounds have been found on others such as the Saturnian moon Titan [23]. It is hoped that the information presented in this thesis guides many astrobiology investigations in the coming years.

## 1.3 Scope and limitations of study

Though there are many molecular biosignatures which could be relevant to Martian astrobiology, this study only examines stearic acid. The reasons for selecting this biosignature are described in chapter 5.

There are many aqueous alteration minerals on Mars, however, only those that satisfy a minimum of two of the following qualities were examined:

-*may have* played important role while life arose from non-living matter (i.e. montmorillonite)[24];

-good at preservation of organic material from harsh environments (i.e. sulphates, clays)[25, 26, 15];

-is used in metabolic processes of microorganisms (i.e. nontronite)[27]; and,

-is present in vast amounts on the surface of Mars (i.e. sulphates, clays)[28, 29, 30, 31].

Precise limits of detection of a biosignature within a mineral matrix may be achievable if that was the primary focus of a study. This study, though quantitative in many aspects, has overall qualitative goals of determining *if* a biosignature can be detected in aqueous alteration minerals, and if so, *in which* minerals does this detection occur most easily.

Finally, even though this study used both green and UV excitation wavelengths, they were not used on equivalent instruments. Directly comparing the

data obtained from each of these systems may not be a fair representation of actual green and UV Raman studies on Mars. Longer focal lengths result in greater resolution. The focal length of the green system is 800 mm, while that of the UV system is only 163 mm. Also, the components making up the green Raman system are too heavy, too large, and require too much power to be incorporated into a rover platform.

## 2 Raman scattering: The classical description

When an incident photon is scattered from a molecule, the scattering event can be either elastic or inelastic. In an elastic event, known as Rayleigh scattering, the scattered photon is the same energy as the incident photon. This means that no lasting energy is transferred to the molecule during the scattering event. Conversely, during the inelastic event, the scattered photon has either greater or less energy than the incident photon. The probability of an inelastic event occurring is low at approximately one in $10^6$ to one in $10^9$ scattering events for solid samples.

If the energy of a scattered photon is less than that of the incident photon, the energy lost by the photon and transferred to the molecule causes the molecule to enter an excited vibrational state. This is known as Stokes Raman scattering. If the energy of the scattered photon is greater than that of the incident photon, the energy gained by the photon (transferred from the molecule) causes the molecule to drop from an excited vibrational state back down to a ground state. This second scenario is known as anti-Stokes Raman scattering. The relationship between stokes and anti-stokes intensities is given by an exponential Boltzmann factor. It is only when the ambient temperature of a Raman experiment is extremely high that anti-stokes scattering is of any significance. This study and the two upcoming Mars rover missions will only examine Stokes scattering as anti-Stokes scattering would be insignificant at Martian temperatures (~140K-300K).

It is standard to refer to the shift in photon energy in terms of the change in wavenumber (units of $cm^{-1}$) since energy and absolute wavenumber are linearly proportional. That is, the energy is of a photon is equal to the product of Planck's constant, the speed of light, and the wavenumber. The change in wavenumber, called the Raman shift and shown symbolically as $\tilde{\nu}$, is related to excitation and scattered wavelengths (in nm) as follows:

$$\tilde{\nu} = 10^7 \cdot \left(\frac{1}{\lambda_{excitation}} - \frac{1}{\lambda_{scattered}}\right) \tag{1}$$

Raman scattering is not instantaneous. For a short period of time, the incident photon is absorbed by the molecule, promoting the molecule to a quantum 'virtual state' before re-radiating a wavelength shifted photon and leaving the molecule in a changed vibrational state. Figure 1 shows how Raman scattering differs from other photon-matter interactions. It is important to note that the incident photon energy is much greater than that of the quantized vibrational energy. It is also worth noting that the virtual state is not observable and that it is not possible to directly measure the energy or lifetime of the virtual state.

Since Raman scattering is directly related to molecular vibrations, a Raman spectrum can be analyzed to provide molecular level structural and dynamic information. Each molecule has different constituent atoms which have different masses. Each molecule also has different geometries forming different bond angles and different internuclear distances resulting in different bond force constants. Therefore, each molecule has unique vibrational energies. The quantized

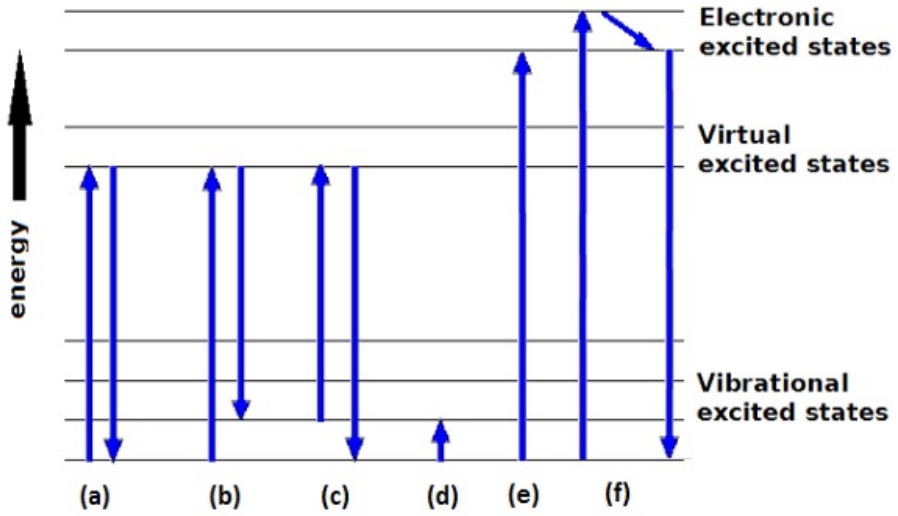


Figure 1: Energy levels of photon-matter interactions: a) Rayleigh scattering, b) Stokes Raman scattering, c) anti-Stokes Raman scattering, d) IR absorption, e) electronic absorption, and f) fluorescence.

energies of these vibrations can be considered fingerprints of a molecule.

For a charge to radiate an electromagnetic wave, the charge must be accelerated or decelerated. Electron clouds and molecular nuclei undergoing oscillatory motion are constantly changing velocity. When a photon is incident on a molecule, the electron cloud (a charge distribution) is distorted by the external oscillating electric field. The nuclei are also forced to move, but in the opposite direction of the electrons and with a much smaller amplitude as the mass of a nucleon is three orders of magnitude greater than that of an electron. The result of the movement of the electrons and nucleons is the formation of a dipole moment. Even though the net charge on the molecule is zero, the spatial distribution of positive and negative charges becomes such that there is a net molecular polarity.

The induced dipole moment oscillates at the photon frequency of the incident radiation. The nuclei, vibrating at a much lower frequency, may cause a change in the polarizability of the electron cloud. If so, this change to the polarizability results in an amplitude modulation of the dipole moment oscillation.

Polarizability is the ease with which a charge distribution can undergo spatial deformation by an external electric field. It determines the dynamic response of a system localized (bound) in a region of space due to a potential. This spatial distortion of the charge distribution forms instantaneous dipoles. Mathematically, the polarizability is the ratio of the induced dipole moment to the incident electric field perturbing the charged particles. Or, rearranged, the induced dipole moment vector P(x,y,z), is the the product of the polarizability

tensor,$\tilde{\alpha}$, and the incident electric field vector, E(x,y,z)::

$$P(x,y,z) = \tilde{\alpha}E(x,y,z) \tag{2}$$

The polarizability tensor is a 3x3 matrix where each coefficient entry depends on how strongly electrons are bound to the molecular nuclei.

$$\tilde{\alpha} = \begin{bmatrix} \alpha_{xx} & \alpha_{xy} & \alpha_{xz} \\ \alpha_{yx} & \alpha_{yy} & \alpha_{yz} \\ \alpha_{zx} & \alpha_{zy} & \alpha_{zz} \end{bmatrix} \tag{3}$$

The fact that the polarizability is a tensor means that it has different values along each normal axis for each component of the incident electric field, with respect to the coordinate system established for the molecule. The polarizability tensor is symmetric (i.e. $\alpha_{xy} = \alpha_{yx}$) and therefore can be diagonalized leading to only three components in a new coordinate system [32]. The result is equation 4.

$$\begin{bmatrix} P_{x'} \\ P_{y'} \\ P_{z'} \end{bmatrix} = \begin{bmatrix} \alpha_{xx'} & 0 & 0 \\ 0 & \alpha_{yy'} & 0 \\ 0 & 0 & \alpha_{zz'} \end{bmatrix} \begin{bmatrix} E_{x'} \\ E_{y'} \\ E_{z'} \end{bmatrix} \tag{4}$$

The polarizability tensor entries can be expanded as a Taylor series as follows where the $k$ subscript denotes the $k^{th}$ normal coordinate:

$$\alpha_{ij} = \alpha_{ij_{equilibrium}} + (\frac{d\alpha_{ij}}{dQ_k})_{equilibrium} \cdot Q_k \tag{5}$$

We ignore the higher order terms in the Taylor series because their magnitude is so small that they would therefore never be relevant with current Raman spectroscopy technology[3]. This assumption means that we are considering the molecular motion to be harmonic instead of the real situation of an anharmonic motion (non-regular periodicity in time). Most published Raman literature makes this assumption.

For a molecule oscillating at a vibrational frequency $f_k$ its vibrational coordinate Q is

$$Q_k = Q_{k_{max}}(\cos 2\pi f_k t) \tag{6}$$

Since we stated above that $\overrightarrow{P} = \tilde{\alpha}\overrightarrow{E}$, where the electric field will change sinusoidally with the frequency of the incident photon ($f_o$) as the following

$$E = E_{max}(\cos 2\pi f_o t), \tag{7}$$

the induced dipole components can be written as

$$P = \alpha_{equilibrium} \cdot E_{max}(\cos 2\pi f_o t)$$

$$+(\frac{d\alpha}{dQ_k})_{equilibrium} \cdot Q_k(\cos 2\pi f_k t) \cdot E_{max}(\cos 2\pi f_o t) \tag{8}$$

Using the following trigonometric identity

$$2(\cos 2\pi f_o t)(\cos 2\pi f_k t) = \cos[2\pi(f_o - f_k)t] + \cos[2\pi(f_o + f_k)t] \tag{9}$$

leads to equation 10 for the induced dipole moment which has two separate components that are the cosine of terms related to the sum and difference of $f_o$and $f_k$:

$$P = \alpha_{equilibrium} \cdot E_{max}(\cos 2\pi f_o t)$$

$$+(\frac{d\alpha_{ij}}{dQ_k})_{equilibrium} \cdot \frac{Q_k \cdot E_{max}}{2} \cos[2\pi(f_o - f_k)t]$$

$$+(\frac{d\alpha_{ij}}{dQ_k})_{equilibrium} \cdot \frac{Q_k \cdot E_{max}}{2} \cos[2\pi(f_o + f_k)t] \tag{10}$$

The first term, a dipole contribution at the same frequency as the incident photon, describes the elastic Rayleigh scattering. It is the second term and third terms that define the inelastic Stokes and anti-Stokes Raman scattering, respectively. The second and third terms include multiplication by a change in the polarizability tensor with respect to vibrational amplitude at the equilibrium position. Therefore, for either type of Raman scattering event to occur, this derivative must have a value not equal to zero. This derivative is commonly referred to as the Raman cross section.

$$(\frac{d\alpha}{dQ})_{equilibrium} \neq 0 \tag{11}$$

Equation 10 is more easily represented as the sum of a dipole resulting from equilibrium polarizability and two dipoles resulting from dynamic changes in the polarizabilty during vibration.

$$P = P(f_o) + P(f_o - f_k) + P(f_o + f_k) \tag{12}$$

We note here that this classical description does not provide any reason why Stokes and anti-Stokes intensities would differ. It is only from the quantum mechanically derived Boltzmann relation mentioned earlier that the two phenomena have differing intensities. Quantum mechanical rules relate the polarizability tensor to the amount of scattering through the wavefunctions. Though it is possible to estimate Raman intensities of small molecules using quantum mechanics and supercomputers, the number of fermions which make up a fatty acid or the unit cell crystal of a hydrated mineral make this task difficult. Without going beyond the scope of this study, the result is that the overall intensity of Raman scattering is proportional to the fourth power of the difference between excitation frequency and the molecular vibrational frequency. In equation 13 showing the relationship for Raman intensity, the K coefficient is a collection of physical parameters relating to both the sample and Raman instrument

parameters. Since the excitation frequency is much greater than the molecular vibrational frequency, published literature often states that the intensity relationship is simply a fourth power of only the excitation frequency.

$$I = K(f_o - f_k)^4 (\frac{d\alpha}{dQ})^2 E_{max}^2 \tag{13}$$

The relative intensities of the multiple Raman peaks of a molecule is a function of the polarization of the incident light with respect to the coordinates of a single molecule or crystal. Since the beam size (field of view) used in this study was far greater than the size of one molecule or crystal, we assume there was not a preferred orientation in our samples. This is definitely the case for the UV system, but maybe not exactly true for the green Raman microscope as it has a much smaller spot size. Though still larger than a single crystal, the green laser spot size may be small enough that crystals exhibit a preferred orientation, thus potentially affecting relative intensities. As in most published Raman studies, polarization has been ignored in this work.

An electron cloud is more easily distorted if the electrons are shared between the constituent atomic nuclei. That is, the magnitude of the polarizability tensor elements will be greater for molecules with covalent bonds, or for functional groups which are less polar. Here, we refer to a functional group as a portion of the molecule that is a class of bound atoms (i.e. alcohol, carbonyl). Many of these functional groups have vibrational motions in which there is only displacement in those atoms while the rest of the molecule remains unaffected. These functional groups are mechanically independent from the remainder of the molecule and will exhibit similar frequencies when they are a constituent of other molecules.

Since carbon forms mostly covalent bonds, many organic molecules produce high intensity Raman scattering. This will be evident from our stearic acid spectra presented in chapter 5. The functional groups mentioned above are common in organic chemistry, but are often polar covalent. Therefore, in many organics, the aliphatic backbone or aromatic ring produces intense bands, while the defining fingerprinting functional groups of the molecule produce only weak bands. In chapter 5, the carboxyl group (C(O)OH) present in stearic acid will be addressed in detail.

Polar molecules and molecules formed with ionic bonds have a low change in polarizability with respect to a change in normal coordinate positions (vibrational amplitude). Therefore, vibrations involving those bonds have a low probability of scattering inelastically. Molecular vibrations which cause a molecule to become polar, such as the asymmetric stretch of the linear molecule carbon dioxide, will cause no Raman scattering at all [4].

Raman scattering is sensitive to hydrogen bonding [4]. The hydrogen bond is an association of an 'X'-H group of a molecule or crystal with the 'Y' atom of another molecule or crystal. The 'X' atom has a high electronegativity and therefore the 'X'-H bond is ionic or polar covalent. In the context of both the minerals and the organic used in this study, the 'X' atom is always oxygen, though it may be nitrogen for other important molecular biosignatures such as

alanine (2-aminopropanoic acid). The H-'Y' bond is mostly an electrostatic attraction, but may also have weak covalency. Larkin [4] reports that this bonding results in a redshift of the 'X'-H stretching peak, an accompanying broadening of the band, and sometimes an intensification of the band. Conversely, he reports that 'X'-H bending bands show a blue shift when affected by hydrogen bonding.

Condensed phase O-H stretches experiencing hydrogen bonding will usually occur between 3200 and 3600 $cm^{-1}$. However, if the O-H is structural in a crystal, the stretches will often occur between 3400 and 3700 $cm^{-1}$. Adsorbed water and structural water bands overlap in our synthetic gypsum, a hygroscopic mineral. This double water in conjunction with hydrogen bonding leads to broader O-H stretching peaks than in the other hydrated sulphate examined.

Band location is both a factor of bond force constants and masses of the constituent atoms. Due to this, minor changes to these quantities throughout a sample can cause band broadening. Force constants may change with the surrounding chemical environment, while different isotopes can cause new, slightly shifted peaks for the same functional group vibration. For example, ~1% of carbon is carbon 13 which is 8.3% more massive than carbon 12. Stearic acid contains 18 carbons, so there is about a one in five chance that a stearic acid molecule will contain a heavier atom which could slightly shift bands. This can become more important when the abundances of isotopes of an atom are more evenly divided in nature, such as is the case with most transition metals.

In Raman spectroscopy a sample is excited with a laser. Collection optics filter out the elastically scattered light and direct the inelastically scattered light towards a wavelength separating device; a reflective diffraction grating in the case of this study. The wavelength separated light is then detected by a CCD and recorded by a computer. The systems used in this study will be described in more detail in both chapter 4 and in the appendices.

Presentation of Raman spectra places intensity on the y-axis and wavenumber on the x-axis. The intensity is usually presented in arbitrary units as it is often a counting of photons. Absolute measurement of intensity is difficult because there are too many ill defined variables, such as the number density of scatterers and multiple instrument parameters. Since reported intensity is arbitrary, normalization of spectra is common in published literature.

Due to symmetry properties, some molecular vibrations of smaller molecules are either Raman or IR active, but not both. Due to this, it is often suggested that these two spectroscopic techniques be used in conjunction for definitive identification of a sample[4]. This study used Raman spectroscopy exclusively since both our target organic molecule and target minerals are sufficiently structurally complex that definitive identification should be possible from Raman only using at least at one of the selected excitation wavelengths.

# 3 Life and organic carbon

## 3.1 Astrobiology

Astrobiology concerns the study of the origin and evolution of life in the universe, the search for habitable environments, adaptation to extreme environments, and prebiotic chemistry. The main questions being asked in this field are *"does life exist, or has life existed beyond Earth?"* and, if so, *"how can we detect it"?* Evidence of habitability and the detection of life building chemicals (organic molecules) are NASA's primary objectives for planetary exploration in our solar system.

The Moon of the Earth, the planets Venus and Mars, the comet 67P Churyumov–Gerasimenko, the asteroids Itokawa and Eros, and the Saturnian moon Titan are the only planetary bodies which humanity has landed a robot on. Of these, only Mars and Titan are expected to have any reasonable possibility of harbouring life. Only Mars currently has any landed probes searching for evidence of life. The Jovian moon Europa and the Saturnian moon Enceladus may also be candidates for harbouring life, but neither have planned missions for robotic landings in the next decade.

The current rovers working on Mars, Curiosity and Opportunity, have various instruments to measure elemental abundances, mineral crystallography, molecular structure, and molecular abundances. They specifically search in areas related to ancient lacustrine environments. This is because as stated in chapter 1, we know that all life on Earth requires liquid water. Therefore, past life is more likely to be found where there is evidence of past water.

In NASA's quest to find evidence of life on Mars, some basic assumptions concerning life are made. They assume that Martian lifeforms would be based on the same elements as terrestrial life. They also assume that Martian life requires liquid water. If life did indeed exists there, they assume that it would require a self-contained structure similar to those of cells and microbes on Earth. Next, the same thermodynamic, chemical, and physical limits to cell sizes and shapes should apply. Finally, it is believed that similar to their terrestrial counterparts, Martian lifeforms would require complex organic molecules to be present to form structural compounds and to preserve genetic information [1].

## 3.2 Biosignatures

Biosignatures are detectable features which are diagnostics for biological processes. They can be physical features such as fossilized cells. They can be metabolic imprints left upon the environment, such as enrichment or depletion of certain elements (isotope ratios, spatial patterns), or the existence of non-equilibrium biogenic gases (i.e. methane). They may also be molecular biosignatures which are essential to the structure, function, or genetic information of a life form (i.e. fatty acids, amino acids, nucleic acids). This study will only consider a molecular biosignature as that category would be most easily identifiable with Raman spectroscopy. It is assumed that any extinct or extant

life on Mars would be microbial, and therefore the probability of finding physical features such as fossils using a camera is low[15].

Organic compounds are chemicals where one or more carbon atoms form covalent bonds with other elements. Most commonly these other elements are hydrogen, nitrogen, sulphur, phosphorus, or oxygen (CHNOPS). Since Raman intensity is proportional to the covalency of chemical bonds, Raman spectroscopy is highly sensitive to organic compounds. Though covalent carbides, cyanides, carbon sulphides, carbonates, and oxides of carbon may fit this description, usually, they are considered to be inorganic. Some argue that an organic compound must have at least one C-H bond. This additional requirement removes carbon allotropes like diamond, graphite, and graphene from the organic categorization.

Though some organic compounds can be produced through man made synthesis (i.e. plastic polymers), it is the naturally occurring organic compounds that one is concerned with for potential biosignatures. These compounds produced by plants or animals include many sugars, nutrients (vitamin b12), carbohydrates, enzymes, hormones, lipids, oils, fatty acids, nucleic acids, amino acids and proteins. It is larger molecules and stereoisometrically complicated molecules that are usually more indicative of biotic synthesis. That is, if a molecule is chiral, abiotic formation will not produce a preferred stereoisomer, but biotic formation will.

Since Mars has no ozone layer, extreme UV photochemical breakdown and cosmic rays would destroy almost all exposed biosignatures. This is because the high energy of the photons or particles can break apart functional groups. It is therefore assumed that any biosignatures present on the Martian surface or in the upper subsurface would be in small concentrations [33].

Raman spectroscopy has proven itself as an important method for characterizing biosignatures, specifically those produced by microbes in extreme environments. Biosignatures that are important to survival strategies such as beta-carotene (UV protection) or glycerol (low temperature protection) have been used in previous studies. Vitek et al [34] used both NIR and green excitation to examine beta-carotene in a gypsum matrix. They found that the C-C stretch was visible at all of the concentrations that they studied. This was down to parts per million, but we note that beta-carotene has a resonance feature at the 532 nm excitation which they used. That study concluded that if Martian lifeforms synthesized beta-carotene, habitable evaporitic rocks could have preserved these biosignatures in the subsurface at concentrations that would be detectable. However, their study only examined a Raman window up to 1600 $cm^{-1}$. The most indicative peaks for aliphatic chain organics are for C-H stretches that occur around 2900 $cm^{-1}$, or N-H stretches that appear at slightly higher wavenumber. This same study suggested that a minimum of two Raman bands is required for unambiguous identification of a compound, whether organic or inorganic.

## 3.3 Habitability

Habitability can be loosely defined as an environment's potential to support any form of life. This is usually in the context of temperature, pressure, radiation, suitable energy sources, pH, salinity, and the presence of liquid water. The presence of the CHNOPS elements and essential nutrients are also considered in habitability assessments. As humanity intends to stretch itself out into the solar system in future manned missions, the search for habitable environments for humans remains an important quest. Although habitability for human explorers is often considered a binary yes or no question, for the more general term 'life', habitability is sometimes seen as a spectrum (very habitable, slightly habitable, not habitable).

Porous evaporitic rocks on Mars may provide a suitable habitat for microbes, extinct or extant [34]. Molecular remnants could be sustained in these locations as evidence for past life. Mini-TES and APXS experiments from the Opportunity rover suggest that evaporites such as hydrated calcium and iron sulphates are abundant [35, 29].

Brines could also serve as potential habitats as halophilic extremophiles have been found in various locations on Earth. Locations near brines would be another location to look for biogenic molecular remnants. Perchlorates which can form brines have been found on the Martian surface [36].

## 3.4 Preservation of molecular biosignatures

Cumulative exposure to the shock from impact events, diurnal temperature fluctuations, oxidation, as well as exposure to ionizing radiation and cosmic rays can limit the ability of an environment to preserve a molecular biosignature. Geomorphological features such as caves or the subsurface of a planet could act as stable environments to shield molecules from some of the above listed issues. Caves and lava tubes have been observed on Mars [37] [38] and therefore would be an ideal place to search for organics. On Earth, extremophiles have been found living in the Earth's crust at great depths, kilometers deep in igneous rock[39]. Unfortunately, it is unlikely than any upcoming robotic missions to Mars will have the capability to search in such environments.

Organic compounds can be sequestered and preserved if incorporated into a mineral structure. Porous evaporitic minerals and layered silicates are good candidates for this to occur. Richardson [40] mentions that sodium sulphates found in layers as a weathering product of basaltic rock would be a good place to look on Mars. He suggests these minerals are key components in geochemical reactions on Earth and have been known to contain organics in both volcanic and evaporitic settings. For sulphates, the organics would be preserved in the mineral lattice. This could be as either intracrystalline inclusions or substitutions. Whereas one finds intercrystalline organics at grain boundaries between crystals, intracrystalline inclusions are distributed within an individual crystal. How exactly larger molecules can be incorporated into the dense structure of an inorganic mineral remains an unanswered question that scientists such as Weber

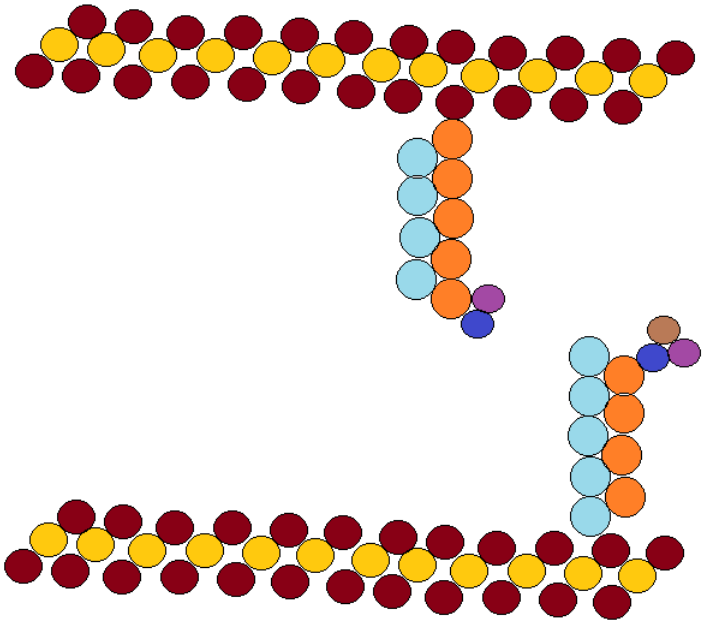

Figure 2: Organic molecules attached to interlayer surfaces of a clay.

and Pokroy[41] have been examining.

For clays, the partially charged, extensive surfaces can adsorb organics for preservation. In some cases where an organic molecule contains a polar functional group, the molecule and phyllosilicates can even chemically bond at an active site on the clay where there is a net charge. By holding smaller organics in place, the clay surfaces can act as catalysts in the creation of large organic molecules from smaller ones (see Figure 2).

Richardson [40] suggests that while nucleic acids, proteins, and carbohydrates are too big to be associated with mineral matrix integration, smaller molecules such as amino acids and fatty acids may be adequately sized for this.

It has been suggested that if the formation of clays and organics is synchronous, a biosignature deposit may be more resistant to weathering. The explanation is that there would already exist a chemical equilibrium between the organics and clays [15][42]. Rapid burial of molecular biosignatures within a clay aids in preservation because quicker reduction of porosity and permeability leads to more anaerobic conditions[15][26].

Loterava and Prozorov [43] found that adsorption of DNA onto the clays montmorillonite and kaolinite protected it from degradation by deoxyribonuclease, which is an enzyme that catalyzes breakdown of linkages in the backbone of the DNA molecules.

## 3.5 What we currently know about organics on Mars

The majority of our knowledge regarding Martian organic compounds is due to examinations of Martian meteorites. Both simple and complex aliphatic and aromatic molecules have been discovered in the Shergottite-Nakhlite-Chassignite meteorites, such as various types of amino acids [11]. It is the composition of gas inclusions in these meteorites that links their origin to Mars. Mars has a unique atmospheric composition and gases such as $N_2$ and $CO_2$ can serve as geochemical fingerprints. The noble gases can also aid in this determination. However, it is not yet certain that the organics found on Martian meteorites are of Martian origin.

Methane plumes have been identified on Mars using ground based observations [44]. The Curiosity Rover has also identified methane using the Sample Analysis at Mars (SAM) instrument[45]. Methane can be produced both biologically as a waste product from microbes and geologically when volcanic rock interacts with water and other gases. It may also form from UV irradiation of carbonaceous chondrites [46]. The source of the Martian methane has not been determined.

More recently, Curiosity has detected organics in a drilled sample of mudstone. A large constituent of the mudstone are smectite clays which are examined in this study. The molecules detected included the following [47]:

-chloromethane
-dichloromethane
-trichloromethane
-carbon tetrachloride
-dichloroethane
-dichloropropane
-dichlorobutane
-chlorobenzene

It has been suggested that a different group of organics may have been present in the mudstone and that the detected organics formed within the SAM instrument when the samples were heated prior to analysis. This would be possible since perchlorates have been located on the surface of Mars [36]. Perchlorates contain both chlorine and oxygen and could react with both aliphatics and aromatics to produce the discovered molecules.

## 3.6 Properties of organic carbon bonding

Carbon is made up of six electrons, six protons, and usually, 6 neutrons. Two other isotopes exist which have either 7 or 8 neutrons. In a gaseous state, an isolated carbon has the electronic structure $1s^2 2s^2 2p^2$, where s and p refer to the azimuthal quantum number. Carbon has 4 valence electrons and can have three different hybrid bonding orbital configurations; tetrahedral ($sp^3$), trigonal ($sp^2$), and linear (sp).

In the tetrahedral configuration, carbon is bonding to four atoms, and the four valence electrons form hybrid orbitals which are approximately 25% s in

character and 75% p in character. When there exists a double bond, such as in a carboxylic acid where a carbon of the aliphatic chain is double bonded to an oxygen, while also singly bonded to a carbon and singly bonded to the oxygen end of a hydroxyl, the central carbon is in trigonal configuration. In this scenario the bonds are approximately 33% s in character and 67% p in character. Finally, a carbon with a triple bond, such as an alkyne, is in a linear configuration and would have orbitals that are 50% s and 50% p in character. Since there are no triple bonds in a fatty acid, only the $sp^2$ and $sp^3$ hybridizations are relevant to this study.

# 4 Methodology I: Experimental techniques, sample suite, equipment, and data analysis used

*Given what we know about Mars, can we detect signs of life on that planet using Raman spectroscopy?* That is the general question this study examines. Raman spectroscopy is a molecule identifying technique and therefore a molecular biosignature would be our target identifier of past or present life. By mixing a biosignature within aqueous alteration minerals that are analogous to what is on the surface of Mars, situations where one might find a Martian biosignature were simulated. Inelastically scattered light was collected from the mixture and it was determined if one could detect and identify the organic (at various concentrations) within the composite mineral plus organic Raman spectra.

Most previous Raman spectroscopy studies regarding Martian minerals were qualitative and performed using visible or NIR excitation. The locations of Raman bands and their relative intensities comprise the majority of the published data. Some quantitative work has been done on mixtures of potential biosignatures and minerals, but much of that work was for simple mineral matrices that were not necessarily significant to astrobiology, such as quartz [2]. It was clear that studies involving biosignature detection in mixtures of more complex minerals would be required to accurately simulate the situation on Mars.

Work has been done on biosignature detection in Mars relevant minerals such as gypsum [34] and sodium sulphate [40], but the former was done with a different excitation wavelength and the latter was done using a completely different technique than Raman spectroscopy, laser desorption mass spectroscopy.

For our research design, individual Raman spectra were to be taken for both the organic compound and the minerals using the prototype in-situ ultraviolet Raman system developed at York University[2]. Mixtures of samples would then be made and the Raman spectra of mixtures would be taken. Using this system, data was easily obtained for both the organic fatty acid and the hydrated calcium sulphate, gypsum. However, as will be presented in chapter 6, none of the phyllosilicates, nor the hydrated iron sulphate, would lead to data with clear Raman peaks. A literature review of this problem suggested that the small particle size of clays was the reason for the difficulty obtaining Raman data, but few details about the physical mechanism for this effect were available [48, 49].

A decision was made to test out the same samples on a commercial Raman microscope with green excitation. The result was that although fluorescence was very strong for some of the clays with this system (likely due to prior organic contaminants), Raman peaks were at least obtainable. Raman spectral matching from the RRUFF™ database was used to confirm that the observed peaks did represent the minerals in question. This database is a project by the University of Arizona's department of geosciences to create a library of Raman spectral data for minerals which have been well characterized by X-ray diffraction and electron microprobe analysis. The database is used by mineralogists and geochemists as a standard to compare against their observed data.

The nontronite samples were not pure enough to consistently detect nontronite with each acquisition. Since the commercial Raman microscope has such a small spot size, a bit of "cherry picking" was required to find the actual nontronite mineral desired in the sample. It was due to this issue and the fact that our lab had a very limited amount of nontronite that it was decided that nontronite would not be included in our study of mineral-organic mixtures. Individual nontronite spectra would still be included in this study because that mineral has relevance to both astrobiology and the exploration of Mars. Between the hydrated sulphates, the kaolinites, and the montmorillonites, there would still be enough astrobiologically relevant minerals to make mixtures from.

Though the commercial Raman microscope with green excitation was initially used just as an attempt to solve the problem with our ultraviolet Raman data, it was then decided to include the green Raman data since there are two Raman systems with green excitation planned for Mars in 2020. A comparison of the results from our two systems for the two hydrated sulphates used in this study was presented as a poster at the 47th Lunar and Planetary Science Conference[50].

## 4.1 Samples used

### 4.1.1 Organic biosignature

The organic molecule used in this study is the fatty acid stearic acid. It was obtained from Sigma Aldrich and is product number S4751. Details on this fatty acid will be presented in the following chapter.

### 4.1.2 Hydrated sulphates

Gypsum and a jarosite group mineral were selected and obtained from the Planetary Spectrophotometry Facility at the University of Winnipeg. This work used sulphates with grain sizes $< 45$ microns. This higher limit is only due to sieve hole size. Jarosites found in nature often have grain sizes $< 5$ microns. We assume sizes on a similar order for our gypsum.

To ensure no trace metal impurities were in the gypsum sample used, a batch of powdered synthetic gypsum was selected for examination. The effect of transition metals as structural components or as impurities on the UV Raman spectrum will be discussed in chapter 7. The synthetic sample is highly hygroscopic, thus O-H stretching intensities could not be expected to be consistent from one trial to the next. This factor does not affect the overall goals of this study as the O-H regions in the mineral do not overlap with the Raman bands of the organic.

Initially we did not know which type of cation the jarosite group sample contained as it had not been identified by the providing research facility. We compared our results for the Raman shift of the sulphate symmetric and asymmetric stretches to those in a study that examined these shifts along a spectrum between K- to Na- jarosite end members[51]. From this we were able to defini-

tively determine that our sample is natrojarosite. Data from Frost et al [52] were also in agreement that our sample was natrojarosite.

### 4.1.3 Phyllosilicates

All of the clays used in this study were obtained from the Clay Minerals Society. It was the Clay Minerals Society [53] that provided details on the percent compositions of the standard clay samples. The available data on these samples was quite detailed and therefore their associated chemical information has been placed in the appendices. A brief description of the selected samples follows here.

Two kaolinites were selected from Georgia, USA. Their main difference is their degree of disorder. This was confirmed by x-ray diffraction at the Royal Ontario Museum. They also have slightly different amounts of structural titanium substitutions.

Four montmorillonites were selected from multiple locations in the USA. The Texas montmorillonite has an interlayer dominated by mostly calcium cations. The Arizona montmorillonite has an interlayer dominated by calcium and magnesium. The Wyoming sample has an interlayer dominated by sodium and some calcium. Finally, the California sample contained all three interlayer cation types.

Three nontronites were selected; two from Australia and one from Germany.

Pictures of the mineral samples used in this study are shown in Figure 3.

All of the phyllosilicates had iron content. While nontronite definitely has structural iron and montmorillonite sometimes does, it is assumed that almost all of the iron in the kaolinte samples was from impurities. A comparison of iron content (reported as hematite) in the samples is provided in Figure 4. The Clay Minerals Society [53] obtained this data by X-ray fluorescence measurements.

## 4.2 Pre-treatment of mineral samples

All of the minerals used in this study except the gypsum were baked for 4 hours at 150°C to attempt to remove adsorbed water from their surfaces while not affecting their crystal structure. Harrison [54] reported that powdered samples of gypsum started to dehydrate at 100°C. Therefore, we were unable to affect the adsorbed water on the gypsum without potentially causing an unwanted affect on the mineral.

Unfortunately, organic contamination was not removed using this method. The result is a small, ill defined peak at ~2900 $cm^{-1}$ for many of the clays. This is prior to the introduction of of our fatty acid. Carrier et al did not mention this in their paper[55], however they informed the author privately about using a leaching process to remove organic contaminants prior to making their mineral/organics mixtures. For organic contamination removal in Evan Eshelman's PhD dissertation[5], he heated his substrates to 600°C, but it is not clear that this process would be sufficient to remove all contaminants in a

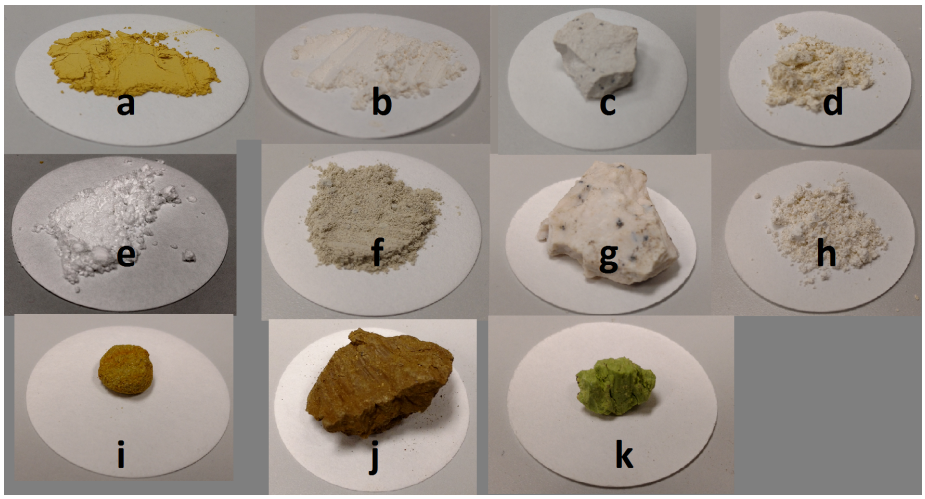


Figure 3: Collection of mineral samples used in this study. The white circular paper is 42.5 mm in diameter. a) natrojarosite b) STx1b montmorillonite c) SAz2 montmorillonite d) KGa2 kaolinite e) synthetic gypsum f) Swy2 montmorillonite g) SCa3 montmorillonite h) KGa1b kaolinite i) NG1 nontronite j) NAu2 nontronite k) NAu1 nontronite

terrestrial clay. Also, the substrates used in his study are less likely to contain organic contamination when compared to terrestrial clays or sulphates.

## 4.3 Raman equipment

### 4.3.1 Green excitation (532nm) commercial Raman microscope

The instrument used for the green excitation was a Horiba LabRAM ARAMIS shown in Figure 5. This was provided by the Royal Ontario Museum (Toronto, Canada).

The exact system is no longer manufactured, so it is difficult to find specifications for the system such as resolution, but similar systems that are the successors to the ARAMIS can be found at the website (*http://www.horiba.com*). In our data, adjacent peaks located ~ 15 $cm^{-1}$ apart are easily resolvable and we estimate the actual resolution to be $< 10$ $cm^{-1}$. The wavelength precision of a data point, found by dividing the Raman window observed in a given acquisition by the number of pixels on the CCD is $< 1$ $cm^{-1}$. Sometimes this is reported in the literature as spectral dispersion.

Wavenumber calibration was done using the single stretching peak of silicon. A 30 second photobleach was first performed on the minerals followed by a ~ 15 minute accumulation of a Raman signal. During this long accumulation, a number of similar scans are added together. This process increases the signal to noise ratio. However, no background correction was made for noise for this

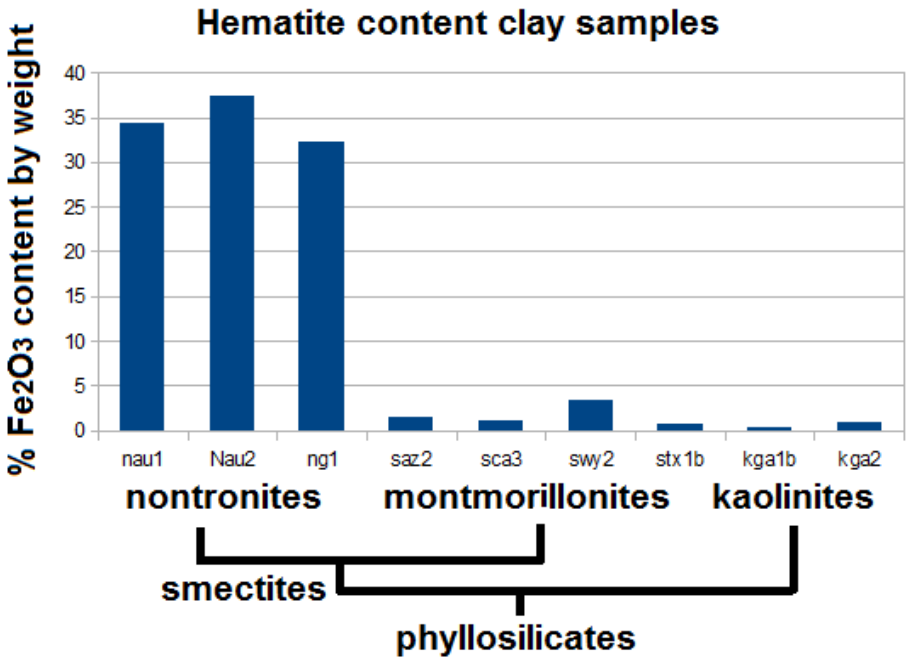


Figure 4: Hematite content in clay samples. Note that oxygen-bonded structural iron and iron bearing impurities are grouped together as hematite. The x-axis lists the different clay samples.


Figure 5: Horiba LabRam ARAMIS commercial Raman microscope at the Royal Ontario Museum

system except for that from cosmic rays.

#### 4.3.2 Ultraviolet excitation (266nm) prototype in-situ Raman system

Our experimental set up for UV excitation was the same as that used in Eshelman et al [2] (Figure 6), except for two minor changes. First, the diffraction grating was changed from 2400 lines/mm to 3600 lines/mm for additional resolution (Figure 7). Second, a dichroic beamsplitter was added so that a 180 degree collection geometry could be used for collection of scattered light (Figure 8 ). Wavenumber calibration was done using multiple peaks of the amino acid L-alanine. The values for these peaks had been well characterized by the Institut National d'Optique (Quebec City, Canada) and allowed for a fit using the Andor Solis © software. A ~22 minute accumulation of Raman signal was then performed for each Raman window. Background noise caused by detector dark current, hot pixels, and ambient light was removed by taking a full accumulation with the laser beam blocked and subtracting this background from the regular signal. The counts are digitized data form the detector's analog to digital converter. A chiller was used to pump water through the camera to decrease noise. The CCD manufacturer states that for each $7^oC$ that the temperature is decreased, the dark signal produced by the flow of dark current is cut in half.

When using L-alanine to perform our daily x-calibrations, we also took note of the photon count readings of the main C-H stretching peak at 2977 $cm^{-1}$ to gain confidence on relative intensities for our y-axis measurements. At a gain setting of 3000 in video mode (Andor Solis © software), a setting where the system repeatedly performs a single scan which is continuously updated on the display, we aimed for a repeatable measurement of 25000 photon counts per acquisition (+/- 1000) before continuing on with obtaining data from our samples. The associated uncertainty could lead to errors of 4 %. However, we

note that the laser power was not stable to better than approximately +/- 2 %.

For overall y-axis calibration (flat fielding), a deuterium lamp (NIST calibrated) was used as a broadband UV source to observe our CCD response. The low energy region of the Raman window (below 1000 $cm^{-1}$) has multiple overlapping responses because of both the edge filter and the bleed of the laser excitation. These complicate any correction as this low energy region is highly non-linear. The remainder of the Raman window data backs up that most of the spectrum is flat, thereby not requiring correction. Since we are not drawing conclusions on relative peak heights within an individual spectrum, the y-calibration is not as important. Also, all of the peaks used to identify organics within the minerals are at greater wavenumber than the non-linear region. The result of choosing to omit the flat field has almost no effect on the conclusions of this thesis.

Andor, the manufacturer of the spectrometer, offers a resolution calculator (*http://www.andor.com/ResolutionCalculator.aspx*) which takes into account detector type, spectrometer type, grating lines/mm, and detection window centre wavelength. Using this information, we determined a value for our instrumental setup of ~ 12 $cm^{-1}$. Since this calculation does not take into account the width of our laser line, the edge filter used to block off Rayleigh scattering, or any other system parameters, it has been suggested [2] that the resolution of this system (using the 2400 lines/mm grating) is closer to 30 $cm^{-1}$. This spectrometer was designed to be compact which is why it has a short focal length of 163 mm. A longer focal length would provide greater resolution. The RLS system for ExoMars will have a shorter focal length, but significantly more laser power at the sample. The precision of a data point, found by dividing the Raman window observed in a given acquisition by the number of pixels on the CCD is ~ 2 $cm^{-1}$.

Expanded details on this system are provided in the appendices. These include laser power, pulse repetition frequency and pulse width.

## 4.4 Raman windows

Due to the laser having a spectral width and the edge filter having a response curve, we do not start taking data right from 0 $cm^{-1}$ Raman shift. For the commercial Raman microscope system we observed from ~150 $cm^{-1}$ to ~3500 $cm^{-1}$. Since the dominant peak for fingerprinting kaolinite is ~ 140 $cm^{-1}$ the observation window was extended slightly for that system when using those samples. With the prototype in-situ system we observed from ~300 $cm^{-1}$ to ~3800 $cm^{-1}$. No relevant bands for fingerprinting these minerals or organics are above this energy. Only low intensity overtones may be found above 3800 $cm^{-1}$. With the UV system we are incapable of properly viewing the region of the dominant kaolinte peak mentioned above.

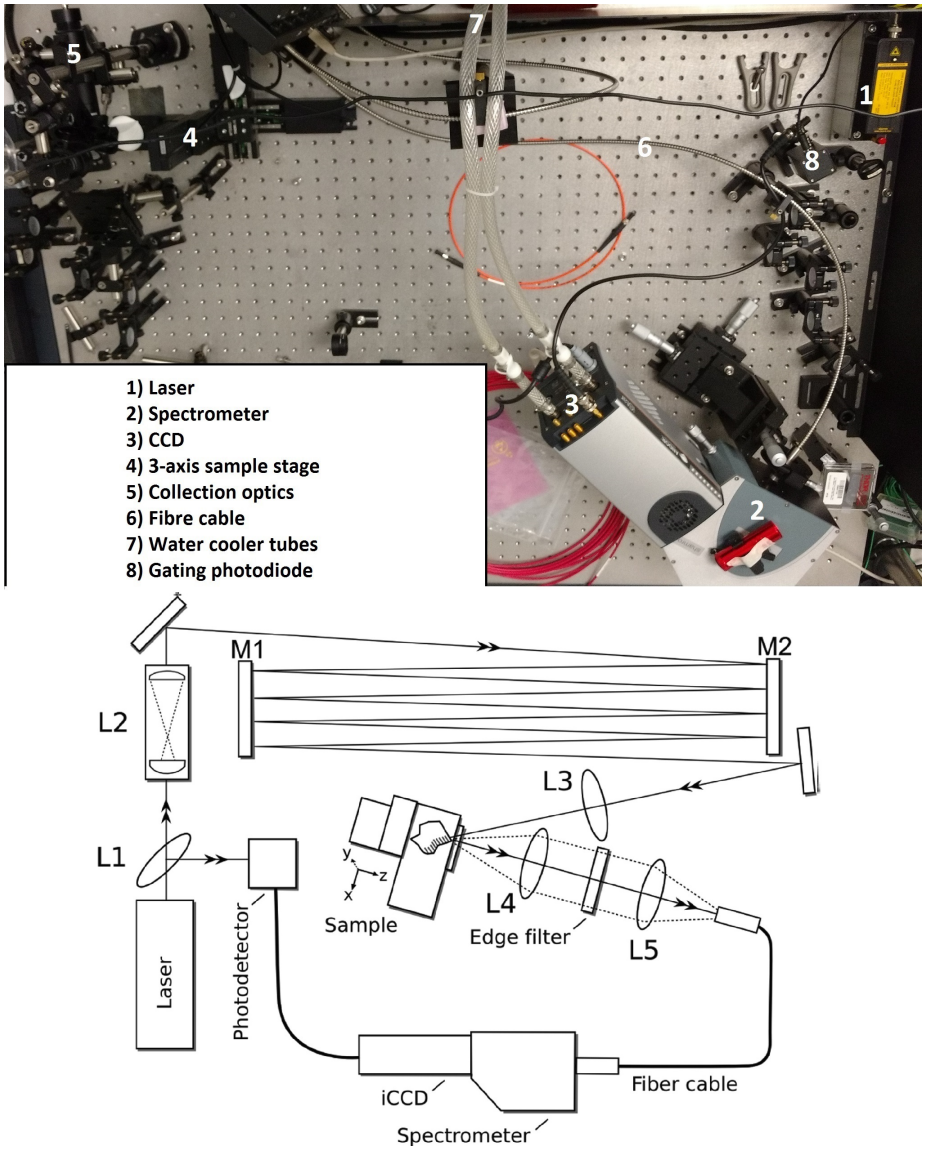


Figure 6: Prototype in-situ stand-off Raman system at the Planetary Exploration Instrumentation Laboratory (York University). Top: colour image labels components. Bottom: Schematic of system used with permission from Eshelman et al [2]. L1 is a quartz beam sampler used to trigger a photodetector which opens the gate on the camera. L2 is a beam expander. M1, M2 (mirrors) and L3 (lens) are used to direct light towards the sample. L4 and L5 (lenses) are the collection optics which direct light towards the detector.

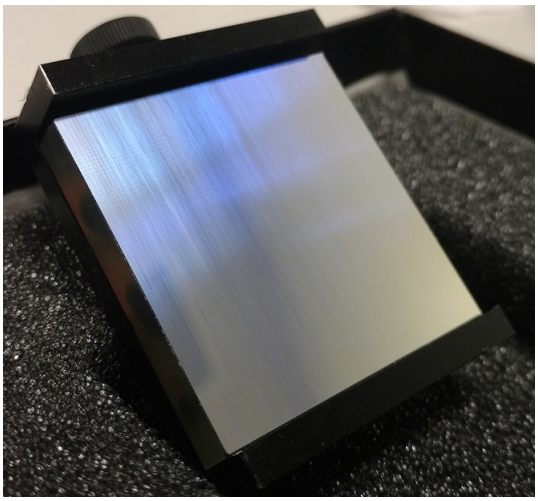

Figure 7: 3600 lines/mm diffraction grating for UV spectroscopy.

### 4.5 Data analysis methods

After data was obtained using the spectrometers, comma separated value files were exported to be read into MATLAB ©.

The commercial Raman microscope system automatically stitches together overlapping accumulation windows. In some cases fluorescence levels changed between window accumulations, the result being sharp changes in what would usually be a smooth background curve. Where possible, attempts were made to fix this in post processing. Since changes along the fluorescence spectra were sometimes more significant than the Raman peaks, 'false peak' artifacts appear in the background corrected green spectra. This paper will attempt to point out which peaks are not 'true' when the relevant spectral data is presented.

For the prototype UV in-situ system the stitching between accumulation windows was done in MATLAB ©.

Where background fluorescence was removed from spectra, this was done using the RRUFF database software Crystal Sleuth ©. Details on the algorithm which that program uses are not available. Usually, this process is done by selecting a certain number of points which are assumed to be on the baseline. Then, the software would connect these lines, creating an artificial baseline. The artificial baseline is then subtracted from the original spectral data. Alternatively, polynomial curves which best fit the profile are subtracted. Unless one creates an infinite number of points in the first method, or uses an infinite order polynomial in the second method, the process will lose some valuable data and retain unwanted data. That is, the $R^2$(R squared) value of the subtracted baseline compared to the real baseline can never approach unity. Any level of noise severely complicates this process and distorts the resulting spectra.

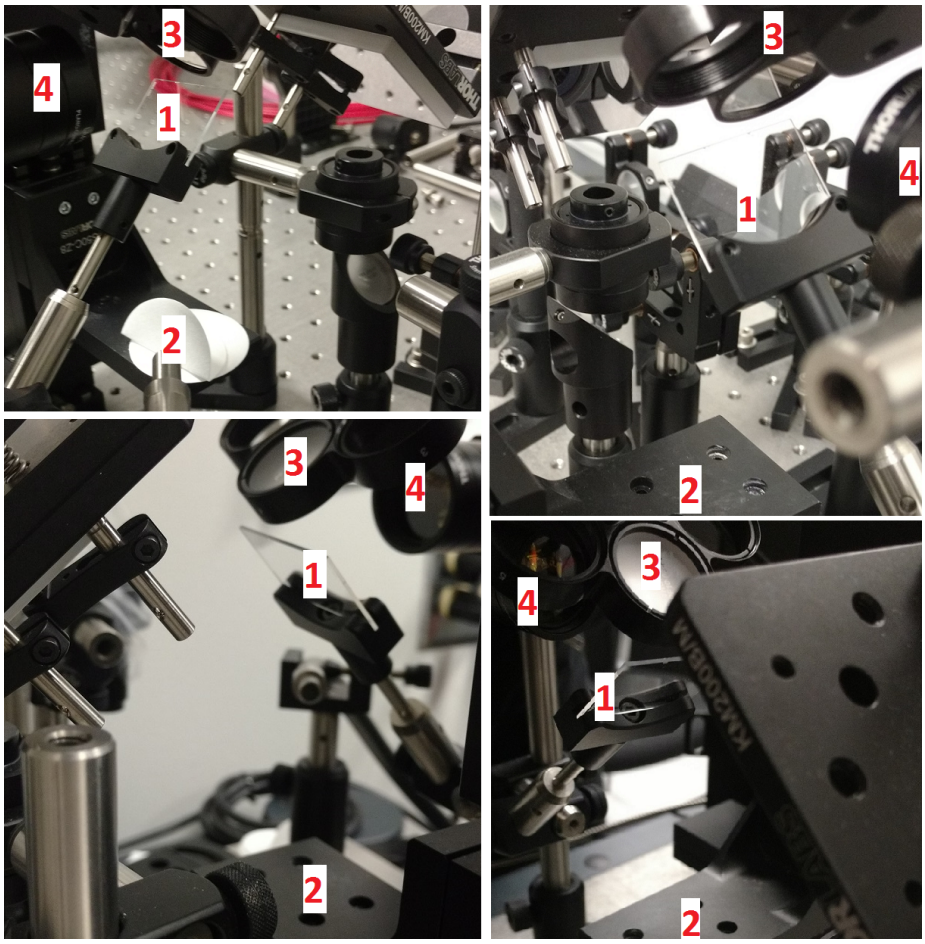


Figure 8: Sample area of prototype in-situ system from various viewing angles. 1) dichroic beamsplitter 2) sample stage 3) harmonic mirror 4) collection optics including edge filter

# 5 The biosignature stearic acid

**IUPAC name: Octadecanoic acid - $C_{17}H_{35}CO_2H$**

Molecular biosignatures are organic molecules which have both structure and chemistry required for biological processes. This study used the fatty acid stearic acid as the target biosignature.

Fatty acids are carboxylic acids which have an aliphatic backbone. They are an organic compound that contains a carboxyl group (C(O)OH), with the general formula being R-COOH. The R in a fatty acid is made up of only carbon and hydrogen in straight or branched chains and contains no benzene rings. This R component can be quite large, typically in the 12-36 carbon range [56] and can be saturated or unsaturated. That is, they may contain single or double bonds between the carbons, respectively. Stearic acid is a saturated fatty acid and therefore contains no double bonds between carbons. Whereas amino acids join together to make proteins, fatty acids join together to make fats and oils.

Cellular membranes of prokaryotes and eukaryotes are composed of fatty acids, which store energy from carbohydrates. However, not all fatty acids are associated with living organisms. It has been suggested that prebiotic formation of small chain fatty acids was most likely through the reduction of sugars [57].

Stearic acid is found in abundances of up to 30% in animal fat and abundances of $< 5\%$ in vegetable fat [58].

Though fatty acids do exist as free acids, they may also be incorporated into geomolecules (bound to minerals) or larger biomolecules (kerogen). The former process, which occurs in the presence of non-metallic refractory materials (those which maintain strength at high temperature), can preserve the acids long after the biological system that created them has died off.

An important issue with respect to life on Earth is that all organisms use a distinct set of organics as the building blocks for larger and more complex molecules. These include the four nucleotides of DNA, the 20 essential amino acids, and acetate units of fatty acids ($C_2H_3O_2$)[59].

Stearic acid contains 18 carbons. This is important as biosynthesized fatty acids most frequently contain even numbers of carbons. This is because they are formed by adding the acetate units [56] mentioned above and therefore always result in even number of carbons. Though even numbered carbon fatty acids suggest a biological origin, they are not definitive of such an origin. Straight chain fatty acids can be synthesized abiotically, as is seen in low concentrations near hydrothermal geysers. However, the probability that such a long chain as stearic acid can be produced abiotically is very low [60].

Biogenic unsaturated fatty acids are never the trans stereoisomer[56]. The fact that all these molecules are cis would be a definitive biomarker if found in nature. However, stearic acid (saturated) does not have any stereoisomers and therefore does not possess this easily identifiable origin. Fatty acids found in carbonaceous chondrite meteorites or produced synthetically have equal number of trans and cis isomers and are therefore assumed to be of abiological origin.

Stearic acid has been used in other studies as a leading potential biosigna-

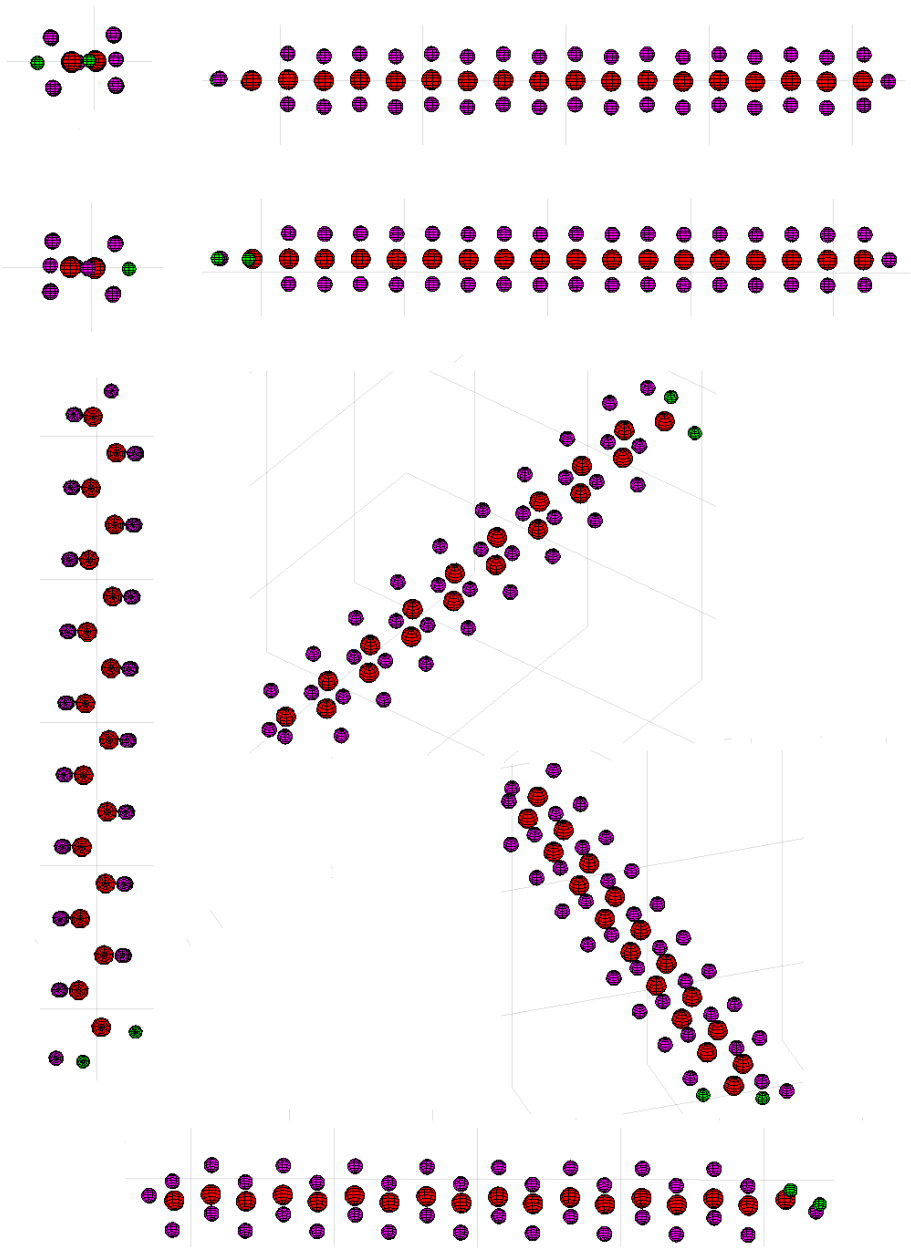

Figure 9: Stearic acid 3D Matlab images made using data file from the ChemEd Java applet[7]. The magenta atoms are hydrogen, the red atoms are carbon, and the green atoms are oxygen. All bonds are single except that between C and O in the carbonyl.

ture as it is present almost everywhere on Earth that life is found. It is also considered more stable than other biosignatures in a Martian environment[40]. Preferential loss of short chain acids has been reported [56] which is important because surface and subsurface Martian biosignatures would, in general, be of low concentration [33], so the fact that losses would affect long chain acids less so is noteworthy.

Richardson et al [60] tested stearic acid in a mixture with the anhydrous sodium sulphate, thenardite. Thenardite is found in arid evaporitic environments and in dry caves. It can also be found as a sublimate deposit around fumaroles. Any of those locations are relevant for Martian astrobiology investigations. Their test did not use Raman spectroscopy to locate stearic acid within the mineral matrix, but instead used laser desorption Fourier transform mass spectrometry.

Since Raman intensity is proportional to the covalency of a bond (directly related to polarizability), the C-C bonds (100% covalent) and the C-H bonds ($>$ 90% covalent) in an organic such as stearic acid are extremely sensitive to Raman spectroscopy [33]. Carbon-carbon bonds are mostly inactive with IR absorption spectroscopy.

## 5.1 Raman peaks in stearic acid

Theoretically, non-linear molecules have 3N-6 normal modes of vibration, where N is the number of atoms in the molecule. Since stearic acid has 56 atoms, this should amount to 162 possible vibrations. Any vibrations that occur because of neighbouring molecules such as with hydrogen bonding would be in addition to this number. Most of these vibrations would be so close in energy that resolving them is impossible with current technology. Note that due to the nature of the long repeating aliphatic chain, the majority of these vibrations will be degenerate.

Stretching vibrations (change in bond lengths) can be either symmetric or asymmetric. Asymmetric stretches are the higher energy of the stretching vibrations. A deformation vibration (change in bond angles) can be a twisting, a scissoring, a rocking, or a wagging. The four deformation motions are shown in Figure 10. Scissoring and rocking are usually the higher energy of the deformation vibrations.

In the tables presented in this chapter, the specific motion of a deformation is mentioned if reported from another source. However, it is usually only listed generically as a 'deformation' since a large molecule with so many vibrations makes it difficult to definitively report which exact deformation is occurring.

### 5.1.1 Methyl and methylene groups

A methyl group consists of a carbon bonded to three hydrogen atoms. In the context of a saturated fatty acid, there is always one methyl group at the opposite end of the aliphatic chain compared to the carboxyl group. Therefore, the

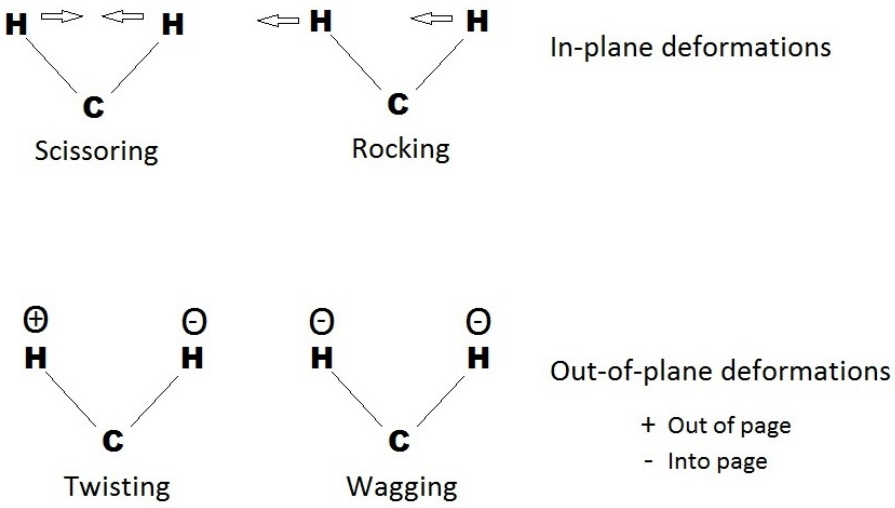


Figure 10: Deformation vibrations for $CH_2$ groups.

| Vibration | Raman shift ($cm^{-1}$) | Relative intensity |
|---|---|---|
| O-H stretch | 3200-3650 | weak |
| -$CH_3$ asymmetric stretch | 2950-3000 | strong |
| -$CH_2$- asymmetric stretch | 2900-2950 | very strong |
| -$CH_3$ symmetric stretch | 2850-2880 | strong |
| -$CH_2$- symmetric stretch | 2840-2870 | very strong |
| C=O stretch | 1640-1750 | medium |
| $CH_2$ symmetric bend | 1400-1500 | medium |
| C-OH bends | 1400-1450 | weak |
| $CH_3$ asymmetric bend | 1400-1450 | medium to weak |
| C-$CH_3$ symmetric bend | 1350-1400 | medium to weak |
| $CH_2$ in phase twist | ~1300 | medium |
| C-OH stretch | 1050-1250 | medium |
| C-C stretch of aliphatic chain | 850-1200 | strong |
| Deformations of aliphatic chain | 150-800 | medium to weak |

Table 1: Typical spectral regions for vibrations in general saturated fatty acids [3, 4].

| Vibration | Raman shift ($cm^{-1}$) |
|---|---|
| $CH_2$ in phase stretch | 2881 |
| $CH_2$ out of phase stretch | 2846 |
| 'not identified' | 1569 |
| $CH_2$ bend | 1461 |
| $CH_2$ bend | 1441 |
| 'not identified' | 1370 |
| $CH_2$ in phase twist | 1296 |
| 'not identified' | 1176 |
| C-C-C ($CH_2$ chain) in phase stretch | 1130 |
| C-C-C ($CH_2$ chain) out of phase stretch | 1063 |
| 'not identified' | 1103 |
| 'not identified' | 959 |
| 'not identified' | 937 |
| 'not identified' | 891 |

Table 2: Stearic acid Raman bands reported by Larkin[4]. Intensities were not reported.

| Vibration | Raman shift ($cm^{-1}$) | Relative intensity |
|---|---|---|
| $CH_2$ in phase stretch | 2896 | very strong |
| 'not identified' | 2740 | shoulder |
| 'not identified' | 2444 | weak |
| 'not identified' | 2202 | weak |
| C=O stretch | 1658 | medium |
| $CH_2$ deformation | 1457 | 'not reported' |
| $CH_2$ deformation | 1309 | medium |
| $CH_2$ deformation | 1174 | shoulder |
| C-C stretch | 1137 | medium |
| C-C stretch | 1072 | medium |
| $CH_3$ rocking | 882 | 'not reported' |
| 'not identified' | 681 | 'not reported' |
| 'not identified' | 588 | 'not reported' |

Table 3: Stearic acid Raman bands reported by Eshelman[5].

fourth bond of the carbon in the methyl group is to the adjacent carbon in the chain.

A methylene group consists of a carbon bonded with two hydrogen atoms. In the context of a saturated fatty acid, methylene groups make up the remainder of the aliphatic chain between the methyl group and the carboxyl group. The two remaining bonds of the carbon are to the adjacent carbon atoms on each side.

Methyl bends can often occur around 1465 $cm^{-1}$. Methyl and methylene twists can occur near 1300 $cm^{-1}$. A rocking motion is observed in some IR spectra at 723 $cm^{-1}$, but it is unclear whether it is found in Raman spectra as well as we did not observe that peak. The in-phase bend of a single methyl results in a band at approximately 1375 $cm^{-1}$ in the IR. Methyl groups have doublet stretching bands between 2950-2975 $cm^{-1}$ and 2860-2890 $cm^{-1}$, while methylene groups have doublet stretching bands between 2910-2940 $cm^{-1}$ and 2840-2870 $cm^{-1}$[4], the doublet being that the higher energy vibration is the asymmetric stretch and the lower energy vibration is the symmetric stretch.

The relative intensities of these bands are indicative of the ratio of methyl to methylene groups and could possibly be used to determine the length of certain aliphatic chains. Deconvolving these overlapping bands using Gaussian and Lorenzian functions to simulate the individual bands may be possible for small chain compounds, but not so for longer chains such as stearic acid. This is because, where small chains would likely have only the four stretching bands, larger molecules would have a higher probability of producing additional bands due to Fermi resonance (discussed in section 5.1.3) for which it is difficult to estimate both band shape and position. Also, in a chain with many methylene groups, individual methylene units may not all vibrate at the same frequency or produce the same peak shape. This is because the adjacent groups to each unit (methyl, methylene, or carboxyl) will have a slight effect on their frequency and so may surrounding molecules.

### 5.1.2 Carbonyl section of carboxyl group

The carbonyl section of a carboxyl group is the double bonded pair of the lone oxygen and the carbon.

The carbonyl C=O stretch in an organic molecule is typically weak to moderate and may occur over a large range from approximately 1550-1900 $cm^{-1}$, depending on the molecule. However, in a carboxylic acid such as stearic acid, this range is usually decreased to 1640-1750 $cm^{-1}$. Larkin [4] states that the C=O stretch in a carboxylic acid results in a Raman band at approximately 1660 $cm^{-1}$. An interesting thing to note about this band is that it decreases in frequency the longer the aliphatic chain. A similar observation is presented in section 5.3.2 concerning the lowest frequency observable chain deformation band.

The C=O band is predicted to be weak since it is a more polar bond compared to C-C or C-H bonds, thus resulting in lower polarizability. The polarity of the bond is a result of the oxygen being more electronegative than the carbon.

Larkin [4] suggests that the frequency of the carbonyl (C=O) stretch redshifts due to hydrogen bonding. The band can also become broader due to hydrogen bonding. Overtones from carbonyl bands may occur between 3200 and 3500 $cm^{-1}$, but most are probably too weak to be detected.

### 5.1.3 Hydroxyl section of carboxyl group

The hydroxyl section of a carboxyl group is the carbon single bonded to the other oxygen which is also bonded to a hydrogen.

Bands from the C-OH bends can be observed near 1400-1450 $cm^{-1}$. Since this is a weaker peak and this region overlaps with C-H deformations, it is likely this peak will not be observable. The bands from the O-H stretch usually occur at wavenumbers greater than 3600 $cm^{-1}$.

### 5.1.4 Fermi-resonance in stearic acid

Vibrations in different sections of a molecule can be almost completely isolated if their vibrational frequencies are significantly different from the groups adjacent to them. As discussed in the Raman theory chapter, the frequencies associated with these localized vibrations are called group frequencies. Under some conditions though the vibrations of neighbouring groups are not well separated. These vibrations can interact leading to Fermi-resonance.

In the context of stearic acid, this means that an overtone of a bending vibration from a methylene interacts with the symmetric stretching mode of a neighbouring methylene. This results in a doublet which straddles the position of the original stretch. Since stearic acid has many neighbouring equivalent methylene groups, it can be expected that additional bands will result from Fermi-resonance around the main C-H stretch peak location. As stated in the section on methyl and methylene groups, since there are an unknown but large number of overlapping bands in the region around 2900 $cm^{-1}$, it is impossible to deconvolve the bands to see what exactly makes up the large broad band.

The 'straddling' (bands occurring at either side of the main stretching peak) is due to a quantum mechanical mixing phenomenon and only occurs if the overtone of the bend and the normal mode of the stretch are almost coincident in energy [4]. A simple description of the result is that the higher energy of the two modes (overtone bend and normal stretch) will blueshift, while the lower energy mode red-shifts. While this occurs, the weaker mode becomes more intense and the stronger mode becomes less intense as seen in Figure 11. In general, the overtone will be the weaker mode.

Although the observer of the spectrum sees a doublet where they previously may have only seen a single peak, the number of peaks has actually not changed. In this case it would be just that the two modes involved in the Fermi-resonance were so coincident in energy that they overlapped prior to the quantum mechanically mixing.

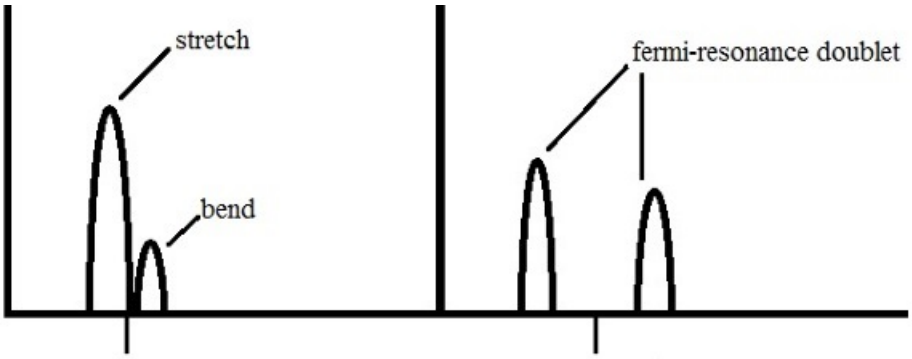


Figure 11: Bands due to normal stretch and bending overtone a) before and b) after Fermi-resonance phenomenon.

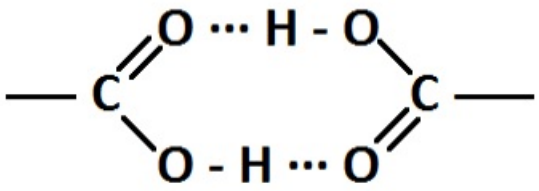


Figure 12: Dotted lines represent hydrogen bonding between two carboxylic acids.

### 5.1.5 Additional band made possible due to hydrogen bonding

A low frequency ($<$1000 cm$^{-1}$) band may be observed due to hydrogen bonding in a carboxylic acid[4] in addition to the 3N-6 regular modes. It involves bending of the H-Y bond. As discussed in chapter 2 on Raman theory, the H-Y bond is the electrostatic bond in the X-H-Y system. It is the OH-O out-of-plane bend that would be relevant to stearic acid. In Figure 12, hydrogen bonding is shown between two carboxyl units.

## 5.2 Band broadening in stearic acid

Hydrogen bonding in the carboxylic acid can not only create the new band mentioned in section 5.1.5, but may also broaden the pre-existing O-H and C-OH stretching bands as well as the C=O stretch. How closely adjacent stearic acid molecules are packed would determine how much this hydrogen bonding affects the broadening.

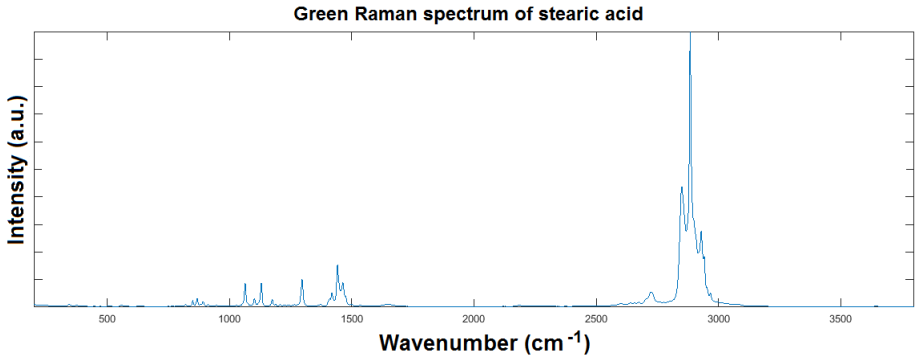


Figure 13: Raman spectrum of stearic acid at 532 nm excitation with a commercial Raman microscope.

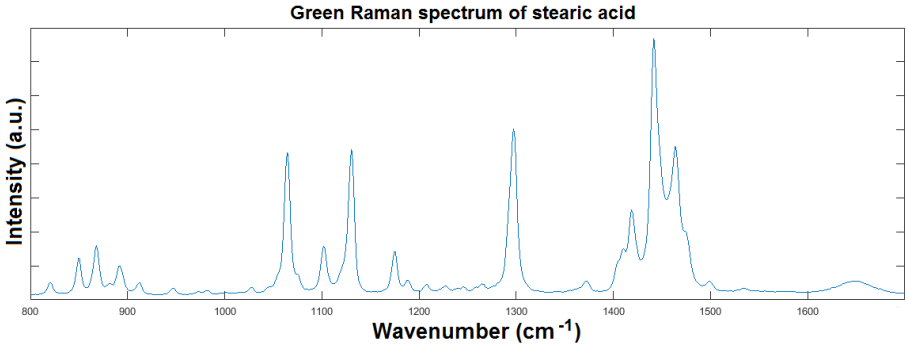


Figure 14: Raman spectrum of stearic acid at 532 nm excitation with a commercial Raman microscope, zoomed in to show a smaller fingerprint window.

## 5.3 Stearic acid results

Next we present the Raman spectral data obtained for stearic acid at green excitation.

The dominant feature is between 2800 and 3000 $cm^{-1}$. This is a region of many different overlapping stretches involving C-H bonds. Since the C-H stretching region is so intense, it is difficult to see the lower energy vibrations in the full Raman window shown in Figure 13 even though they too are significant. In Figure 14 we present a zoomed portion of the region from 800-1700 $cm^{-1}$. Note the broadness due to hydrogen bonding on the C=O stretching peak at 1649 $cm^{-1}$. Also, though an additional weak band $< 1000$ $cm^{-1}$was anticipated from an OH-O bend resulting from hydrogen bonding, it is unclear that one would be able to differentiate such a band from the many deformations of the aliphatic chain in that region.

Next we present the Raman spectral data obtained for stearic acid at UV

| Vibration | Raman shift ($cm^{-1}$) | Relative intensity |
|---|---|---|
| O-H stretch | 3644 | weak |
| -$CH_3$asymmetric stretch | 2967 | weak |
| -$CH_3$ symmetric stretch | 2940 | weak |
| -$CH_2$ asymmetric stretch | 2929 | medium |
| -$CH_2$ symmetric stretch | 2884 | very strong |
| -$CH_2$ symmetric stretch | 2849 | medium |
| Fermi resonance C-H bend overtone* | 2723 | medium |
| Fermi resonance C-H bend overtone* | 2704 | shoulder |
| 'not identified' | 2673 | shoulder |
| 'not identified' | 2657 | weak |
| 'not identified' | 2641 | weak |
| 'not identified' | 2600 | weak |
| 'not identified' | 2183 | weak |
| C=O stretch | 1649 | weak and broad |
| -$CH_3$symmetric bend | 1466 | medium |
| -$CH_2$symmetric bend | 1442 | medium |
| -$CH_2$symmetric bend | 1420 | medium |
| C-$CH_3$ symmetric bend | 1373 | weak |
| -$CH_2$twist | 1298 | medium |
| C-OH stretch | 1175 | weak |
| C-C ($CH_2$ chain) stretch | 1130 | medium |
| C-C ($CH_2$ chain) stretch | 1103 | weak |
| C-C ($CH_2$ chain) stretch | 1065 | medium |
| C-C ($CH_2$ chain) stretch | 1028 | weak |
| C-C ($CH_2$ chain) stretch | 946 | weak |
| C-C ($CH_2$ chain) stretch | 912 | weak |
| -$CH_3$rocking | 892 | weak |
| C-C ($CH_2$ chain) stretch | 882 | weak |
| C-C ($CH_2$ chain) stretch | 868 | weak |
| C-C ($CH_2$ chain) stretch | 849 | weak |
| C-C ($CH_2$ chain) stretch | 820 | weak |
| Deformations of aliphatic chain | 633 | weak |
| Deformations of aliphatic chain | 573 | weak |
| Deformations of aliphatic chain | 560 | weak |
| Deformations of aliphatic chain | 519 | weak |
| C-C=O deformation* | 505 | weak |
| Deformations of aliphatic chain | 447 | weak |
| Deformations of aliphatic chain | 408 | weak |
| Deformations of aliphatic chain | 376 | weak |
| Deformations of aliphatic chain | 343 | weak |

Table 4: Stearic acid green Raman bands from this study. (*uncertain, but probable)

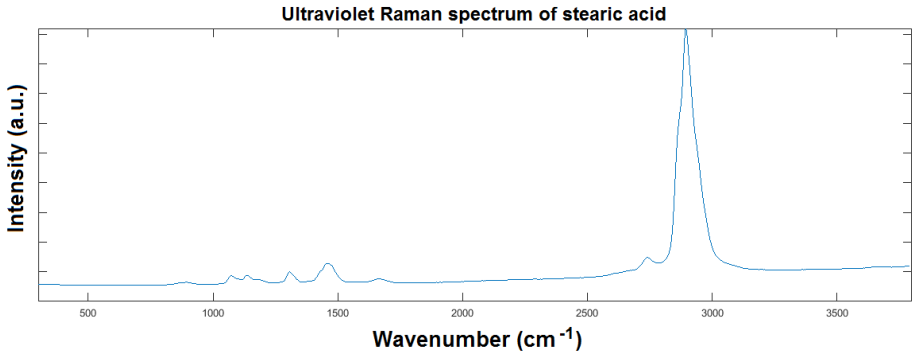


Figure 15: Raman spectrum of stearic acid at 266 nm excitation with a prototype in-situ stand off Raman system.

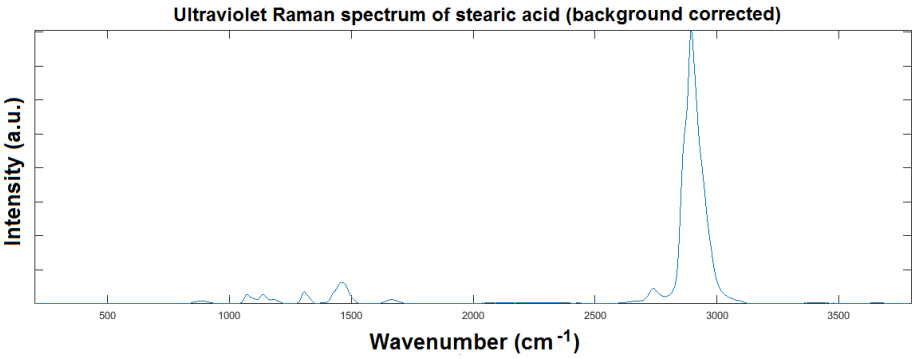


Figure 16: Raman spectrum of stearic acid at 532 nm excitation with a prototype in-situ stand off Raman system, corrected for minor amounts of fluorescence.

excitation (Figure 15).

The dominant feature in the UV is still between 2800 and 3000 $cm^{-1}$. However, with the poorer resolution of the UV system, the band comes across as a superposition of many C-H vibrations including both $CH_2$ and $CH_3$ stretches. The Fermi resonance previously mentioned as occurring in this region further complicates attempts to separate this region into constituent bands.

The same zoomed section (800-1700 $cm^{-1}$) with the poorer resolution of the prototype in-situ system shown in Figure 17 displays significantly fewer Raman bands than the same window for the commercial Raman microscope.

In all of the data tables for stearic acid we see multiple bands assigned to a single vibration type. Though that may seem counter intuitive, there is a good explanation. As mentioned in the section on methyl and methylene groups, not all C-C and C-H bonds are equal. Pending where those bonds occur in the molecule, they can have different bond lengths and angles, thereby

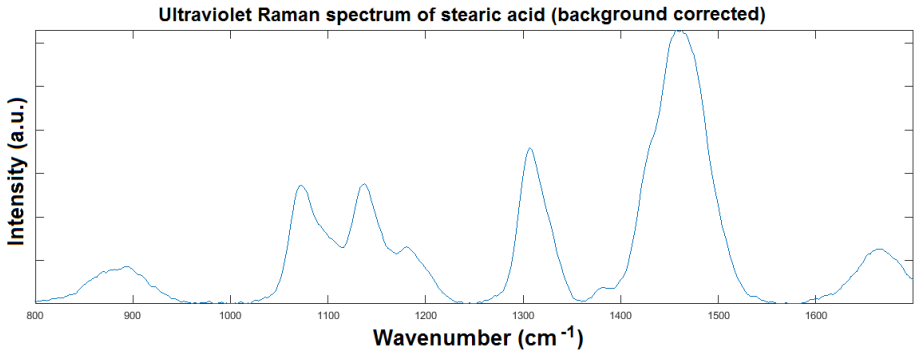


Figure 17: Raman spectrum of stearic acid at 266 nm excitation with a prototype in-situ stand off Raman system, corrected for fluorescence and zoomed in to show a smaller fingerprint window.

| Vibration | Raman shift ($cm^{-1}$) | Relative intensity |
|---|---|---|
| O-H stretch | 3666 | weak |
| $CH_3$and $CH_2$ anti + symmetric stretch | 2895 | very strong |
| Fermi resonance C-H bend overtone* | 2741 | strong |
| 'not identified' | 2444 | weak |
| 'not identified' | 2210 | weak |
| C=O stretch | 1662 | weak and broad |
| -$CH_2$symmetric bend | 1457 | strong |
| -$CH_3$ asymmetric bend | 1380 | shoulder |
| -$CH_2$deformations | 1307 | strong |
| -$CH_2$deformations | 1181 | shoulder |
| C-C ($CH_2$ chain) stretch | 1138 | medium |
| C-C ($CH_2$ chain) stretch | 1072 | medium |
| -$CH_3$rocking | 892 | broad and weak |
| Deformations of aliphatic chain | 563 | weak |
| Deformations of aliphatic chain | 340 | weak |

Table 5: Stearic acid UV Raman bands from this study (*uncertain, but probable).

leading to different force constants. Also, as discussed in the section of chapter 3 concerning hybridization of carbon atoms, not all carbons will be holding on to electrons with the same strength and therefore those electrons will be shared differently between the atoms in the bond. The methyl group at one end of the stearic acid molecule has a carbon that is $sp^3$ hybridized and the same is true for the rest of the chain (methylene groups) except the final carbon. The carbon which as part of the carboxyl functional group is $sp^2$ hybridized.

### 5.3.1 Uncertain region from 2100-2700 $cm^{-1}$

There are no functional groups in stearic acid that should produce first order vibrations with a Raman shift in the 2100-2700 $cm^{-1}$ range. This is usually the region where triple bonds would produce stretching peaks, but there are no triple bonds in stearic acid. Since we do observe bands in this region, they are marked as "not identified" in our tables. However, there may be an explanation for their presence. They could be overtones of lower frequency deformations or they could be combination bands. Usually, overtones which are not involved in Fermi resonances are very low in intensity. All of the unidentified peaks in this region are also weak.

### 5.3.2 Lowest frequency observable band as chain length identifier

The lowest frequency observed was 340 $cm^{-1}$ in the UV and 343 $cm^{-1}$ in the green. A frequency this low was not reported by either Larkin[4] or Eshelman[5]. However, other studies have observed that this weak low frequency vibration will redshift in fatty acids with an increase in carbon backbone length. Starting from 10 carbon chains and going up by two carbons at a time to 16 carbons, the saturated fatty acids are capric acid, lauric acid, myristic, and palmitic acid. These lowest observable bands for these molecules are at 486 $cm^{-1}$, 459 $cm^{-1}$, 407 $cm^{-1}$, and 365 $cm^{-1}$, respectively[61]. By adding two more carbons to obtain stearic acid one would expect the vibrational frequency to follow the downward trend as seen in Figure 18. Our data follows this trend well. We suggest here that if a Raman spectrum observed in the field for a suspected saturated fatty acid is clear enough to observe the weak low frequency vibrations, this peak may be indicative of chain length and therefore aid in fingerprinting the molecule.

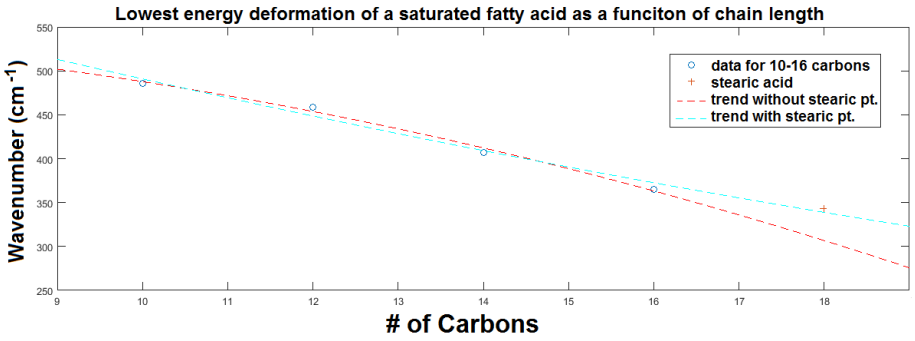


Figure 18: Decrease in energy of lowest energy deformation vibration in saturated fatty acids from C=10 to C=18.

# 6 Aqueous alteration minerals

On Earth, liquid water is a necessary condition for life. If one is to search for evidence of life where there is no lasting water, such as the surface of Mars, it would be optimal to look at locations where the minerals had to form in the presence of water.

Secondary minerals such as hydrated sulphates and phyllosilicates have been identified on Mars[62][29] [30]. The vast distribution of these aqueous alteration minerals is evidence of large amounts of water during the Martian past. Subsurface liquid water may still exist on Mars. As mentioned in chapter 1, there is now evidence that surface water can exist in the form of brines on the surface. Perchlorates and chloride bearing salts may depress the freezing point of water[14] so that this liquid state is possible at the low atmospheric pressure on the Martian surface. These brines may have provided or may continue to provide a habitable environment, though not continuously at the surface.

The secondary minerals used in this study all contain either water layers, structural water, or structural OH groups. This means that they have increased relevance to astrobiology. In extreme environments on Earth which could be considered Mars analogue sites, cyanobacteria have been found to live in the crevasses [5] of gypsum and therefore that mineral has the potential to be a habitable environment for microorganisms on Mars.

Water is needed as a solvent for many chemical reactions to occur. It can absorb heat without a large rise in its temperature and it exists as a liquid over a larger range of temperatures than other potential biological solvents. Water has a high dielectric constant compared to many other liquids which means that two oppositely charged ions are more shielded from one another and can therefore be dissolved into solution more readily, thereby allowing them to be involved in chemical reactions [57].

For our aqueous alteration minerals we selected from both hydrated sulphates and phyllosilicates. The sulphates were the dominant Martian calcium

sulphate, gypsum, and the dominant Martian iron sulphate, jarosite. Note that there exist various forms of jarosite. While gypsum contains only the cation calcium, jarosite has a second cation to iron in the structure which can be $K^+$, $Na^+$, $Ag^+$, $H_3O^+$, $NH_4^+$, or $Pb^{2+}$. This study used natrojarosite, which contains sodium cations. This is important because Klingelhofer et al [29] showed by using the Mossbauer spectrometer on the Mars Exploration Rover Opportunity that the jarosite encountered on the Martian surface was mostly likely the $K^+$or $Na^+$cation versions within that mineral group. A synthetic gypsum was used in our study to establish a control mineral with no impurities or transition metals. The effect of transition metals either as structural components or as impurities on UV Raman and reflectance spectra will be discussed in chapter 7. Note that all the clays likely started with some organic contamination. All have a weak broad peak near the C-H stretching region and all have large amounts of fluorescence using green excitation. Terrestrial clays are known to be have high organic content.

The tetrahedral-octahedral (T-O) layered clay kaolinite was selected, as well as the tetrahedral-octahedral-tetrahedral (T-O-T) layered clays montmorillonite and nontronite. All three have been detected on Mars [63, 64].

## 6.1 Minerals and abiogenesis

We refer to the process of life arising from non-living matter, such as simple organic compounds, as abiogenesis. The study of abiogenesis considers chemical, geophysical, and biological aspects of how self-replicating molecules came into existence. Stanley Miller and Harold Urey demonstrated in an environment similar to the presumed early Earth that many amino acids and complex organics can be synthetically produced from inorganic compounds and simple organics by catalyzing them with a spark to simulate lightning[65].

As introduced in chapter 3, the clay montmorillonite can act as a catalyst for both the formation of larger molecules such as membranes from lipids and the polymerization of ribonucleic acid (RNA). Montmorillonites allow time for chemical bonding of smaller organics by holding the organics in place while in aqueous solution. It has been suggested that prior to the development of cell walls (which within their structure allow the reproduction of DNA and RNA), early RNA was produced in the presence of montmorillonite. At room temperature, James Ferris[24] mixed simple organics and nucleotides with montmorillonite to synthesize longer RNA molecules in the laboratory. This proved that this process could happen and allowed montmorillonite to be postulated as a potential catalyst for the beginning of life on Earth. Note that it is generally accepted that all current terrestrial life descended from RNA.

Sheet structure in clays can vary from one layer to the next by replacement of cation type. It has been suggested that this variability may allow clays to act as 'mineral genes', providing a template for the formation of a new clay layer, passing on information from the parent clay.

Nontronite, an iron smectite, can act as a chemical energy source for microscopic bacteria deep in the ocean where they cannot access the energy of the

| Vibration | Raman shift ($cm^{-1}$) | Relative intensity |
|---|---|---|
| O-H asymmetric stretch | 3200-3600 | medium |
| O-H symmetric stretch | 3100-3500 | medium |
| $H_2O$ bending overtone | 3000-3250 | weak |
| $H_2O$ bending | 1500-1700 | very weak |
| $SO_4$ asymmetric stretch | 1140-1200 | medium |
| $SO_4$ asymmetric stretch | 1080-1130 | medium |
| $SO_4$ symmetric stretch | 970-1070 | strong |
| $SO_4$ in plane bend | 550-700 | weak |
| $SO_4$ out of plane bend | 400-530 | weak |
| $H_2O$ translation | 150-350 | weak |
| O-cation-O lattice | $< 300$ | weak |

Table 6: Typical spectral regions for vibrations in hydrated sulphates [4, 6].

sun. Microtubules in nontronite samples from white smoker chimney locations at mid ocean ridges suggest that bacteria are somehow feeding from the iron in the clay[27].

Pyrite may also be an important mineral surface for chemical reactions related to biochemical processes. Though pyrite itself was not studied here, we will see in the next section how pyrite can be a precursor to sulphates.

## 6.2 Hydrated sulphates

Evaporitic minerals on the surface of Mars could serve as habitable environments for adapted microorganisms. It is possible that these evaporitic minerals could sustain molecular remnants of extant or extinct Martian life. Hydrated sulphates are often evaporitic minerals and therefore we focus our study on that subgroup of evaporites.

The Mars Exploration Rovers Opportunity and Spirit have confirmed the presence of hydrated sulphates on the surface of Mars [66]. Mini-TES and APXS instruments have performed experiments which lead team scientists to consider that magnesium sulphates are the dominant sulphates on the Martian surface. The predicted dominant surface and subsurface magnesium sulphates are kieserite ($MgSO_4$-$H_2O$) and hexahydrite ($MgSO_4$-$6H_2O$), respectively. Neither of these minerals remain in their hydration state at Earth standard atmospheric conditions and are therefore difficult to work with in the lab setting.

After magnesium sulphates, the next dominant hydrated sulphates on Mars are predicted to be the calcium sulphate[67], gypsum, and the iron sulphate group, jarosite. Orbital data from the Mars Reconnaissance Orbiter and the Mars Express orbiter corroborate the presence of these minerals[66]. While jarosite deposits are more localized, gypsum has been found in vast areas by the OMEGA instrument on the Mars Express orbiter[66].

Table 6 lists typical spectral regions for Raman bands from hydrated sulphates. The cation for each sulphate can change the environment within which

the sulphate ion and the water/hydroxyls exist. Therefore, cation type can alter the energies of the sulphate ion internal vibrations. However, the bond between the cation and the sulphate ions is too polar to allow much if any Raman scattering and therefore we see almost no bands associated with the cation.

### 6.2.1 Gypsum

**Calcium sulphate dihydrate - $CaSO_4$-$2H_2O$**

Gypsum is a common mineral found in evaporite deposits, dry caves, near volcanic vents, as an evaporative precipitate in lakes with high salinity, and less frequently in hydrothermal sulphide deposits which have been oxidized. Most frequently, it is found in layered sedimentary deposits in close proximity to anhydrite, calcite, and halite. It is often formed from the hydration of anhydrite. Gypsum may also form when calcium carbonates come in contact and react with sulphuric acid. This acid can form when sulphur dioxide, outgassed from volcanoes, is converted to $H_2SO_4$ in the presence of water. The acid falls to the surface as acid rain. The acid may also be a product of oxidation of sulphides in aqueous solution. As the water evaporates away, gypsum remains as an evaporite.

Gypsum is composed of layers of water alternating with layers of edge sharing $SO_4$and $CaO_8$polyhedra. Calcium atoms are bonded to six oxygens from sulphate tetrahedra and two oxygens from water. The water binds layers together through hydrogen bonding [68] (Figure 20). None of the oxygen atoms in the sulphate tetrahedra come from the water.

Next, we present spectral data for gypsum from the commercial Raman microscope at 532 nm excitation (Figure 20). The green data was taken as ~15 minute accumulations.

The most intense peak occurs at 1011 $cm^{-1}$ and corresponds to the symmetric stretch of the sulphate ion. The less intense band at 1138 $cm^{-1}$ corresponds to the antisymmetric stretch of that ion. Bands at 418 and 496 $cm^{-1}$ and 622 and 673 $cm^{-1}$ correspond to bending modes. The first two, out-of-plane bends, and the last two, in-plane bending modes. These values correspond with published data by Skulinova et al [18] for natural gypsum samples. Smith and Dent [69] reported the asymmetric stretch at 1135 $cm^{-1}$, the symmetric stretch at 1009 $cm^{-1}$, the in-plane bends at 629 and 669 $cm^{-1}$, and the out-of-plane bends at 415 and 491 $cm^{-1}$. In both studies the differences between our values and their values are within the uncertainty of the measurements. See Figure 21 for visual depictions of these vibrations.

The water symmetric and asymmetric stretches were observed at 3407 and 3495 $cm^{-1}$, respectively. Kristnamurti and Soot [6] reported similar values of 3400 $cm^{-1}$ and 3500 $cm^{-1}$. The previously mentioned hygroscopic nature of this synthetic sample is enough of a reason for observed shifts in water bands.

Difficult to see on the above plot is an extremely weak band 320 $cm^{-1}$. This peak is not listed in published data. We propose that this is a vibration of the calcium atom and the oxygen atoms it is bonded to. Firstly, the published data

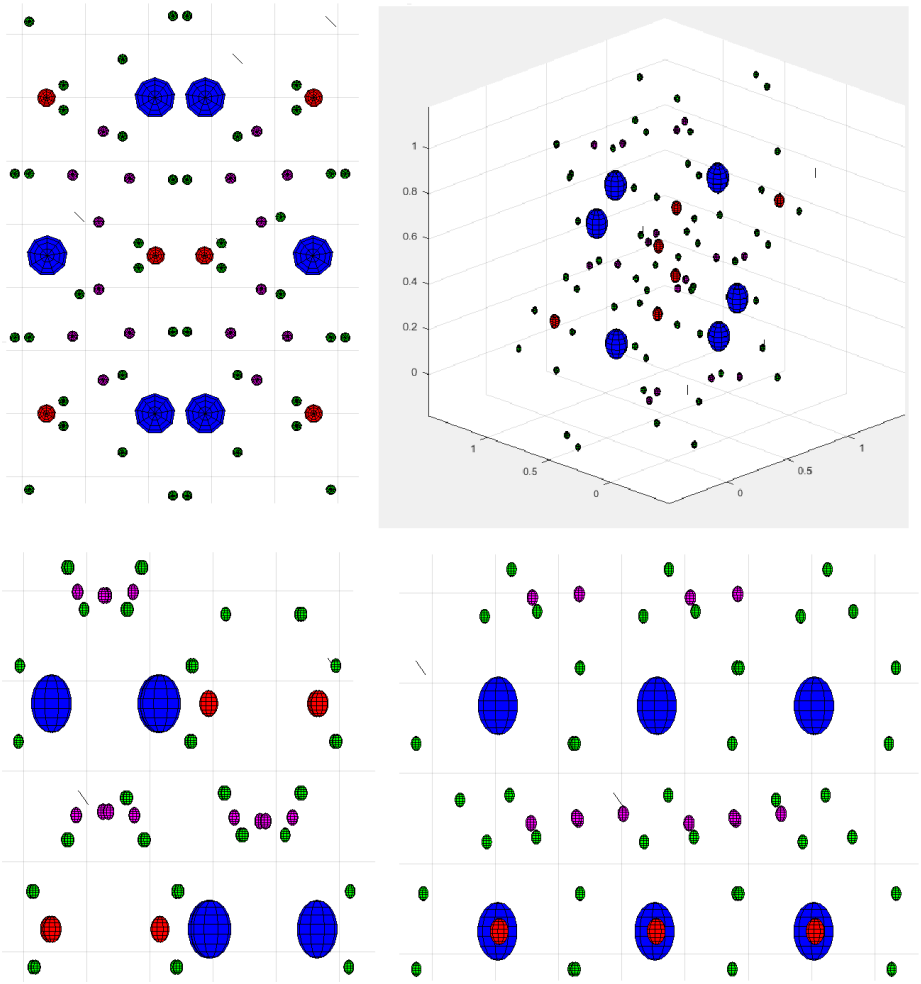


Figure 19: Gypsum 3D Matlab images made using data file from the American Mineralogist Crystal Structure Database[8]. The magenta atoms are hydrogen, the red atoms are sulphur, the green atoms are oxygen, and the blue atoms are calcium.

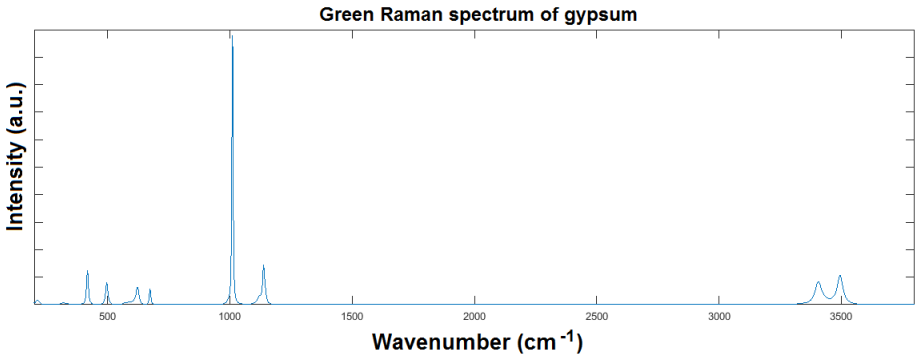


Figure 20: Raman spectrum of gypsum at 532 nm excitation with a commercial Raman microscope.

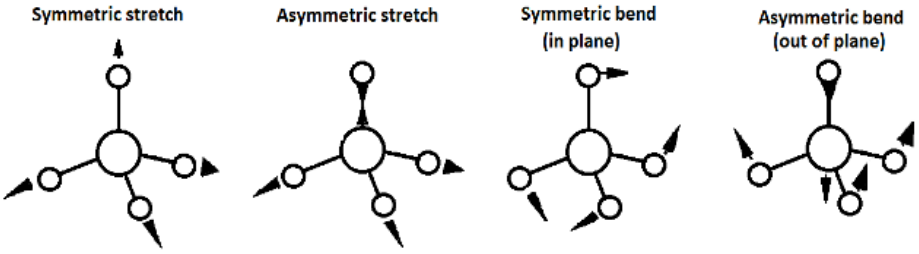


Figure 21: Vibrational modes of the sulphate ion.

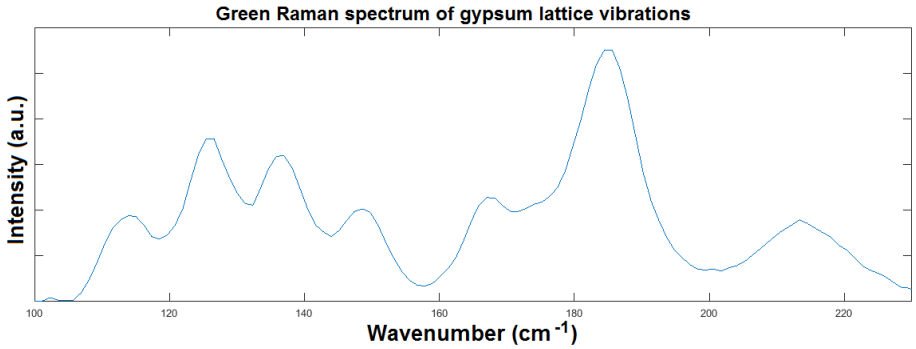


Figure 22: Low energy lattice vibrations of gypsum at 532 nm excitation with a commercial Raman microscope.

does not mention calcium in any of the observed bands, so a correlation of a new band to a vibration would want to consider calcium. Secondly, a calcium-oxygen bond is quite polar compared to all of the other bonds in gypsum which would explain the low Raman intensity compared to other more covalent bands.

Krishnamurti and Soot [6] report a lattice vibration at 183 $cm^{-1}$. The presented spectra in Figure 21 does not go that low in wavenumber. This study was comparing the green and UV spectra and our UV experimental setup does not allow for very low energy bands to be observed. Therefore, we opted to leave out that region for our full window green spectra. However, in Figure 22 we present the green excitation lattice vibrations observed with the commercial Raman microscope. We observe seven Raman bands, including the one band previously reported at 183 $cm^{-1}$[6].

Next, we present the gypsum spectral data from the prototype in-situ stand-off Raman system at 266 nm excitation (Figure 23). The UV data was taken as ~22 minute accumulations. Additional measurement parameters for the UV system are available in the appendices.

Comparing the UV plot in Figure 23 to that with green excitation, the sulphate stretching peaks were shifted to slightly higher frequencies at 1018 and 1146 $cm^{-1}$. The two out-of-plane bending modes remained the same, while the in-plane bending modes were similar at 622 and 675 $cm^{-1}$. The water symmetric and asymmetric stretches were found at 3422 and 3507 $cm^{-1}$, respectively. These shifts are attributed to the hygroscopic nature of the sample as the green and UV Raman experiments were not performed in the same laboratory or on the same day. The final result is a superposition of both water types (adsorbed and structural).

The difficult-to-observe band at 320 $cm^{-1}$ with green excitation is also difficult to observe with UV excitation. The UV spectrum has the vibration located at 323 $cm^{-1}$.

It can easily be seen that the relative intensities of bands in the green and UV are not the same. This is most likely the polarization dependence factor as

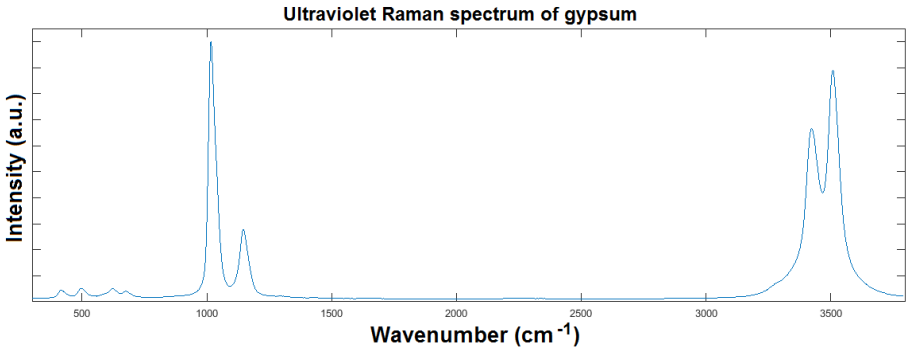


Figure 23: Raman spectrum of gypsum at 266 nm excitation with a prototype in-situ stand off Raman system.

mentioned in chapter 2. Raman spectra of crystals can be polarization dependent and this affects each vibration differently. That issue is not investigated in this study because the spot size of our UV system is much larger than the sample grain sizes. If the particles are randomly aligned, then statistically, we should not observe any difference from one UV spectrum to the next. However, the commercial Raman microscope has a much smaller spot size and therefore, could be affected by alignment of the gypsum crystals in the viewing area. Due to the large difference in spot sizes between systems (polarization dependence), we must ignore relative peak heights between green and UV excited mineral spectra.

### 6.2.2 Natrojarosite

**Sodium iron sulphate hydroxide - $NaFe_3(SO_4)_2(OH)_6$**

Iron and sulphur combine to make the sulphide pyrite. When pyrite and primary basalts come in contact with an acidic aqueous solution they can form iron sulphates such as natrojarosite. This usually occurs downstream of the weathered sulphides[31]. The source of the water can be from high temperature hydrothermal vents or geysers, whose water is from deep below the planet's surface. This subsurface water is heated by nearby magma from recent or ongoing volcanism and jarosite group minerals require warm water during formation. Acid rainwater dissolves salts and organic acids, causing it to lead to even more acidic groundwater. The reactions from this acidity provide many of the mineral nutrients in soils required for plant growth[70].

Solutions with lower pH are more acidic. The pH scale ranges from 0-14 and a pH of 3 or less is needed to form jarosite group minerals. A solution is more acidic when more hydrogen bonds to an anion such as $Cl^-$ or $SO_4{}^-$. If hydrogen bonds to the sulphate anion, it forms sulphuric acid ($H_2SO_4$).

Iron sulphates may also form from the weathering of iron rich phyllosilicates, such as nontronite. As opposed to the sulphur coming from the initial mineral

such as discussed above with pyrite, nontronite contains no sulphur and thus the sulphur would have to come from sulphuric acid in solution. The stratigraphy in certain locations on Mars suggests that this is the dominant formation process in the jarosite observed by CRISM on the MRO orbiter[31].

Though major jarosite deposits are assumed to be localized on the surface of Mars, it is suggested [62] that jarosite is an integral component in the globally mobilized dust, thereby spreading small amounts of the mineral around the planet.

Klingelhofer et al [29] showed by using the Mossbauer spectrometer on the Mars Exploration Rover Opportunity that the jarosite encountered on the Martian surface was most likely made up of $K^+$or $Na^+$cations. Jarosite $KFe_3(SO_4)_2(OH)_6$, natrojarosite $NaFe_3(SO_4)_2(OH)_6$, and hydronium-jarosite $(H_3O)Fe_3(SO_4)_2(OH)_6$ have all been found in Martian meteorites [71]. Weathering of Martian basalts in the presence of an acidic oxidizing fluid could lead to these sulphates in the meteorites. It has yet to be determined if Pb-jarosite, ammonium-jarosite, or argento-jarosite exist on Mars.

Frost et al[72]stated that infrared spectroscopy has failed to distinguish between the various forms of jarosite and that X-ray diffraction of that mineral group is difficult since jarosites are often poorly crystalline.

All of the iron in jarosite is trivalent $Fe^{3+}$. Iron-oxygen distances in jarosite are dependent on which section of the crystal the oxygen is shared with. As seen in Figure 24, all of the iron is located in an asymmetric octahedral coordination, meaning that it bonds to six anions which are not all the same. The bonds with the sulphate ion are longer than the bonds to neighbouring octahedra or the sodium cation.

Next, we present the spectral data for natrojarosite from the commercial Raman microscope at 532 nm excitation (figure 25).

An intense peak occurs at 1009 $cm^{-1}$ and corresponds to the symmetric stretch of the sulphate ion. The more intense band at the higher wavenumber of 1112 $cm^{-1}$ corresponds to the antisymmetric stretch of that ion. A second antisymmetric stretch is located at 1152 $cm^{-1}$ and is presumed to be caused by a degeneracy splitting of that stretch in the presence of the sodium cation. Published data[73] places the symmetric stretch at 1010 $cm^{-1}$ and the two antisymmetric stretches at 1109 and 1151 $cm^{-1}$, in good agreement with our data. It is interesting to note that the sulphate asymmetric stretch is more intense than the symmetric stretch which is the opposite of most sulphates. This could be a polarization dependence issue due to the small spot size of the Raman microscope, resulting in non-randomly oriented particles in the field of view. A band at 622 $cm^{-1}$ corresponds to an in-plane bending mode and a band at 445 cm-$^{-1}$ corresponds to an out-of-plane bending mode of the sulphate ion. These agree well with published values by Sasaki et al [74] of 625 and 451 $cm^{-1}$, respectively. Bands observed at 227, 292, and 364 $cm^{-1}$ correspond to O-Fe stretching modes that agree well with their data. There is one peak observed at 536 $cm^{-1}$. This may be a librational mode of the water, whereby it rotates back and forth.

The natrojarosite data presented above appears to be noisier than the green

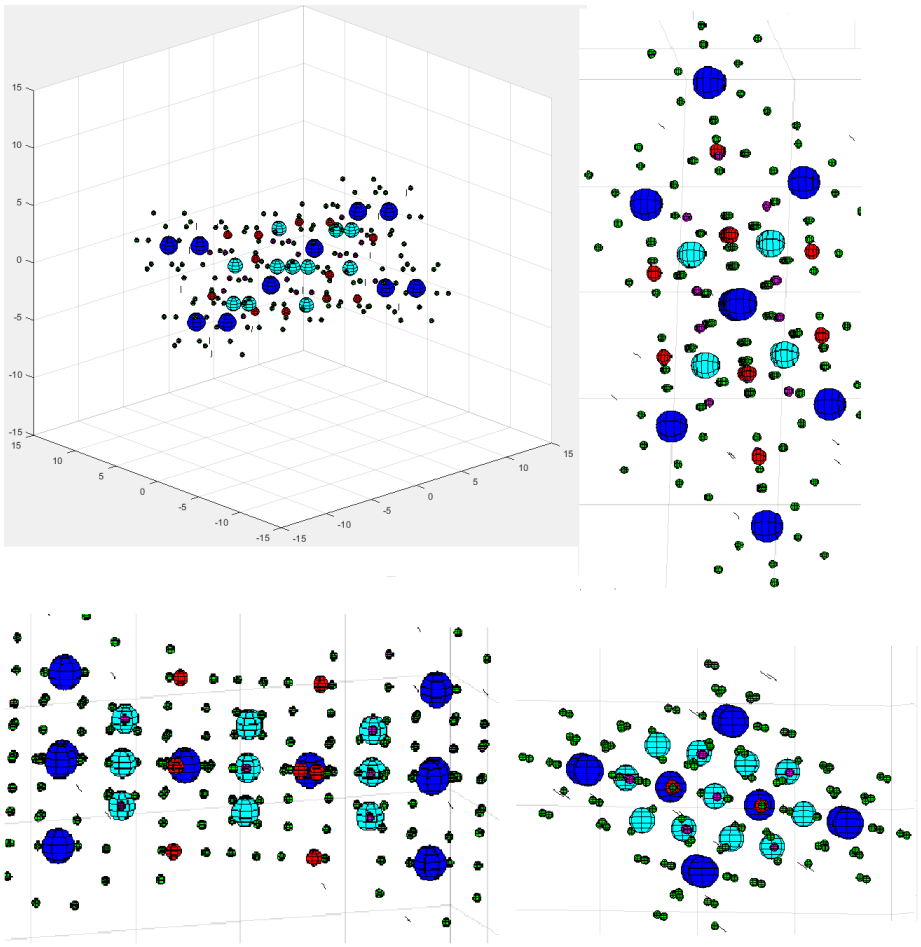

Figure 24: Natrojarosite 3D Matlab images made using data file from the American Mineralogist Crystal Structure Database[8]. The cyan atoms are iron, the magenta atoms are hydrogen, the red atoms are sulphur, the green atoms are oxygen, and the blue atoms are sodium.

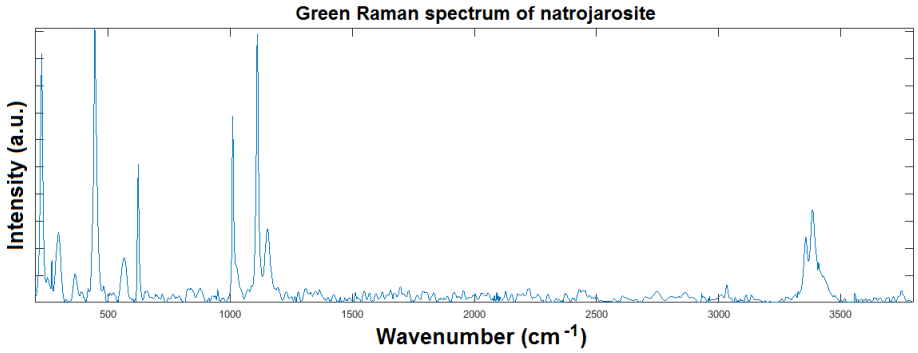


Figure 25: Raman spectrum of natrojarosite at 532 nm excitation with a commercial Raman microscope.

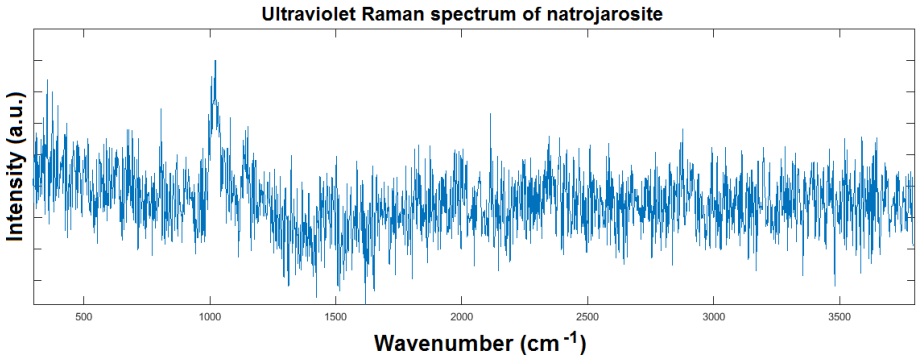


Figure 26: Raman spectrum of natrojarosite at 266 nm excitation with a prototype in-situ stand off Raman system.

excitation data previously presented for gypsum. This is because the overall intensity from the gypsum is more than two orders of magnitude higher and therefore it has a greater signal-to-noise ratio.

Next, we present the spectral data from the prototype in-situ stand-off Raman system at 266 nm excitation (figure 26).

No discernible information is available from this spectrum other than a weak sulphate symmetric stretch around 1022 $cm^{-1}$ and a weaker sulphate antisymmetric stretch around 1150 $cm^{-1}$, the latter of which is barely more significant that the surrounding noise. Note the small peak around ~2340 $cm^{-1}$ and the even smaller peak ~1500 $cm^{-1}$. These result from molecular nitrogen and oxygen, respectively. Wu et al[75] reported these peaks at 2331 $cm^{-1}$ and 1551 $cm^{-1}$. We don't see these in the gypsum spectrum because the gypsum sulphate stretching Raman peaks are three orders of magnitude greater intensity than the natrojarosite peaks with UV excitation.

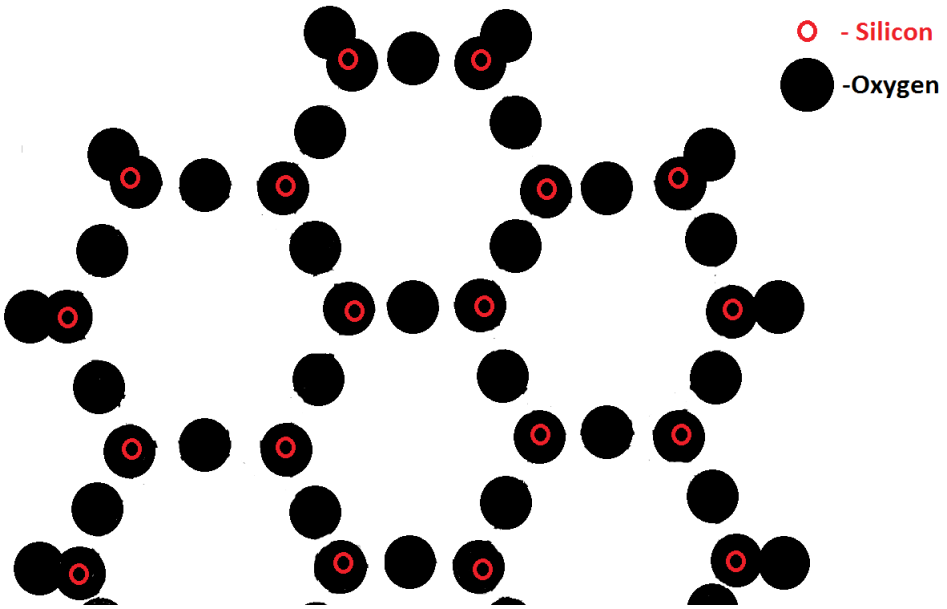


Figure 27: Hexagonal network of linked $SiO_4$ tetrahedra comprising the T sheet in phyllosilicates.

## 6.3 Phyllosilicates

Phyllosilicates are sheet silicate materials and often referred to as clays. The sheet silicate structure comes from two sheet types known as tetrahedral (T) or octahedral (O).

The T sheets are made of $Si^{4+}$ (sometimes $Al^{3+}$) cations attached to $O^{2-}$ anions. The anions lie in two planes with the cations in tetrahedral sites in between the planes. The structure of phyllosilicate T sheets contains two dimensional networks of hexagonal rings connected at tetrahedra. Figure 27 shows a two dimensional top down view of a T sheet.

The O sheets are made up of $Mg^{2+}$, $Fe^{2+}$, $Al^{3+}$, or $Fe^{3+}$ cations attached to $OH^-$ anions. Whether the cations are divalent ($Fe^{2+}$, $Mg^{2+}$) or trivalent ($Fe^{3+}$, $Al^{3+}$) decides whether the octahedral sheet is classed as trioctahedral or dioctahedral, respectively. The O sheets, most commonly gibbsite $Al(OH)_3$, are arranged such that the oxygens of aluminum-centred octahedra are bonded to either hydrogen, thereby forming hydroxyls, or an oxygen at a vertex of a $SiO_4$ tetrahedron from the adjacent T sheet [76]. The O layer is more complex than the T layer and would be difficult to visualize with a two dimensional image.

In T-O phyllosilicates, layers are bonded from the outward hydrogen of a hydroxyl in an octahedral complex (O sheet) to the oxygens in the tetrahedral complex of a tetrahedral sheet in the adjacent layer. In T-O-T sheets, layers are weakly bonded to adjacent layers through electrostatic bonds. Interlayer cations

| Vibration | Raman shift ($cm^{-1}$) | Relative intensity |
|---|---|---|
| Inner surface O-H stretch | 3600-3700 | weak |
| Inner O-H stretch | 3600-3650 | weak |
| Inner surface O-H deformation | 900-950 | weak |
| O-H translation | 740-790 | medium |
| O-Si-O | ~700 | medium |
| $SiO_4$ symmetric stretch | 400-550 | medium |
| $SiO_4$ symmetric stretch | ~335 | medium |
| Al-OH stretch | ~250-270 | medium |
| Al-$(O/OH)_6$ symmetric stretch | ~200 | weak |
| Al-$(O/OH)_6$ symmetric stretch | 140-150 | strong |

Table 7: Typical spectral regions for vibrations in phyllosilicates.

$K^+$, $Na^+$, $Li^+$, or $Ca^{2+}$, as well as interlayer water can also bond adjacent layers to one another.

Which type of sheets are involved in a clay as well as which cations are involved generally specifies which type of clay a mineral is. The general formula for phyllosilicates is $XYAlSi_3O_{10}(OH)_2$. In this formula, the X can be the interlayer cations $K^+$, $Na^+$, $Li^+$, or $Ca^{2+}$, while the Y represents the possible structural substitution cations described earlier.

Sometimes the words phyllosilicate and clay get used interchangeably. We will do so here, but note that the term phyllosilicate usually designates a type of a mineral in the theoretical form, whereas a clay can be an assortment of minerals dominated by a phyllosilicate, such as with mudstone. Usually, a clay is a disordered phyllosilicate of small grain size. Where a theoretical phyllosilicate should extend to infinity in two dimensions, obviously in real world samples it does not. Where there is a broken edge can lead to a charge buildup where other molecules may bond.

Clays often form from the chemical breakdown of aluminum rich silicate minerals in aqueous environments. Formation of individual clay types will be discussed in the next subsections.

Orbiting spacecraft and rovers have determined that the clays nontronite, montmorillonite and kaolinite are present on the surface of Mars [28][30]. Since clays must be formed through aqueous alteration, their presence confirms the past existence of liquid water. Some clays require formation in warm water, providing evidence of nearby hydrothermal activity.

Table 7 lists regions where one could expect to observe Raman bands from phyllosilicates.

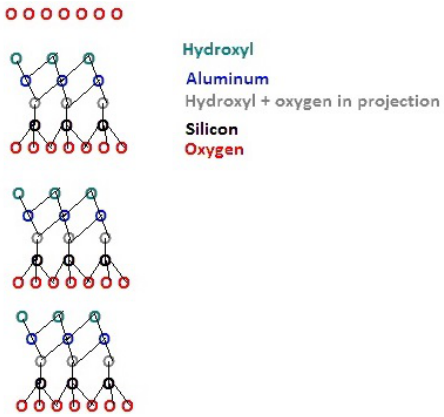


Figure 28: T-O layered structure of kaolinite

### 6.3.1 Kaolinite

**Kaolinte - $Al_2Si_2O_5(OH)_4$**

Kaolinite, a T-O sheet silicate, forms from hydrolysis of potassium feldspar. Carbon dioxide gas dissolves in water making carbonic acid ($H_2CO_3$), which becomes $H^+$ and bicarbonate ions ($HCO_3^-$). This makes the water acidic. The acidic water reacts with the feldspar, breaking bonds and dissolving the potassium ion and silica. Recrystallization forms the clay, while the ions and some of the silica are left in solution. [77].

$$2KAlSi_3O_8 + 2H^+ + H_2O \rightarrow 2K^+ + 4SiO + Al_2Si_2O_5(OH)_4$$

Higher temperatures favour this reaction. Therefore, kaolinite is more likely to be found in intertropical zones. Organic acids provided by bacterial activity can speed up the process[77].

Kaolinite is empty between the layers (non-expanding). The layers are held too closely together to allow interlayer ions or molecules to enter. This means there is no interlayer swelling from water. Kaolinite can however, adsorb large amounts of water to the outer surfaces of the crystal. The layered structure of kaolinite is shown in Figure 28. The hydroxyl located in an unshared plane is called the outer hydroxyl, while that which shares a plane with oxygen atoms is called the inner hydroxyl. Due to their differing environments, they will have slightly different bond force constants and therefore will stretch at different frequencies.

Next, we present the data for two kaolinites from both the green and UV Raman systems. The green spectra are presented with and without correction for fluorescence background. There was little or no fluorescence at UV excitation for most of the minerals and therefore fluorescence background corrected data is only selectively presented for those data sets.

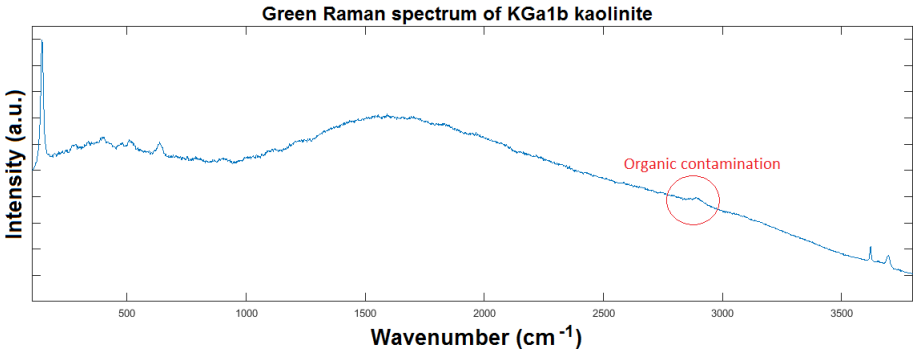


Figure 29: Raman spectrum of kaolinte KGa1b at 532 nm excitation with a commercial Raman microscope.

We note here that fluorescence removal attempts to eliminate the fluorescence background curve, but does nothing to eliminate the noise associated with this fluorescence. Therefore, when the fluorescence is removed the resulting Raman spectra are not necessarily easier to interpret. In fact, sometimes the process introduces more problems than it helps. At the current moment it does not appear to be a standardized industry requirement to present Raman spectra with the fluorescence baseline removed.

Noise due to dark current and ambient light was removed for the UV system by the process mentioned in section 4.3.2. A noise background correction was not performed using the green system. However, the green system is housed in a closed compartment, thus the sample would not be exposed to ambient light and would only be affected by detector dark current and shot noise. Cosmic ray removal was applied to data from both systems.

In the plots that follow, organic contamination and atmospheric nitrogen are circled in red on all the pre-background correction spectra.

The plots for the two kaolinites at green excitation in Figure 29 and Figure 32 show a high similarity. They both have the strong O-Al-O deformation at 143 $cm^{-1}$, and the two hydroxyl stretches at 3622 $cm^{-1}$ and 3697 $cm^{-1}$ line up perfectly on both samples. The lower energy of the two hydroxyl vibrations is due the inner hydroxyl, while the higher energy vibration corresponds to the outer hydroxyl [78]. The next strongest band is at 637 $cm^{-1}$ and is found in both samples, but more easily seen in the KGa1b sample. Small peaks at 393 $cm^{-1}$ and 510 $cm^{-1}$ are visible in the KGa1b sample, but in the KGa2 sample the same peaks are on the same order as the noise, so it would be difficult to definitively say that they have been observed. The peak at 393 $cm^{-1}$ is attributed to a O-Si-O stretch.

Frost et al [48] attributed the poor spectra to the small size of the clay. They noted that Raman spectra are dependent on the long range order of the crystals, thus explaining why the kaolinite produces a poor signal. This also explains why the more disordered sample produces the weaker of the two signals.

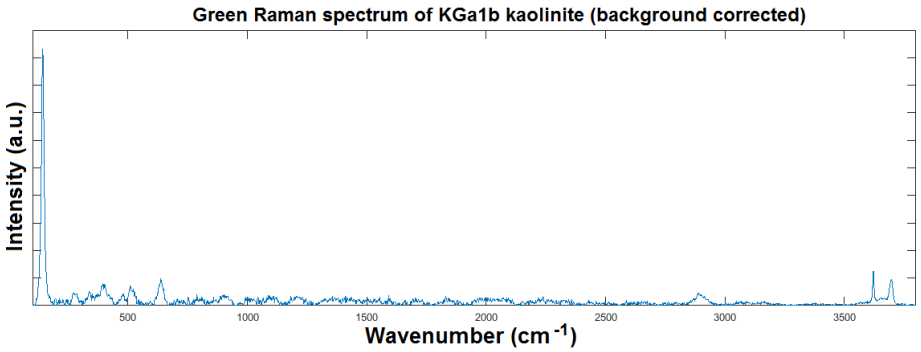


Figure 30: Raman spectrum of kaolinte KGa1b at 532 nm excitation with a commercial Raman microscope, corrected for fluorescence.

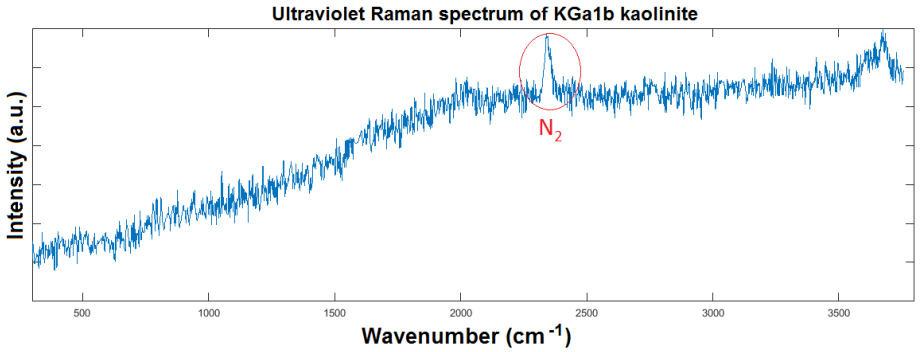


Figure 31: Raman spectrum of kaolinite KGa1b at 266 nm excitation with a prototype in-situ stand off Raman system.

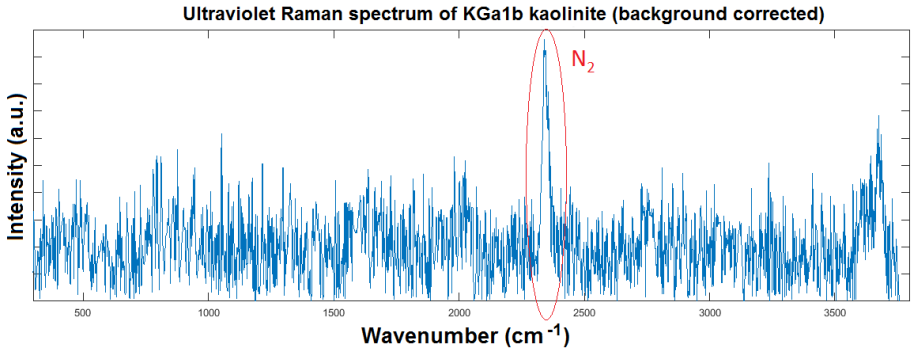


Figure 32: Raman spectrum of kaolinite KGa1b at 266 nm excitation with a prototype in-situ stand off Raman system, corrected for fluorescence.

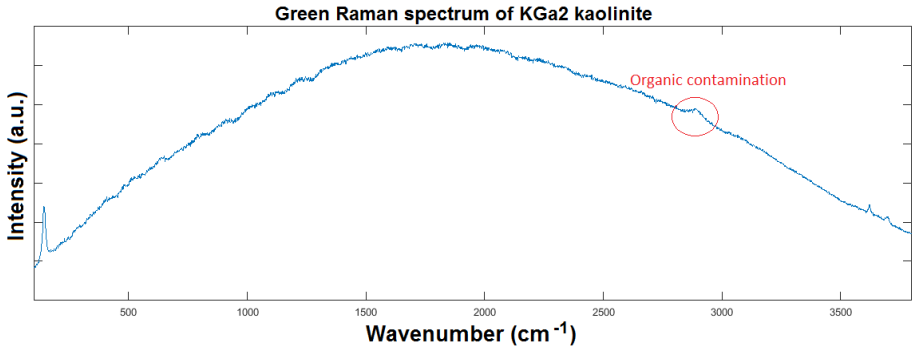


Figure 33: Raman spectrum of kaolinte KGa2 at 532 nm excitation with a commercial Raman microscope.

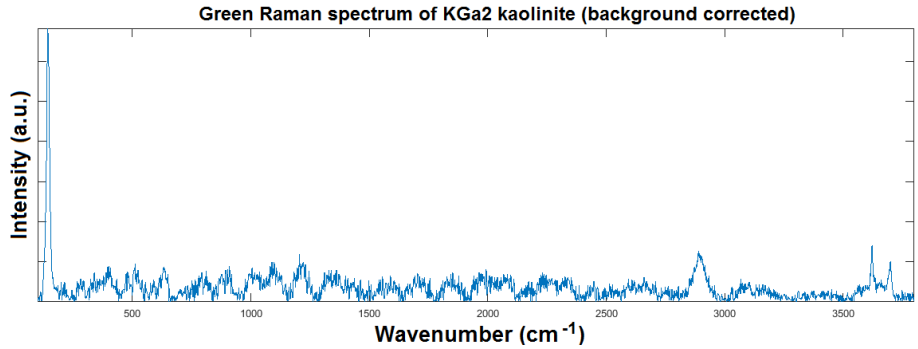


Figure 34: Raman spectrum of kaolinte KGa2 at 532 nm excitation with a commercial Raman microscope, corrected for fluorescence.

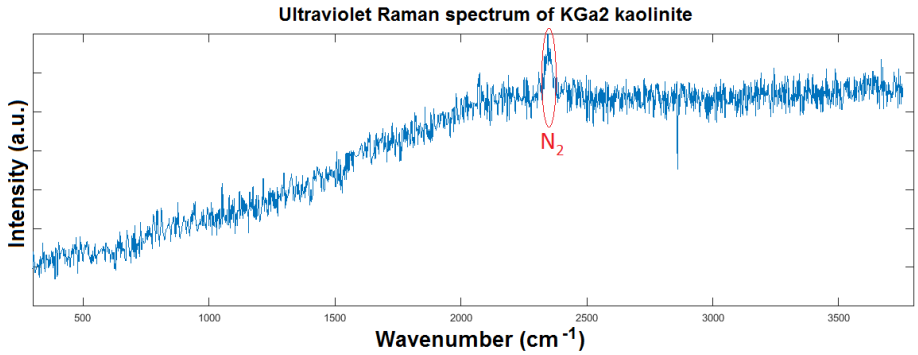


Figure 35: Raman spectrum of kaolinite KGa2 at 266 nm excitation with a prototype in-situ stand off Raman system.

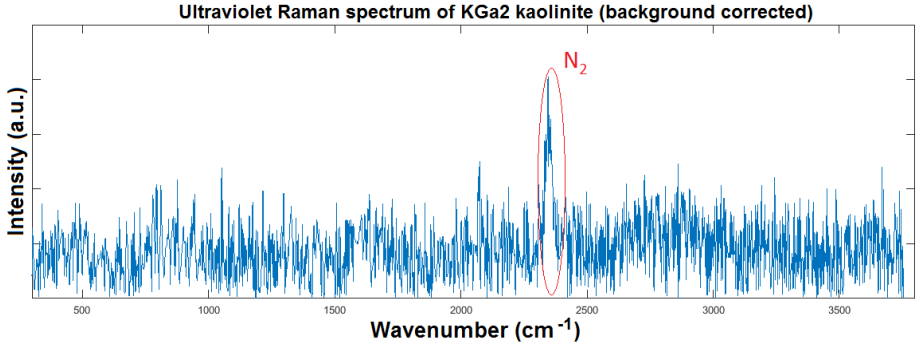


Figure 36: Raman spectrum of kaolinite KGa2 at 266 nm excitation with a prototype in-situ stand off Raman system, corrected for fluorescence.

Frost [79] observed all of these bands, but also observed a band at 915 $cm^{-1}$ which he attributed to an inner hydroxyl deformation . They did not mention the source of the 510 $cm^{-1}$ and 637 $cm^{-1}$ peaks, but at least the lower of the two is likely a stretch of the silicon-centered tetrahedra as well. In a later paper, Frost et al [48] attributed a band at 512 $cm^{-1}$to an out-of-plane $SiO_4$ deformation. There is a small amount of titanium structurally replacing the aluminum in the O sheet, and a strong band has been reported because of O-Ti-O vibrations in the 600-700 $cm^{-1}$region for minerals. It isn't clear whether the small titanium content would be enough to produce this peak.

With green excitation we observed a weak broad band around 2900 $cm^{-1}$ indicating that both samples start with a minor amount of organics contamination.

It was mentioned in chapter 4 that one sample was less disordered than the other. The KGa1b sample that has clearer Raman peaks in the region below 800 $cm^{-1}$ is the less disordered sample. X-ray diffraction measurements of the two kaolinite samples done at the Royal Ontario Museum confirmed this difference.

With the UV system there is enough noise and poorer resolution that for the KGa1b plots in Figure 31 and Figure 32 the lower energy of the hydroxyl stretches appears more like a shoulder. The only other band observed in the UV is the molecular nitrogen in the room ~2350 $cm^{-1}$.

One would not be able to use the UV Raman data obtained to definitively say that this sample was kaolinte. Minor titanium replacement of the aluminum in our samples is likely the cause of this poor result. UV absorptions by titanium complexes and complexes involving other transition metals such as iron are discussed in chapter 7.

### 6.3.2 Smectites

**Montmorillonite - $Al_2Si_4O_{10}(OH)_2$-n($H_20$)**

**Nontronite - $(Al,Fe)_2Si_4O_{10}(OH)_2$-n($H_20$)**

Smectites (T-O-T sheet silicates), are a subgroup of clays which includes both montmorillonites and nontronites. Structurally, they are the same, but chemically they are different. The chemical differences are substitutions of the central cation in the tetrahedral and octahedral groups, with octahedra cation substitutions being the most common. Nontronite is the iron dominant end member of these substitutions, while montmorillonite has the lowest iron content of the smectites. Even the iron end member never has complete replacement of the aluminum in the octahedral layer. The formulas listed in the title of this subsection are the theoretical values for end members with no interlayer species, but the actual constituents of our samples are listed in the appendices.

Smectites form from weathering of basaltic volcanic ashes in neutral to alkaline aqueous solution and subsequent recrystallization[31]. On Earth, nontronite has been found at the bottom of the ocean at white smoker chimneys as a precipitate of hydrothermal fluids[27]. Nontronite is generally suggested to be the primary metal silicate found in hydrothermal sediments[77]. Kohler et al [27] suggest that the delicate folded clay sheet microstructure of nontronite deposits at smoker chimneys indicates that sheath forming bacteria, which are Fe oxidizing, are playing a role in their formation.

Smectites can have interlayer cations, hydrated cations, and interlayer water. If enough water moves into the interlayer region the layer spacing can expand dramatically from sub-nanometer spacing to multiple nanometers. In addition to interlayer water, smectites can also adsorb significant water to their outer surfaces. The weak interlayer bonding and interlayer water allow for smectite layers to slide over one another. The layered structure of a smectite is shown in Figure 37. Nguyen and Baird [80] note that most montmorillonite platelets are approximately 1 nm thick and have lateral dimensions of 100-200 nm, which is smaller than the wavelengths of our lasers.

Next, we present the data for four montmorillonites and three nontronites from both the green and UV Raman systems. The green spectra are presented with and without correction for the fluorescence background.

With green excitation, all four montmorillonites show a single broad stretch in the O-H region at approximately 3625 $cm^{-1}$. This is mainly due to structural O-H groups. Variations in this peak intensity could be indicative of the number of water molecules per unit cell.

Similar to the kaolinites, all of the montmorillonites have suspected organic contamination identified by a C-H stretch at 2895 $cm^{-1}$. The remainder of the bands were found at 1110 $cm^{-1}$, 922 $cm^{-1}$, 711 $cm^{-1}$, 425 $cm^{-1}$, 291 $cm^{-1}$, 201 $cm^{-1}$. These bands were all well defined for the STx1b sample and poorly defined for the others. Wang et al[81] suggested that these bands should shift between montmorillonite types due to differing replacement of the central cation in the octahedral sheet. However, we observed no shift in band positions. The

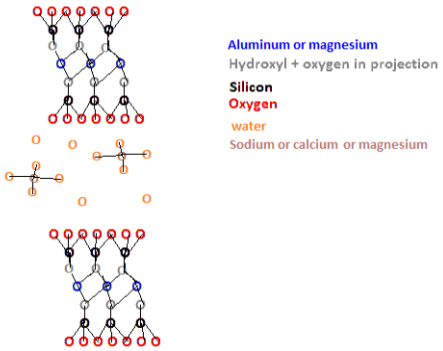


Figure 37: T-O-T layered structure of montmorillonite. Nontronite has the same structure, but with aluminum and magnesium partially replaced by iron. Smaller amounts of silicon may also be replaced with iron.

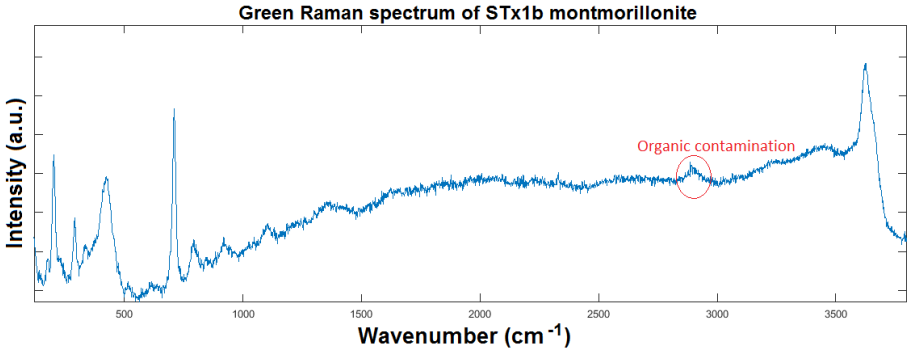


Figure 38: Raman spectrum of calcium rich montmorillonite STx1b at 532 nm excitation with a commercial Raman microscope.

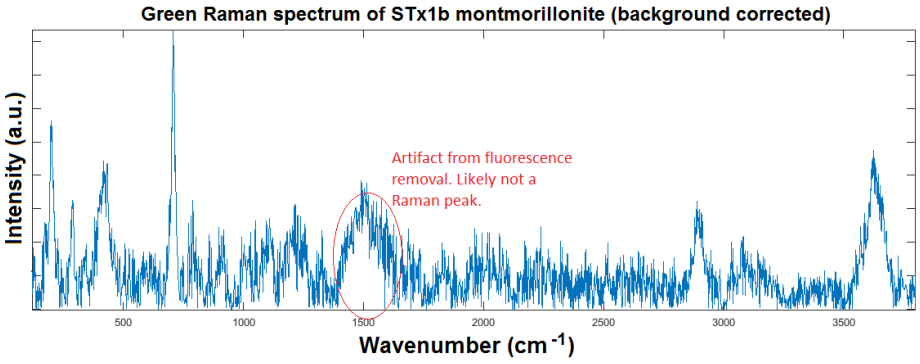


Figure 39: Raman spectrum of calcium rich montmorillonite STx1b at 532 nm excitation with a commercial Raman microscope, corrected for fluorescence.

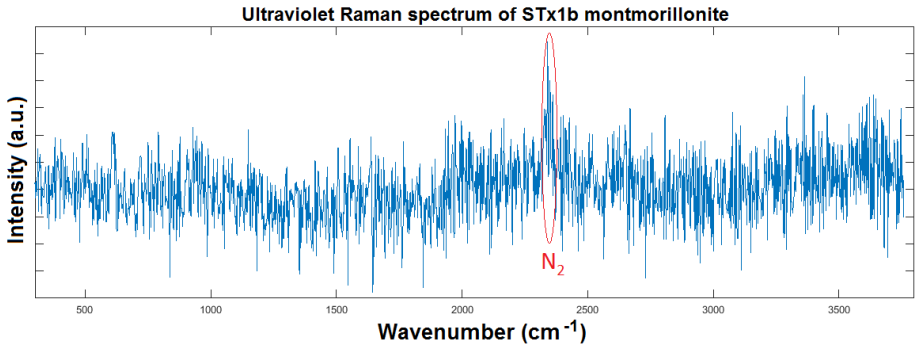


Figure 40: Raman spectrum of calcium rich montmorillonite STx1b at 266 nm excitation with a prototype in-situ stand off Raman system.

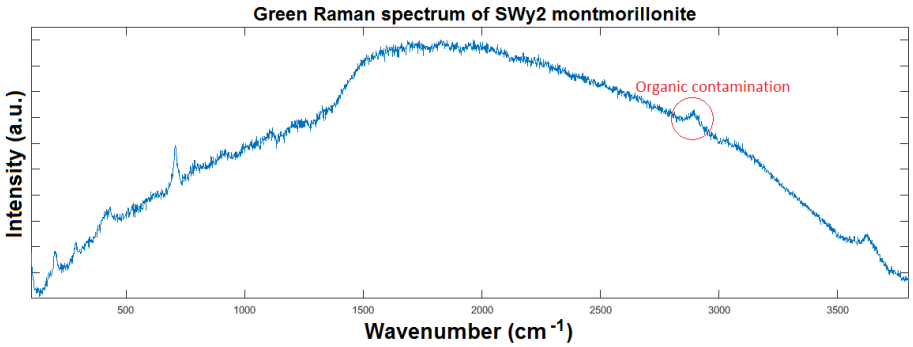


Figure 41: Raman spectrum of sodium rich montmorillonite SWy2 at 532 nm excitation with a commercial Raman microscope.

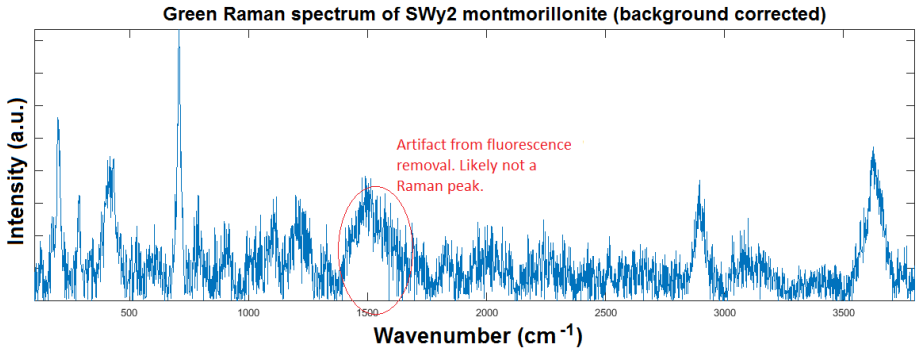


Figure 42: Raman spectrum of sodium rich montmorillonite SWy2 at 532 nm excitation with a commercial Raman microscope, corrected for fluorescence.

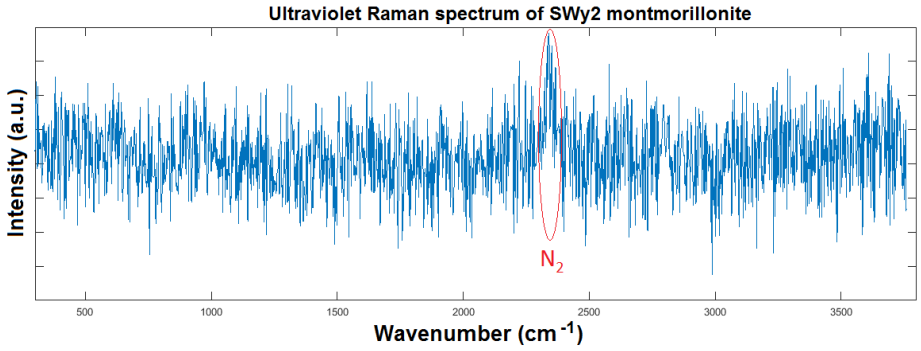


Figure 43: Raman spectrum of sodium rich montmorillonite SWy2 at 266 nm excitation with a prototype in-situ stand off Raman system.

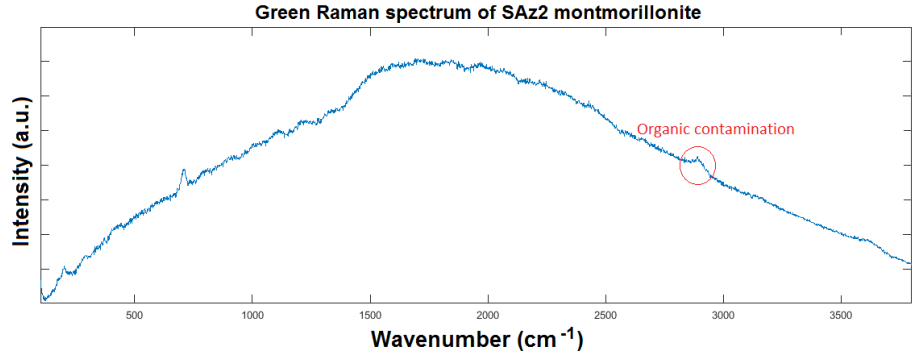


Figure 44: Raman spectrum of calcium and sodium rich montmorillonite SAz2 at 532 nm excitation with a commercial Raman microscope.

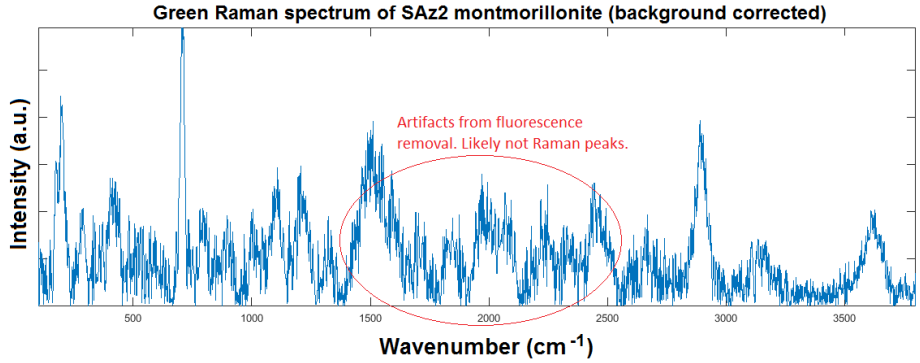


Figure 45: Raman spectrum of calcium and sodium rich montmorillonite SAz2 at 532 nm excitation with a commercial Raman microscope, corrected for fluorescence.

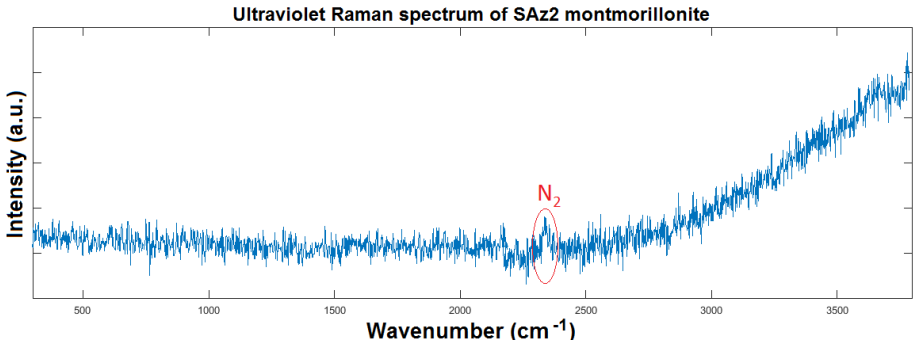


Figure 46: Raman spectrum of calcium and sodium rich montmorillonite SAz2 at 266 nm excitation with a prototype in-situ stand off Raman system.

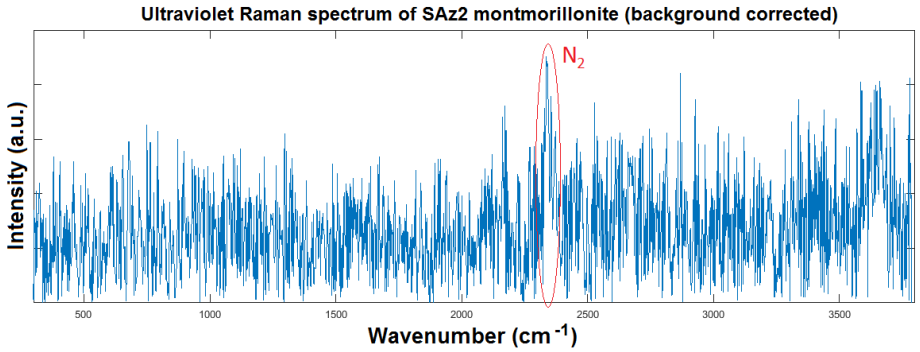


Figure 47: Raman spectrum of calcium and sodium rich montmorillonite SAz2 at 266 nm excitation with a prototype in-situ stand off Raman system, corrected for fluorescence.

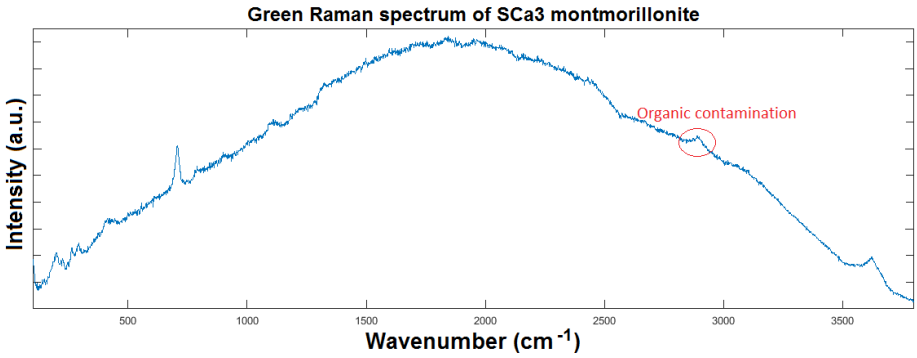


Figure 48: Raman spectrum of calcium, sodium and magnesium rich montmorillonite SCa3 at 532 nm excitation with a commercial Raman microscope.

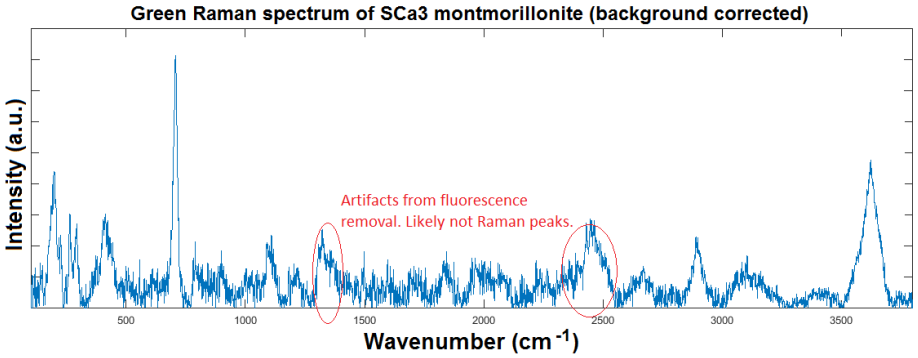


Figure 49: Raman spectrum of calcium, sodium and magnesium rich montmorillonite SCa3 at 532 nm excitation with a commercial Raman microscope, corrected for fluorescence.

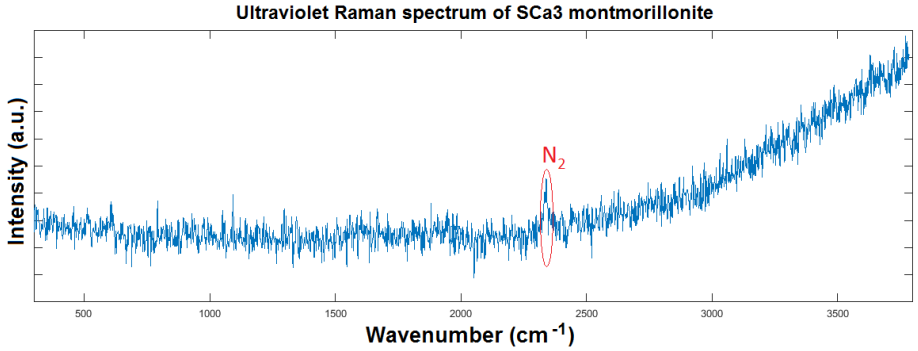


Figure 50: Raman spectrum of calcium, sodium and magnesium rich montmorillonite SCa3 at 266 nm excitation with a prototype in-situ stand off Raman system.

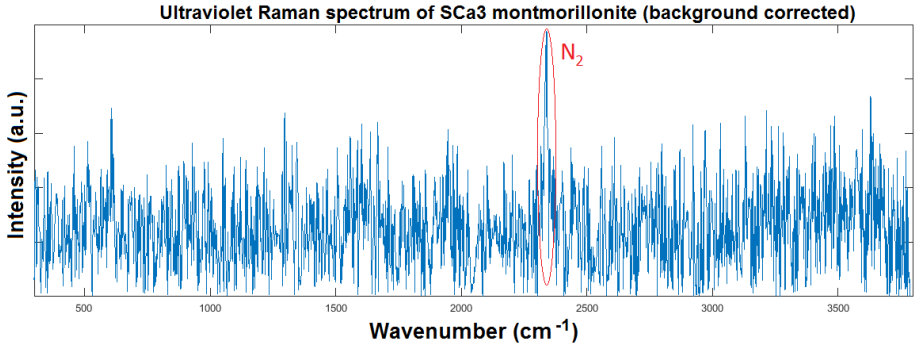


Figure 51: Raman spectrum of sodium and magnesium rich montmorillonite SCa3 at 266 nm excitation with a prototype in-situ stand off Raman system, corrected for fluorescence.

band at 1110 $cm^{-1}$ is likely due to O-Mn-O vibrations as that band had been suggested to be from O-Ti-O vibrations in kaolinite by Wang et al[81]. We assume that because manganese and titanium have similar atomic masses. The band at 922 $cm^{-1}$ is likely an inner surface hydroxyl distortion. The strong band at 711 $cm^{-1}$ was suggested by Rinaudo et al [82] to be a symmetric stretch of the $SiO_4$ tetrahedra, while that at 425 $cm^{-1}$ is also suggested to be related to the octahedra. They observed a peak at 290 $cm^{-1}$ and attributed it to a O-H-O deformations. The band at 201 $cm^{-1}$ is attributed to a stretch of the $AlO_6$ octahedra.

The STx1b sample also has an additional three bands at 175 $cm^{-1}$, 340 $cm^{-1}$ and 520 $cm^{-1}$. The lowest energy is suggested to be O-Al-O bending vibrations. The lower energy of the remaining two is likely a stretch of the $SiO_4$but it is not clear what the highest energy band is from. The SCa3 sample has a peak that is unique to that sample at 265 $cm^{-1}$. This could be an Al-OH stretch.

In addition to having different interlayer cations, the sodium montmorillonite has also been shown to have iron replacement of the aluminum in the octahedral layer[83]. This replacement would change some of the low frequency vibrational frequencies.

None of the UV data for any of the montmorillonites yielded discernible Raman bands. The sample from Arizona, SAz2, did display a band in the O-H stretching region, but that information is useless without additional bands from the mineral. Also, the band observed is so noisy and broad that it is difficult to determine the precise Raman shift. Minor iron replacement of the aluminum in our samples is likely the cause of this poor result. UV absorptions by iron complexes and complexes involving other transition metals are discussed in chapter 7.

The three nontronite samples produce similar Raman spectra with green excitation, but the shape of the background fluorescence varies significantly between the Australian (NAu1, NAu2) and German (NG1) samples.

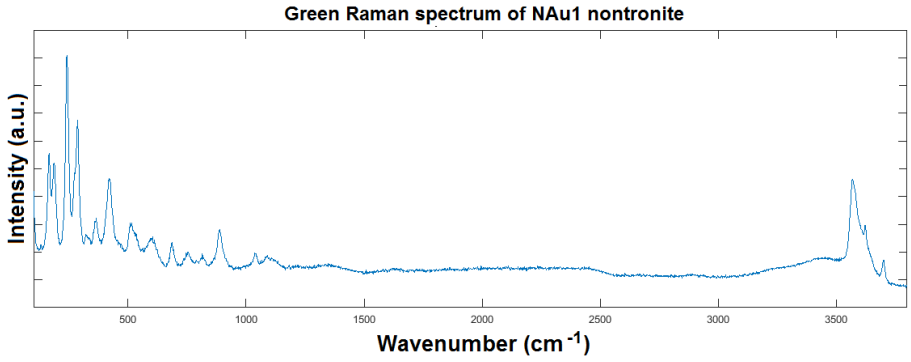


Figure 52: Raman spectrum of nontronite NAu1 at 532 nm excitation with a commercial Raman microscope.

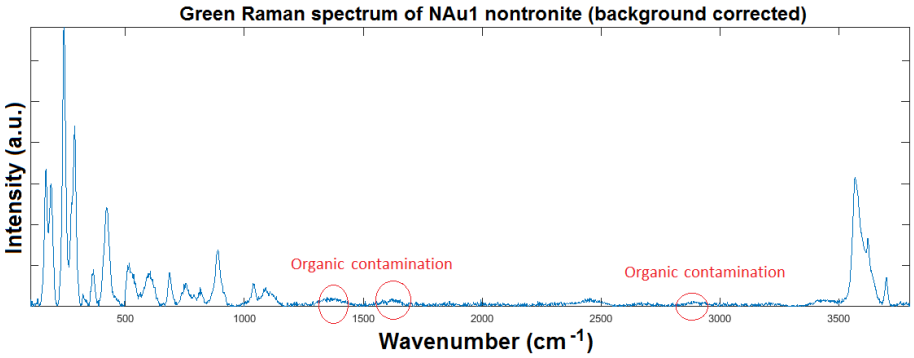


Figure 53: Raman spectrum of nontronite NAu1 at 532 nm excitation with a commercial Raman microscope, corrected for fluorescence.

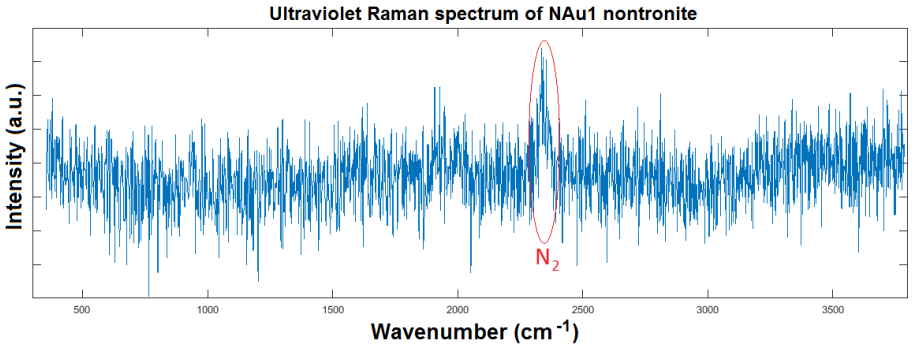


Figure 54: Raman spectrum of nontronite NAu1 at 266 nm excitation with a prototype in-situ stand off Raman system.

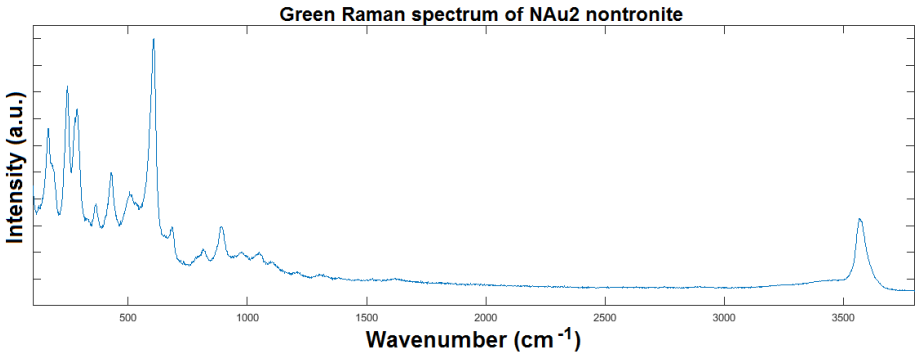


Figure 55: Raman spectrum of nontronite NAu2 at 532 nm excitation with a commercial Raman microscope.

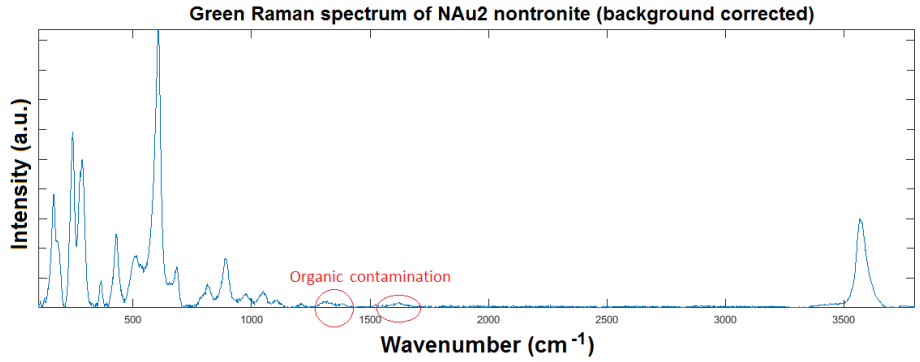


Figure 56: Raman spectrum of nontronite NAu2 at 532 nm excitation with a commercial Raman microscope, corrected for fluorescence.

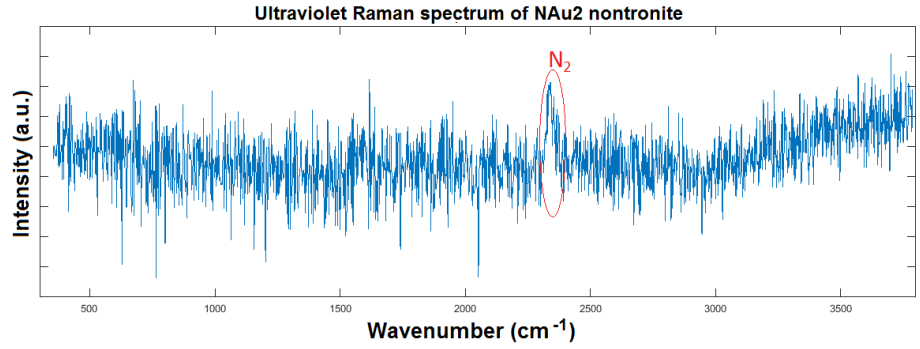


Figure 57: Raman spectrum of nontronite NAu2 at 266 nm excitation with a prototype in-situ stand off Raman system.

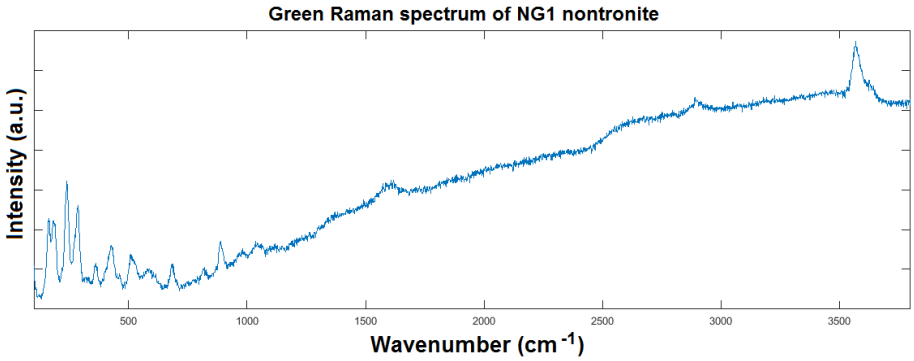


Figure 58: Raman spectrum of nontronite NG1 at 532 nm excitation with a commercial Raman microscope.

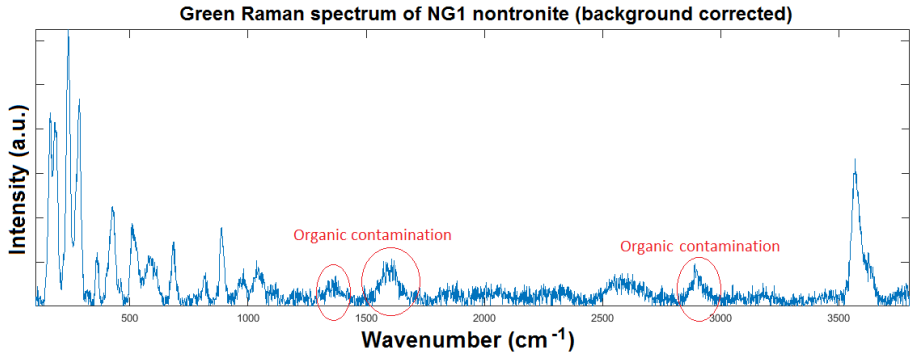


Figure 59: Raman spectrum of nontronite NG1 at 532 nm excitation with a commercial Raman microscope, corrected for fluorescence.

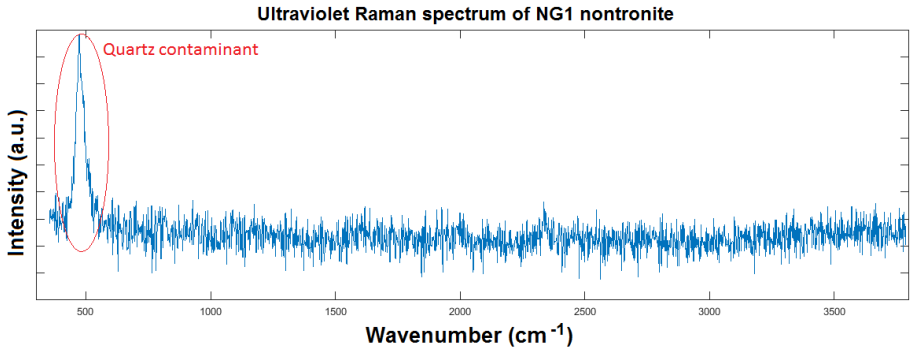


Figure 60: Raman spectrum of nontronite NG1 at 266 nm excitation with a prototype in-situ stand off Raman system.

All three samples have an O-H stretch at 3571 $cm^{-1}$, but it is interesting to note that only the NAu1 sample has an additional two O-H stretches at 3623 $cm^{-1}$ and 3700 $cm^{-1}$.

Only the NG1 and NAu1 samples appear to have the organic contaminant of an aliphatic C-H stretch found in the previously presented clays at 2894 $cm^{-1}$. All three nontronites show bands around 1350 $cm^{-1}$ and 1610 $cm^{-1}$. These are also indicative of organics as a C=C double bond. In the literature, they are referred to as the disordered 'D band' and ordered 'G band', respectively[84]. Eshelman[5] mentioned how no minerals have vibrational frequencies in that region, thus observing a peak there is a good indicator of organic content.

Some carbon deposits can exhibit a peak in the 2450-2800 $cm^{-1}$ range called a '2D(G*)-band'. We do observe a band in our background corrected spectra there for NAu1 and NG1 (as well as some of the montmorillonite samples), but we believe that in our experiment this is an artifact of a sharply changing fluorescence background being removed and not actually a band from organics contamination.

There are at least 10 observable peaks in the mineral fingerprinting region below 1000 $cm^{-1}$. The German NG1 sample has slightly more noise and weaker peaks than the Australian samples. However, it appears to have the same number of peaks. It is likely that the differences between the colour of the samples is whether the iron is ferric or ferrous as colour in iron bearing minerals can be a function of the oxidation state[83]. We observe two low frequency lattice vibrations at 164 and 188 $cm^{-1}$, though the second of these two is very weak from the NAu2 sample. These bands are attributed to O-Al-O lattice interactions. Frost and Kloprogge [85] published data with peaks at 239 $cm^{-1}$, 287 $cm^{-1}$, and 363 $cm^{-1}$ attributed to O-Si-O bending. This matched our data within a few wavenumbers. We also observed bands at 432 $cm^{-1}$ 512 $cm^{-1}$ 606 $cm^{-1}$ 686 $cm^{-1}$ 815 $cm^{-1}$. The last of these was very weak in all samples and not mentioned in published data. The 606 $cm^{-1}$ band was much larger for the NAu2 sample than the others. A hydroxyl deformation at 879 $cm^{-1}$ in their results is at a slightly lower wavenumber than the peak common in that region for all three of our samples at 890 $cm^{-1}$. The intense band at 474 $cm^{-1}$ in the UV Raman spectrum is due to quartz contamination in the sample and should be ignored.

A possibility for these lower energy vibrations is O-Fe-O modes. If they are due to iron, it is interesting that the low frequency bands would match up so closely because band position should be a function of oxidation state (higher oxidation state, higher energy vibration). The three nontronite samples are varied in colour which implies that their $Fe^{2+}/Fe^{3+}$ ratios differ, yet the Raman data doesn't confirm this. Therefore, the other unidentified lower energy bands may be alternatively caused by various silicate stretches having different energies depending how closely in the crystal the $SiO_4$ tetrahedra are positioned with respect to locations with iron substitutions

The presented data here was checked using a spectral matching software at the Royal Ontario Museum. It identified all three samples as a nontronite match. However, since the museum's Raman microscope has such a small spot

size and these samples have a lot of quartz contamination, sometimes it took more than one acquisition to obtain a nontronite spectrum instead of a quartz spectrum.

None of the UV data for any of the nontronites yielded any discernible Raman bands from the minerals. Only the molecular nitrogen and oxygen were observed. Major iron replacement of the aluminum in our samples is likely the cause of this poor result. UV absorptions by iron complexes and complexes involving other transition metals are discussed in chapter 7.

### 6.3.3 Imperfections in the crystal lattice of clays

Cations in either the octahedral or tetrahedral units can be replaced without any significant change in the crystal structure. Aluminum can replace the silicon (T sheet) and magnesium or iron can replace the aluminum (O sheet). Sometimes this leads to unbalanced charges. Similarly, a two dimensional sheet with no replacement cations is only charge balanced if it continues on for infinity. The broken edge of a sheet will most likely have some charge. Unbalanced charges are sometimes neutralized by interlayer cations, but can also be the source of the forces that hold an organic to a sheet.

### 6.3.4 Clays and the current organics budget

The high surface areas of clay results in a high carbon content due to absorption processes which are not well understood[15]. Des Marais[86] suggests that approximately 68% of the Earth's organic material is stored in clays and shales. Therefore, the search for Martian organics should focus on clay deposits.

### 6.3.5 Problems with clay optical spectroscopy other than UV absorption

Since these clay minerals occur in particle sizes smaller than two microns [68], incident light used for Raman scattering is approximately on the order of the particle sizes. This poses a challenge and multiple studies suggest that Raman spectroscopy of clay powders is not easy or not possible.

> *"Raman spectroscopy to sheet silicates is very much dependent on the long range order of the mineral. If the long range order is absent or the order is randomized as with layer spacings then the FT Raman spectra are difficult to obtain." [83]*
>
> *"Raman technique for the study of ferruginous smectites was difficult because the clay is a poor scatterer." [85]*
>
> *"...the use of a dispersive Raman technique results in no utilizable spectra" [49]*
>
> *"...the diffuse scattering of the primary beam at the particle surfaces in muscovite powder results in an increasing background over the entire spectral range" [49]*

*"...common Raman sampling techniques are not successful for the measurement of powdered micas"[49]*

*"...the dominant particle morphology of the Galapagos Rift and Mariana Trough clays is one of fine slightly folded sheets, less than 1 micron in diameter" [27]*

*"...it is almost impossible to distinguish individual species or even broad groups of clays from each other based on optical means, even if individual grains were large enough to examine with the microscope. It is strongly recommended that the petrographer use the term clay for all members of the group and employ X-ray diffraction or other techniques to identify the various species." [68]*

# 7 Transition metal bearing coordination complexes and UV absorption

## 7.1 What is the problem that we are concerned with?

Besides scattering, another way that light interacts with matter is absorption. When the wavelength of a laser beam incident on a sample corresponds with a band in the absorption spectrum of that sample, a photon may be absorbed. The result is that the molecule or crystal is excited to an electronic or vibrational excited state. Which excited state it enters depends on the wavelength of the incident light, with electronic states favouring UV and VIS excitation and vibrational states favouring IR excitation. The absorbed energy may then be converted to heat and transferred to the environment via a radiationless transition. It is important to note that Raman scattered light can also be absorbed from an adjacent molecule or crystal in a sample if the Raman shifted light corresponds to an absorption band.

UV reflectance/absorption spectroscopy of transition metal-bearing minerals produces intense and broad absorption bands. This absorption is due to electronic transitions in the coordination complexes of the minerals. Since Raman spectroscopy is a weak phenomenon, coupling that weakness with strong UV absorption means that UV Raman spectroscopy of transition-metal bearing minerals is difficult with current available technology. This chapter will highlight the reasons for these strong electronic absorption peaks. It will also discuss why the peaks occur in the UV region and the causes for their broadness. This chapter intends to provide physical reasons for the very poor UV Raman spectra presented in the previous chapter for all the phyllosilicates and the iron bearing sulphate, natrojarosite.

The following plots were created using UV spectral reflectance data sets of aqueous alteration minerals taken at the Planetary Spectrophotometry Facility (University of Winnipeg) and provided courtesy of Ed Cloutis and Matt Izawa[9]. The first example in Figure 61 is the high iron content clay mineral nontronite. The spectrum is opaque throughout the whole region observed.

The next example, montmorillonite (Figure 62), contains some structural iron and has hematite impurities ($Fe_2O_3$), as well as trace amounts of other transition metals such as Cr, Zr and V. This is known from the x-ray fluorescence analysis done by the Planetary Spectrophotometry Facility [9]. Kaolinite (Figure 63) contains no structural transition metals in the ideal formula for the mineral. However, both samples examined in our Raman study contain trace structural titanium. Also, the natural kaolinite sample observed via UV reflectance spectroscopy contains trace transition metal impurities in similar quantities to the montmorillonite sample. Though the montmorillonite spectra show quite a smooth line in the lower energy UV region, McCormick et al.[87] observed distinct bands at 370 and 395 nm. However, they did not mention which type of montmorillonite they examined. The kaolinite is not as intense an absorber as the nontronite or montmorillonite are at 266 nm, but it is still

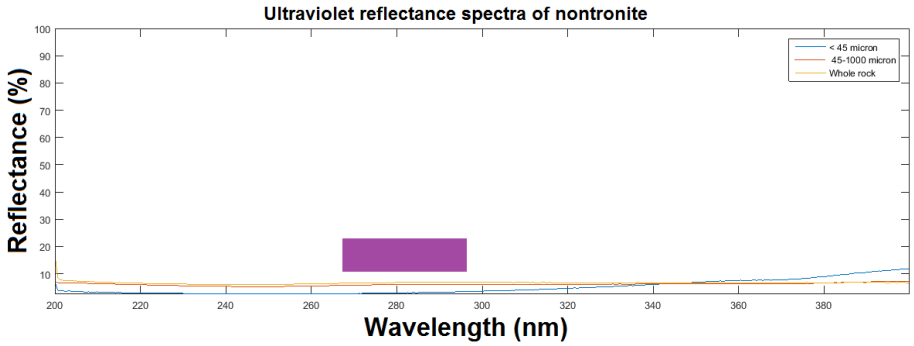


Figure 61: UV reflectance spectra of nontronite at various grain sizes taken at the University of Winnipeg[9]. Purple box denotes our UV Raman window.

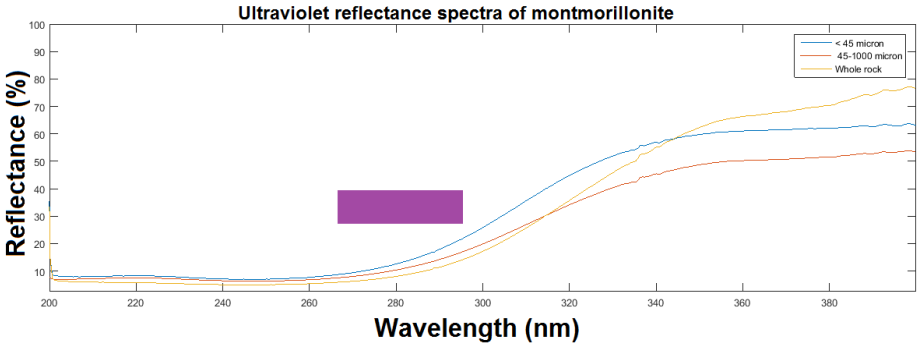


Figure 62: UV reflectance spectra of montmorillonite at various grain sizes taken at the University of Winnipeg[9]. Purple box denotes our UV Raman window.

significant and appears to have an absorption maximum around 260 nm. In addition, the upward slope towards the visible region is shallower than that of montmorillonite and occurs at longer wavelengths.

Cloutis et al [88] suggested that trace iron at 0.01 wt % concentrations can eliminate the spectrum of a mineral in the UV region. Keeping this in mind, it is important to note that Allen et al [89] used XRF to determine the chemical composition of JSC Mars-1, showing it contained 12.4 wt % $Fe_2O_3$. It is unclear if the reflectance of kaolinite at 266 nm is low enough to be the main reason for poor UV Raman results with that mineral.

To compare against a sample that is almost transition metal free, the UV reflection spectra of gypsum is presented next. Structurally gypsum contains no transition metals, and this sample presented in Figure 64 contained less than a third of the $Fe_2O_3$ impurities that the montmorillonite or kaolinite presented above contained. Again, this was determined through x-ray fluorescence measurements [9]. It is interesting to note that the gypsum reflectance spectra

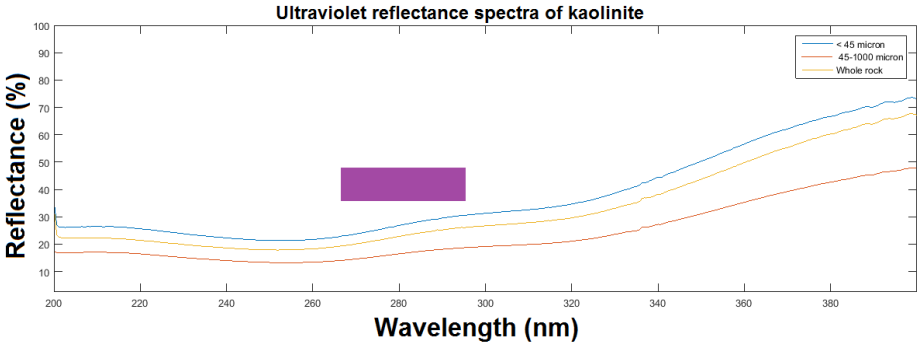


Figure 63: UV reflectance spectra of kaolinite at various grain sizes taken at the University of Winnipeg[9]. Purple box denotes our UV Raman window.

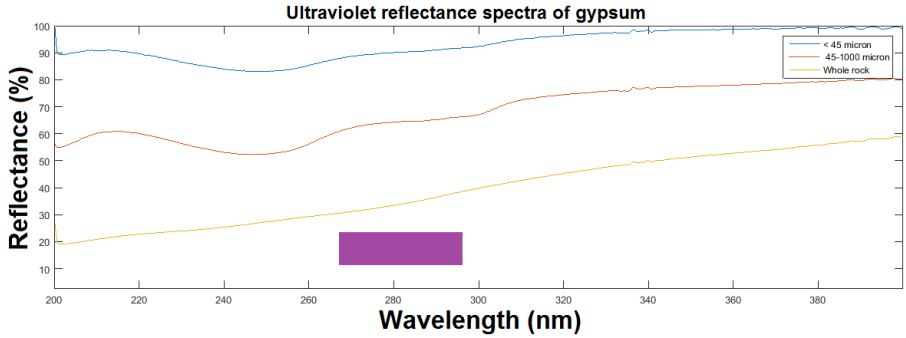


Figure 64: UV reflectance spectra of gypsum at various grain sizes taken at the University of Winnipeg[9]. Purple box denotes our UV Raman window.

presented in Figure 64 are significantly more dependent on grain size than the spectra of any of the clays

## 7.2 Transition metals

IUPAC defines a transition metal as "an element whose atom has a partially filled d sub-shell, or which can give rise to cations with an incomplete sub-shell." This is not an accepted definition across all fields as elements with a completely filled d sub-shell, yet an incomplete f sub-shell, are generally also considered transition metals. Since those higher atomic number metals are quite rare in planetary mineralogy, we can ignore them and simply focus on those with incomplete d sub-shells. Specifically, we are concerned with those metals in the $4^{th}$ period of the periodic table which have the following electronic configuration: [Argon core] $3d^{1-10}4\ s^{1-2}$. Superscripts associated with each orbital indicate the number of electrons occupying it.

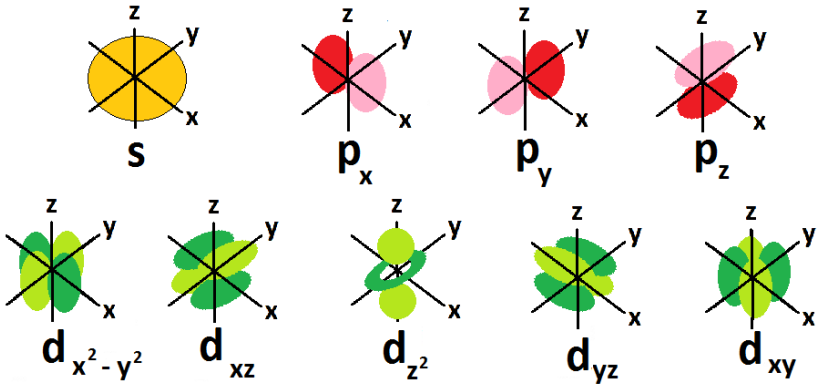


Figure 65: Illustrations of s, p, and d orbital geometries.

Fourth period transition metals include Sc, Ti, V, Cr, Mn, Fe, Co, Ni, Cu, and Zn.

## 7.3 Quantum numbers for electron orbital theories

In the above section describing the electronic configuration of transition metals, the numbers 3 and 4 refer the principal quantum number, "n", of an electron. The higher the principal quantum number, the greater the energy of the orbital and the further away from the nucleus that orbital is located. Since an electron will have higher potential energy the further it resides from the nucleus, it will be less tightly bound at higher principle quantum numbers. Once an atom is large enough to have electrons which occupy 3d and 4s orbitals, the situation becomes a more confusing as will be discussed shortly.

The azimuthal quantum number "$\ell$ " is referred to by letters, where s, p, d, and f correspond to $\ell$=0,1,2, and 3, respectively. These atomic orbitals shown in Figure 65 define the orbital angular momentum of an electron.

Each orbital will have $2\ell$ +1 sub-shells. These sub-shells are designated by a magnetic quantum number, $m_\ell$, which runs from -$\ell$ to $\ell$. In the absence of any surrounding atoms or electromagnetic fields, all the sub-shells of a particular orbital would be at the same energy. The shape of the electron cloud distribution of each orbital about the nucleus is defined by which sub-shell the electron is located within.

Each sub-shell has occupancy for two electrons. These electrons must have opposite spin angular momentum from one another. This is denoted as quantum number $m_s$ and always has a value of either +/- 1/2. In other words, any two electrons with the same n, $\ell$, and $m_\ell$, must have opposite $m_s$. This is known as the Pauli Exclusion Principle, which says that two electrons cannot simultaneously occupy the same quantum state.

For the d orbitals ( $\ell$=2) which concern our study of spectroscopy of minerals with transition metals, there are 5 sub-shells, and a therefore a total of 10 possible electrons.

## 7.4 Orbital filling

Orbitals of neutral atoms fill with the lowest n + $\ell$ value before those with higher n + $\ell$ values. That is why the 4s (4+0) orbital fills before the 3d (3+2) orbital. This can be more complicated once one considers elements which contain both 4s and 3d orbitals. For example, Cu and Cr are exceptions to this rule. For Cu, the exception is because a lower energy state results in all 3d orbitals doubly filled and the 4s orbital remaining singly occupied. This is as opposed to the spatially asymmetric orbital filling that would result from nine 3d electrons and a completely filled 4s orbital. For Cr, it is because the atom is at a lower energy if the five 3d orbitals are all singularly occupied, while the 4s orbital remains singly occupied. This is as opposed to the spatially asymmetric orbital filling that would result from only four of five 3d orbitals being singularly occupied, while the 4s orbital is completely filled .

Iron, the main transition metal that we are concerned with when studying martian geochemistry, has an atomic number of 26. Therefore, neutral atomic iron has 26 electrons and an electron configuration of [Ar] $3d^6 4s^2$. The most common oxidation states for iron are $Fe^{2+}$(ferrous) and $Fe^{3+}$(ferric). Ferrous iron or Fe(II) has electron configuration of [Ar] $3d^6$,while ferric iron or Fe(III) has electron configuration of [Ar] $3d^5$. From these oxidation state electron configurations one can see that while iron fills 4s orbitals before 3d orbitals, it is the 4s orbital electrons that are removed first. One can see in Figure 66 how close in energy the 3d and 4s orbitals are for iron. It is important to note for our study that ferric iron likely predominates in the brighter regions of Mars [76].

Another factor involved with orbital filling is called Hund's rule. It states that a greater total spin state usually results in a more stable atom. Thus, for degenerate orbitals, electrons will occupy them singly prior to filling them in pairs. The singly filled electrons will have parallel spin.

## 7.5 Coordination complexes

Coordination complexes are molecular structures which are polyhedrons formed by a central metal in coordination with surrounding ligands. A ligand is a negative ion (anion) or neutral dipolar molecule that donates at least one lone pair of electrons to form coordinate covalent bonds (dative bonds) to a metal (cation) located at the centre of a coordination complex. If the ligand is a neutral dipolar molecule, such as water, the negative end of the dipole bonds with the central metal.

Though there are many possible coordination geometries in chemistry, in mineralogy it is octahedral and tetrahedral coordination that are the most common. Octahedral coordination occurs when a central atom is bonded to 6 ligands

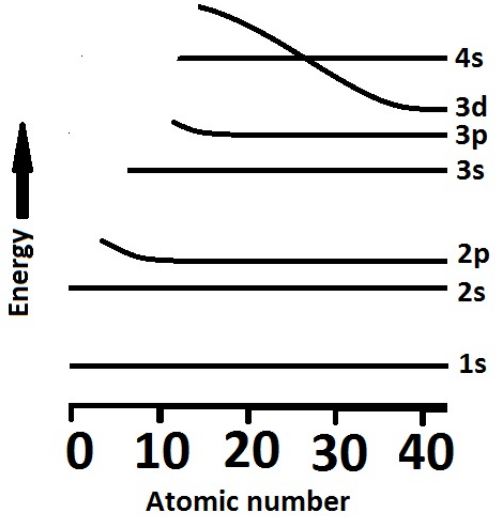


Figure 66: Subshell relative energies vs atomic number. Shells fill from bottom up. Note the location where the 3d and 4s orbital match in energy is approximately halfway through the 4th period transition metals.

spaced such that one can imagine the ligands residing along each of the Cartesian axes. Tetrahedral coordination occurs when a central metal atom is bonded to 4 ligands spaced such that one can imagine the ligands residing at opposite vertices of a cube. These two dominant mineral geometries are shown in Figure 67.

## 7.6 Crystal field theory

In a free transition metal cation, each electron in the 3d valence orbitals has the same energy (single degeneracy). If one placed a free transition metal cation in a spherically symmetric electric field, for instance from an even distribution of negative charges over a sphere surrounding the metal, the energy of each orbital would be perturbed. However, they would all be shifted the same amount of energy and the orbitals would remain singly degenerate.

In minerals, there is never a spherically symmetric surrounding field to a transition metal cation. This is because the charge responsible for the associated field is due to ligands occupying specific positions. To elaborate, consider a metal atom or ion being placed at the origin in an octahedral coordination complex. Next, imagine the ligands as negative point charges along the six Cartesian axes. There now remains mirror plane symmetry to the resulting electric field experienced by the electrons of the central metal, but the field is no longer spherically symmetric. Therefore, not all 3d orbitals exist at the same energy. They are affected differently by the geometry of the surrounding

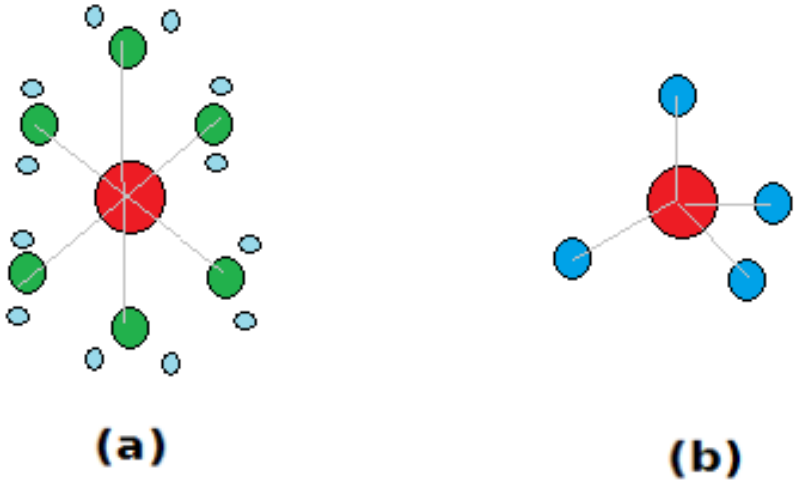


Figure 67: Coordination polyhedra with a central metal cation a) bonded to six $H_2O$ ligands in octahedral geometry and b) bonded to four oxygen ligands in tetrahedral geometry.

negative point charges. With respect to the previously discussed spherically symmetric arrangement, it now takes more energy to place an electron into the higher energy orbital and less into the lower energy orbital. The degeneracy of the metal 3d orbitals has been split. The scientific model used to describe this splitting of 3d orbital degeneracy based on electrostatic repulsion of ligands is called crystal field theory.

This degeneracy splitting can lead to changes in the colour and magnetic properties of materials. Our study is concerned with how the degeneracy splitting allows for electronic transitions that affect absorption of light in the spectral ranges relevant for our Raman spectroscopic studies and those planned for Mars 2020 and ExoMars.

For both the octahedral and tetrahedral geometries, the five 3d orbitals get split into two categories; one set of three orbitals and the other a set of 2. Which set goes up or down in energy depends on the orientation of the ligands with respect to the Cartesian axes defined using the metal as the origin. That will decide the amount of repulsion between the ligand point charges and the electron clouds of the metal.

To properly understand crystal field theory, an understanding of the description of the electron distributions which make up the 3d orbitals is required. As seen earlier in Figure 65, the $d_{xy}$, $d_{xz}$, and $d_{yz}$ orbitals are oriented in between the x and y, x and z, and y and z axes, respectively. Also shown is that the $d_{x^2-y^2}$ orbital lies along the x and y axes. Finally, the $d_{z^2}$ orbital has two lobes along the z axes and also a doughnut-like ring centred at the origin on the xy

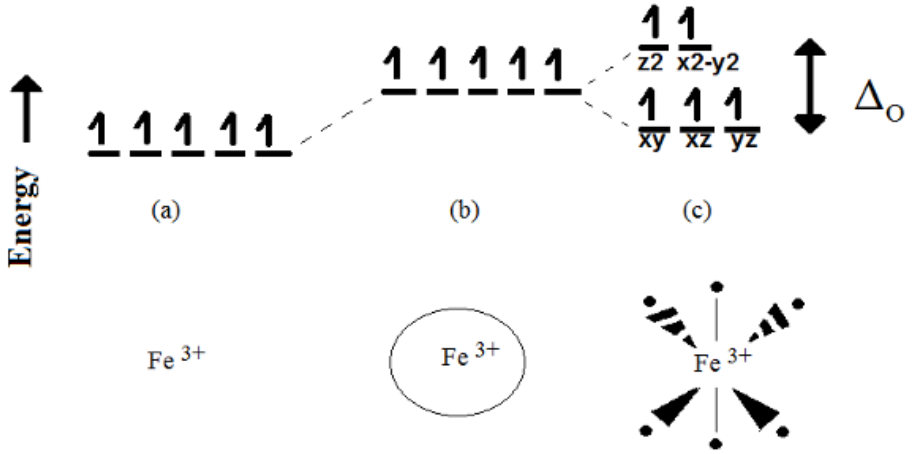


Figure 68: Iron (III) cation in a) free space b) spherically symmetric shell of charge c) octahedral coordination.

plane, circling the other two z axes lobes. Though this last orbital may seem strange, it is actually a linear combination of $d_{z^2-x^2}$ and $d_{z^2-y^2}$ , each of which would have similar shapes to the $d_{x^2-y^2}$ orbital [76].

In an octahedral complex, the six ligands are located at the vertices of the octahredon. The $d_{x^2-y^2}$ and $d_{z^2}$ orbitals of the metal, defined earlier as being oriented along the Cartesian axes, would therefore experience direct head-on electrostatic repulsion from the ligand negative point charges and increase in energy. Conversely, the $d_{xy}$, $d_{xz}$, and $d_{yz}$ metal orbitals which are not located along the Cartesian axes, experience less repulsion and therefore exist at lower energy. The energy difference between the two states is referred to as $\Delta o$. This energy difference for ferrous and ferric iron bonded to 6 water molecules corresponds to photons of wavelengths 1070 nm and 704 nm, respectively [90].

The crystal-field splitting of the d orbitals in an octahedral complex can be seen in Figure 68.

In a tetrahedral complex, the ligand point charges can be thought of as occupying four alternate vertices of a cube, with the metal located at the centre of the cube. In this arrangement none of the metal 3d orbitals are oriented directly towards a ligand point charge. However, there is still preference for one set over the other. In this geometry, the $d_{x^2-y^2}$ and $d_{z^2}$ orbitals are lowered in energy, while the $d_{xy}$, $d_{xz}$, and $d_{yz}$ orbitals are raised in energy, with respect to a spherically symmetric field. The energy difference between the two states is referred to as $\Delta t$. The energy differences are smaller for tetrahedral complexes than with the octahedral complexes such that$\Delta t$ = -4/9 $\Delta o$. The negative sign is simply to indicate that the double and triple degenerate sets are oppositely located in the two geometries.

The crystal-field splitting of the d orbitals in a tetrahedral complex can be

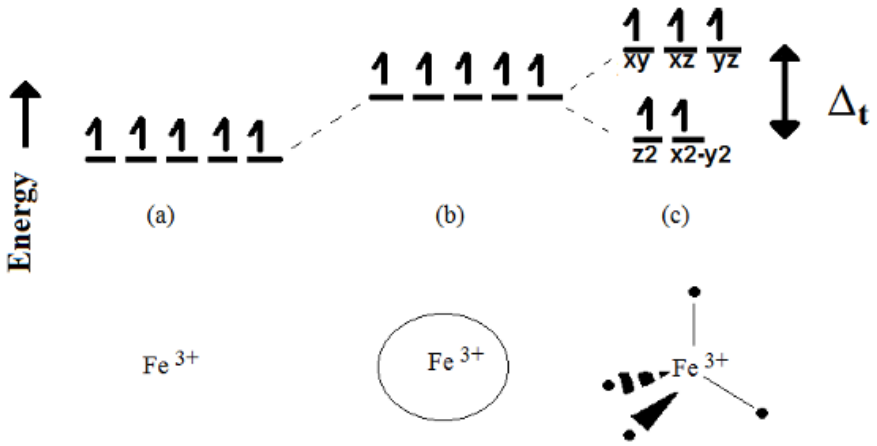


Figure 69: Iron (III) cation in a) free space b) spherically symmetric shell of charge c) tetrahedral coordination. Note that $\Delta t$ =a -4/9 $\Delta o$.

seen in the Figure 69.

There are other factors that determine the value of $\Delta$ besides the polyhedron geometry.

Firstly, $\Delta$ is proportional to $r^4$, where r is the mean radial distance of the 3d orbitals from the nucleus. This will be a function of cation radius and effective nuclear charge [76].

Secondly, $\Delta$ is proportional to $R^{-5}$, where R is the metal–ligand distance. This is affected by pressure (increase = blue shift) and temperature (increase = red shift) [76].

Thirdly, the asymmetry which results when ligand occupation sites on the same complex host different ligand types will affect $\Delta$. For instance, in some minerals examined in this study, certain ligand sites are occupied by an $O^{2-}$ ligand while others in the same complex are occupied by an $OH^-$ ligand. The iron in natrojarosite is bonded to four hydroxyls and two oxygens. Another situation could result when cis and trans versions of a complex exist. In a true octahedron, all metal-ligand distances are equivalent and all ligand-metal-ligand angles are 90 degrees. Neither statement is true if any asymmetry exists.

Vibronic coupling modes (the interaction between electronic and nuclear vibrational motion) in coordination complexes may cause the central metal cation to shift from its equilibrium centrosymmetric location, thereby changing the energy difference between certain orbitals. Since some molecular vibrations are activated by thermal energy, one can expect broader absorption peaks at higher temperatures.

Filling orbitals when there is a split in degeneracy is more complex than simply following Hund's rule (greater total spin = more stable atom) or a preference for the lower energy orbital. One must also consider the energy it takes

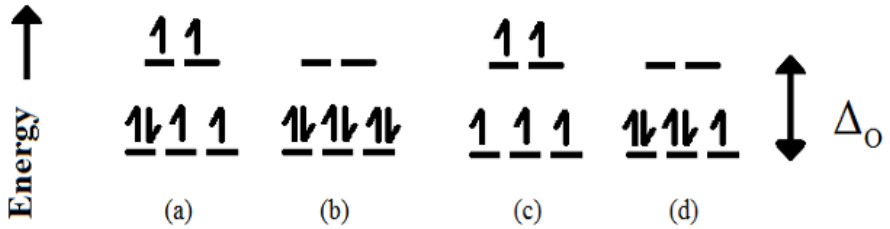


Figure 70: Iron (II) cation in a) high spin b) low spin states, and Iron (III) cation in c) high spin d) low spin states.

to overcome repulsive forces to place two electrons in the same orbital. This is called the electron pairing energy.

To predict which electrons are in which orbitals for certain oxidation states, one needs to compare the value of $\Delta$ with that of the pairing energy. For instance, consider a cation with four 3d electrons. If the pairing energy to place the 4th electron in the same orbital as one of the other three is less than $\Delta$, the 4th electron will go into the lower energy orbital, in contradiction to Hund's rule (reducing the total spin state). However, if the pairing energy is more than $\Delta$, the 4th electron will go into the higher energy orbital, agreeing with Hund's rule. The situation with the most unpaired electrons is known as the high spin arrangement, while that with the least unpaired electrons is known as the low spin arrangement. One must note that the pairing energy of an electron actually changes depending on the oxidation state of an atom. For $Fe^{2+}$ and $Fe^{3+}$, the pairing energies correspond to photons of wavelengths 334 nm and 522 nm, respectively [76]. One must only consider this electron paring energy comparison with $\Delta$ for 4th period transition metal elements in octahedral coordination. The ground state of heavier transition metals in octahedral coordination is always the low spin state[90], whereas ground state transition metals in tetrahedral coordination complexes are always in the high spin state [90]. Figure 70 shows the possible spin states of ferrous and ferric iron.

Spin crossover, which is a spin state change, can be caused by external stimuli such as variations in temperature. It may be observed if the energy between states is comparable to the thermal energy ($\Delta E = k_b T$, where $k_b$ = Boltzmann constant, T= temperature) [91].

In addition to the factors affecting the crystal field splitting parameter $\Delta$ mentioned above, there are factors which further split the degeneracy of the associated orbitals.

The Jahn-Teller effect describes how complexes containing degenerate electronic states will undergo a geometrical distortion to remove degeneracy. This is a quantum mechanical effect that leads to broader absorption bands. The mathematics describing this effect are beyond the scope of this study and the reader is encouraged to see Henderson and Bartram [92] for further details.

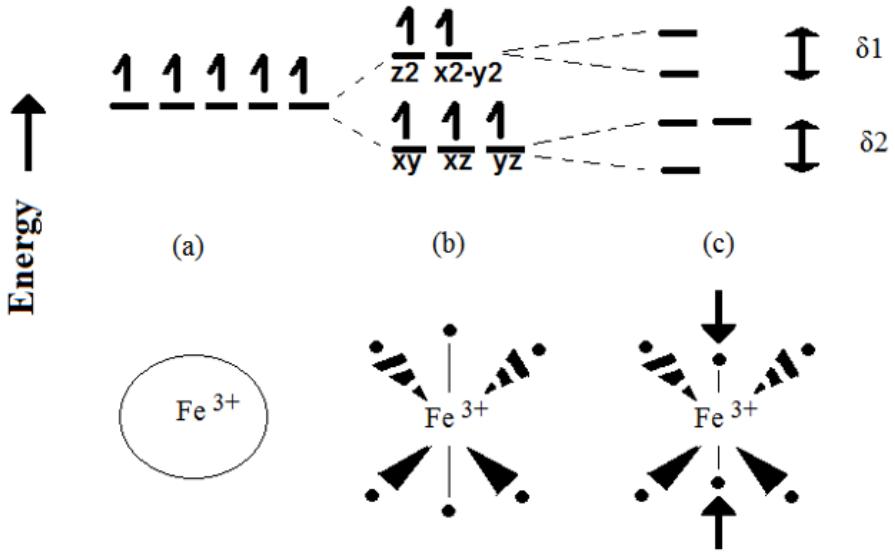


Figure 71: Iron (III) cation in a) spherically symmetric shell of charge, b) octahedral field (high spin), c) octahedral field distorted in z-direction, further splitting d orbital degeneracy.

Partially occupied sigma anti-bonding orbitals (described in section 7.7) lead to more pronounced Jahn-Teller distortions than partially occupied non-bonding orbitals [90]. However, both sets of orbitals end up split by the effect.

In Figure 71, a z-direction distortion due to the Jahn-Teller effect is shown.

Each electron orbiting an atom produces two magnetic fields. The first field is due to the intrinsic spin of the electron, while the second is due to the orbital motion of the electron about the atom. Electron quantum states where these two fields are opposite are more stable, thereby splitting the degeneracy of two electrons in the same n, $\ell$, and $m_\ell$, state. This is called spin orbit coupling and it too increases the breadth of absorption peaks.

Crystal field theory is not perfect. It is used mostly for a qualitative understanding of electron transitions in transition-metal bearing minerals. However, it is not good for quantitative prediction of the energy or breadth of absorption peaks. This is because crystal field theory ignores both covalency of the metal-ligand bonds and orbital overlap. It also treats the metal cation and ligand as point charges, when in reality, they both have an ionic radius and an effective nuclear charge. Ferrous iron has ionic radii of 61 and 78 pm in the low and high spin states, respectively, while ferric iron has ionic radii of 55 and 64.5 pm in the low and high spin states, respectively. The decrease in radii with respect to oxidation state is a result of diminished effective nuclear charge.

Due to these omissions, crystal field theory cannot explain the spectrochemical series. That is, it does not properly describe the relative 'strength' of ligands

as displayed in the following trend:

$$Br^- < Cl^- < F^- < OH^- < O_2^{--} < H_2O < SCN^- < NH_3$$

This mineralogy study is only concerned with $OH^-$, $O_2^-$, and $H_2O$ ligands.

## 7.7 Ligand field theory

To delve into better detail about what is actually happening in a coordination complex with respect to covalent bonding (electron orbital overlap, electron sharing, strength of metal-ligand bonds), one must look to molecular orbital theory. This theory assumes all valence electrons are shared by all nuclei within a molecule. Electrons are no longer assigned to individual atomic orbitals (A.O.s). Instead, electrons are treated as under the influence of all the nuclei in the molecule and the A.O.s combine to form molecular orbitals (M.O.s). The M.O.s formed are either bonding, non-bonding, or anti-bonding. In the ground state, the bonding orbitals will be filled, some or all of the non-bonding orbitals may be filled, and contrary to what their name suggests, some anti-bonding orbitals may be occupied. Applying molecular orbital theory to the bonds between transition-metal cations and ligands is referred as ligand field theory. It has more success for quantitatively describing electronic transitions in transition-metal complexes.

Bonding orbitals overlap and hold the molecule together. Anti-bonding orbitals overlap, but oppose one another. Non-bonding orbitals may overlap only slightly, do not oppose one another, and are mostly neutral with respect to holding the molecule together. The shapes of bonding and anti-bonding orbitals are the same [90].

There are three rules which summarize the combination of atomic orbitals to construct molecular orbitals as follows[92]:

> 1) The number of M.O.s formed must be equal to the number of A.O.s that they were created from.
>
> 2) The combining orbitals must have matching symmetry properties. No individual ligand orbitals line up perfectly symmetrical with a metal orbital. The ligand orbitals must be symmetry-adapted by taking suitable linear combinations.
>
> 3) The combining orbitals must have similar energies and their electron distributions must overlap in the same general area of space. For bonding orbitals, the more similar the energies and the more spatial overlap of the orbitals, the lower in energy of the resulting molecular orbitals. For anti-bonding orbitals, the converse is true.

One needs to understand the two types of covalent bond orientations that can exist in these crystals. The stronger of the two bond types, a sigma bond, is a head-on overlap of orbitals along the internuclear axis as shown in Figure 72. The weaker type, a pi bond, occurs when the lobes of the A.O.s overlap each other in a non-head-on manner as in Figure 73. Wavefunctions of the orbitals

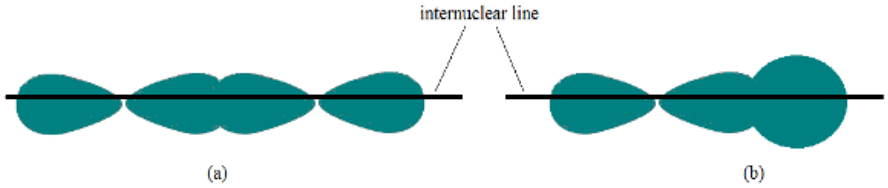


Figure 72: Sigma bonding between a) $p_y$ and $p_y$ orbitals b) $p_y$ and s orbitals.

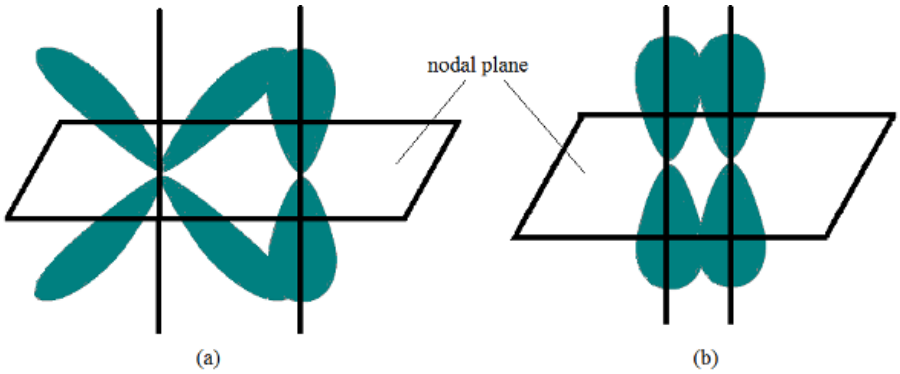


Figure 73: Pi bonding between a) $p_z$ and $d_{yz}$ orbitals b) $p_z$ and $p_z$ orbitals

that overlap this second way are zero at a common nodal plane that passes through the two bonded nuclei.

Sigma bonding M.O.s are the lowest in energy, followed by pi bonding orbitals, non-bonding orbitals, pi anti-bonding orbitals, and finally, sigma anti-bonding orbitals.

The bonding between a metal cation and a ligand is 'sigma-only' if the ligand donates only one pair of electrons to the metal. However, if the ligand has additional available electron pairs in the p sub-shell to donate, those additional electrons will form a pi bond and this is called a 'pi donor' M.O. In octahedral complexes, the orientations of the ligand p orbitals are good for creating pi bonds with the off-Cartesian axes $d_{xy}$, $d_{xz}$, and $d_{yz}$ orbitals. Water is the only relevant ligand in mineralogy that is almost 100% sigma only. The hydroxyl and oxygen ions are slightly pi donating. This pi bonding splits the degeneracy of the non-bonding orbitals into a metal-ligand bonding orbital and a metal-ligand non-bonding orbital.

It is important to note that the argon core of the metal as well as the 1s and 2s orbitals of the ligand are much lower in energy than the valence orbitals of

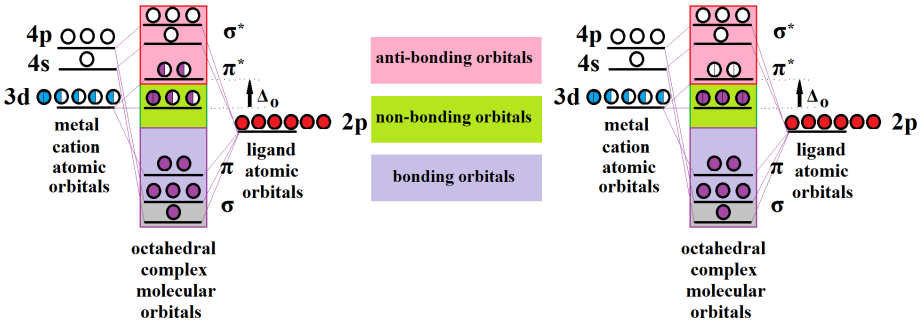


Figure 74: Molecular orbital diagrams for an octahedral coordination complex showing occupancies from a $d^6$ cation such as $Fe^{2+}$. Image on left is the high spin state and image on right is the low spin state.

the metal and ligand. These lower-energy orbitals are assumed to be entirely localized on their respective atom and are therefore completely non-bonding. In Figure 74, where energy increases from bottom to top, the A.O.s of the metal cation and ligand are shown to combine to form M.O.s. In this figure, the $d_{x^2-y^2}$ and $d_{z^2}$ orbitals are pi anti-bonding, while the $d_{xy}$, $d_{xz}$, and $d_{yz}$ orbitals are non-bonding.

If the cation orbitals directed along the Cartesian axes are empty in an octahedral geometry, they easily overlap with filled ligand p orbitals. Bonding M.O.s correspond to the maximum overlap of the A.O. wavefunctions which created them. These resulting orbitals are more stable than the individual orbitals of either the cation or ligand which combined to form them.

If the energy of the resulting molecular orbital is closer to that of the cation A.O. which helped create it, the characteristic of the M.O. will be more similar to the cation A.O. The converse is true of the energy of the resulting M.O. is closer to that of the ligand.

## 7.8 Selection rules for electronic transitions

The *Laporte selection rule* states that orbital transitions are forbidden if both states involved are of the same principal quantum number and azimuthal quantum number (i.e. two 3d orbitals, two 4f orbitals, etc.). In other words, a transition would be forbidden if it simply involves redistributing electrons within the same type of orbital in a single quantum shell. In this context the word forbidden does not mean it cannot happen. Instead, it means that the transition has a low probability of occurring. Forbidden transitions become temporarily allowed if there is a disruption of the centre of symmetry of a complex. Therefore, some vibrations due to heat will momentarily allow forbidden transitions to occur. The reason a Laporte transition occurs even when the quantum numbers are the same is explained by mixing of a ligand p orbital into one of the d orbitals of the metal when this vibration induced asymmetry occurs. This mixing changes

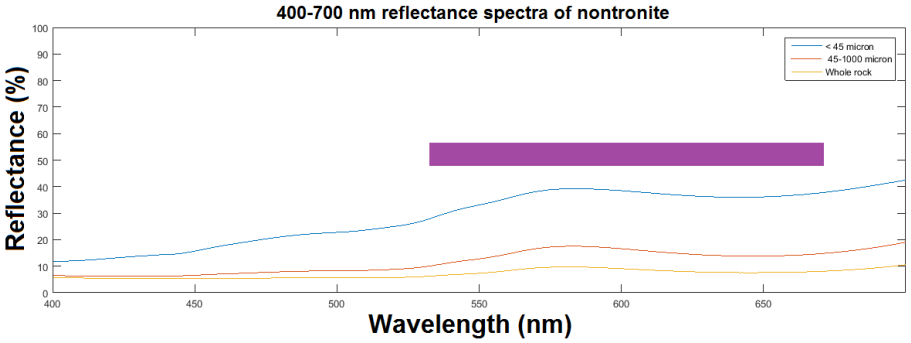


Figure 75: Visible region reflectance spectra of nontronite at various grain sizes taken at the University of Winnipeg[9]. Purple box denotes our green Raman window.

one of the two d orbitals involved in the transition into a p-d mixture. This occurs more with pi donor ligands. At no point does a tetrahedral complex have a centre of symmetry. Therefore, 3d-3d transitions in these complexes are not considered Laporte forbidden. A way to mathematically think about the Laporte rule is that transitions from orbitals with wavefunctions such that $\Psi$(x,y,z) = $\Psi$(-x, -y, -z) to those of the same characteristic are Laporte forbidden [92]. The same is true of transitions from orbitals with wavefunctions such that $\Psi$(x,y,z) = -$\Psi$(-x, -y, -z).

The *spin selection rule* sates that a transition is forbidden if during that transition the total number of unpaired electrons changes. Where we are concerned with a single electron transitioning in a complex, the spin state, $m_s$, of that electron must be identical before and after the transition.

## 7.9 Possible electronic transitions in coordination complexes

### 7.9.1 Crystal field transitions (d-d)

The lowest energy transitions (VIS and NIR) are due to a 3d electron being excited from the lower to higher energy of the two split d orbital sets. This d-d transition is also known as a crystal-field (CF) transition. These transitions are Laporte forbidden and often spin forbidden, thus their intensity is weak compared to other transitions. Although they are weak, it is these transitions which are mostly responsible for the colour we observe for transition-metal bearing minerals (i.e. gemstones). Figures 75-78 were created using VIS spectral reflectance data sets of the same aqueous alteration minerals taken at the Planetary Spectrophotometry Facility (University of Winnipeg) and provided courtesy of Ed Cloutis and Matt Izawa [9]. One can clearly see that even at 532 nm, absorption in the high iron content mineral nontronite is significant.

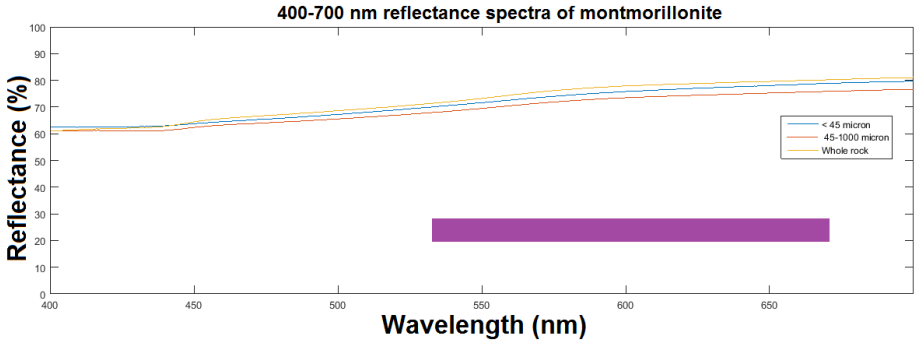


Figure 76: Visible region reflectance spectra of montmorillonite at various grain sizes taken at the University of Winnipeg[9]. Purple box denotes our green Raman window.

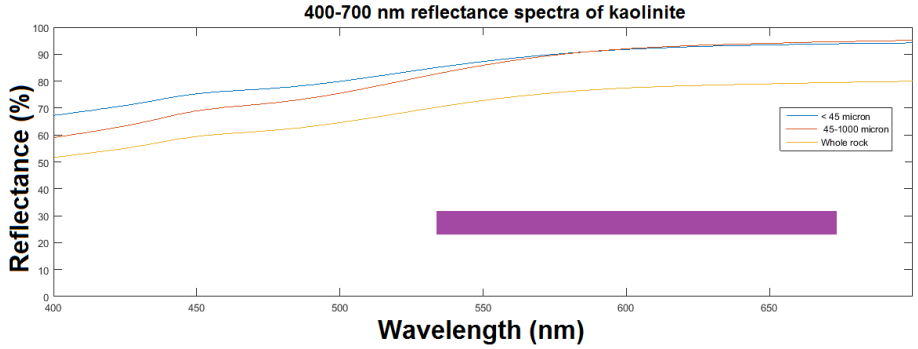


Figure 77: Visible region reflectance spectra of kaolinite at various grain sizes taken at the University of Winnipeg[9]. Purple box denotes our green Raman window.

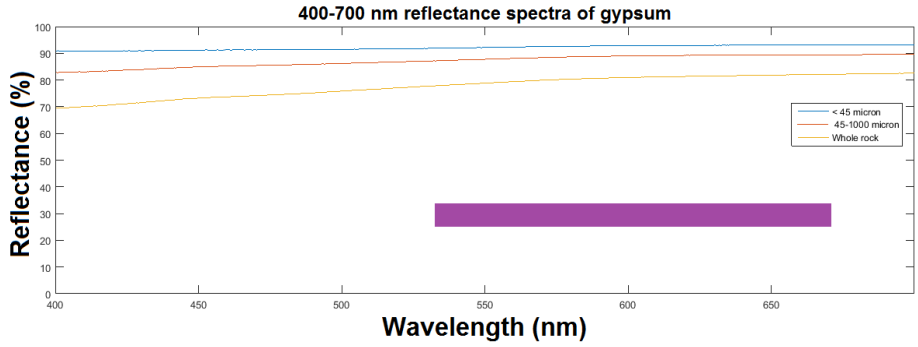


Figure 78: Visible region reflectance spectra of gypsum at various grain sizes taken at the University of Winnipeg[9]. Purple box denotes our green Raman window.

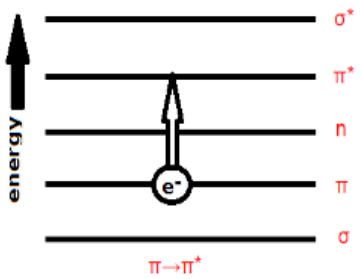


Figure 79: Charge-transfer transition from a bonding orbital predominantly localized on ligand to an anti-bonding orbital predominantly localized on metal.

### 7.9.2 Intervalence charge transfers

The next higher energy transitions (VIS and near UV) are due to metal-metal intervalence charge transfers (IVCT) between cations in adjacent coordination sites. These transfers can be from the same cations in different oxidation states (homonuclear, i.e. $Fe^{2+}$ –> $Fe^{3+}$) or different cations (heteronuclear, $Fe^{2+}$ –> $Ti^{4+}$ ). The heteronuclear charge transfers are higher energy than the homonuclear. These transitions are both spin and Laporte allowed, and therefore produce medium to high intensity absorption bands ($10^1$-$10^3$ more intense than crystal field bands.). Electron movement may be blocked by substitutions of transition metals by non-transition metals such as Mg and Al in adjacent coordination complexes. Though most of these transitions are in the visible region, Burns [76] reported $Mn^{2+}$ –> $Ti^{4+}$ charge transfers causing an absorption at 325 nm. Many IVCT transitions can be very broad.

We note that at the green wavelength of 532 nm planned for both ExoMars RLS and Mars 2020 SuperCam, absorptions due to these first two transition types (d-d and IVCT) are especially high for cobalt, titanium, and are of medium intensity for chromium.

### 7.9.3 Ligand-metal charge transfers

The highest energy transitions (UV) are due to ligand-metal charge transfers (LMCT) from the oxygen (ligand) 2p orbital to the metal 3d orbital. Contradicting this sentence, it was mentioned earlier that in molecular orbitals the electrons are shared between all nuclei in the molecule. Therefore, to clarify, when it is described here that the electron transitions from a ligand orbital to a metal orbital, what is actually meant is that it is transitioning from an orbital that is mostly ligand in character (predominantly localized on the ligand) to an orbital that is mostly metal in character (predominantly localized on the metal). These LMCT transitions correspond to higher energy UV photons because the ligand-character M.O.s lie so low in energy in comparison to the metal-character M.O.s.

LMCT transitions are both spin allowed and Laporte allowed, so they produce very high intensity absorption peaks. These absorptions are $10^3$-$10^5$ more intense than crystal field bands. The energy of a LMCT transition is usually a function of metal type and coordination site geometry. The following series compares the transition energies of various metal cations and oxidation states:

$$Cr^{3+} > Ti^{3+} > Fe^{2+} > Fe^{3+}(\text{tetrahedral}) > Fe^{3+}(\text{octahedral}) > Ti^{4+}$$

An older study by Burns [93] placed the $Ti^{4+}$ in between the ferrous and ferric iron.

It is difficult to theoretically predict the wavelength of an absorption corresponding to an LMCT transition because both the cation, ligand and all their neighbouring ions must be considered as one system when calculating energy levels. This could include hundreds or thousands of electrons. However, the relative binding energies of oxygen 2p and metal 3d orbitals can be estimated through UV photoelectron spectroscopy of simple oxides and silicates. This transition energy estimate is made by taking the difference in binding energies. The energy is the difference between what is required to remove an electron from an oxygen 2p orbital (ionization energy) and the electron accepting energy (electron affinity) of an iron 3d orbital. This energy is then adjusted by the resulting electrostatic attraction between acceptor and donor. Though application of these values to complex minerals such as layered silicates and hydrous sulphates may not yield exact matching results of band position, the results of these simpler minerals do show that LMCT transitions definitely reside in the UV region of the spectrum.

### 7.9.4 Charge transfers and delocalized electrons

In some minerals such as magnetite ($Fe_3O_4$) and hematite ($Fe_2O_3$), there exist charge transfer mechanisms which are believed to cause electron delocalization. This means that the electrons behave essentially as free charge carriers, above the valence band, but below the conduction band. This results in opacity over a wide spectral range [94]. Burns [93] suggested that this phenomenon causes discrete valencies to become indistinguishable valencies, thereby eliminating characteristic properties of single valence states. Magnetite, which contains infinite chains of ferric iron in tetrahedral coordination as well as both ferrous and ferric iron in octahedral coordination, displays complete opacity in the UV due to electron delocalization. Burns suggests that iron end member silicates (nontronite in our study) are expected to exhibit electron delocalization. The opacity of the nontronite spectrum shown in Figure 61 is proof of this theory.

Wagner, Hapke and Wells [95] have a slightly different explanation when speaking about UV absorption of minerals in the far-ultraviolet. They refer to these transitions as valence-conduction band transitions occurring between the bonding electrons in the filled or partially filled valence band and empty anti-bonding locations in the conduction band.

## 7.10 Experimentally observed and theoretically predicted UV electronic transitions in previous studies

### 7.10.1 Wells et al

Wells et al [96] suggested that lunar soil has a low UV reflectivity because of an abundance of metallic iron in submicroscopic particles. The suggested mechanism for the creation of such particles is vaporization due to meteorite impacts and subsequent re-condensation of the same material. The same study found what they suggested was a charge transfer band due to an $O^{2-}$–>$Ti^{4+}$ transition at 260 nm, and two charge transfer bands due to heteronuclear IVCT transitions from $Fe^{2+}$ –> $Ti^{4+}$ at 340 and 420 nm. In the laboratory, they also determined that absorptivity is higher in vacuum-melts than in air-melts.

### 7.10.2 Loffler et al

Loffler et al [97] predicted $O^{2-}$–>$Ti^{4+}$bands at both 260 and 300 nm, and $O^{2-}$–>$Ti^{3+}$ bands at 220 and 250 nm. The same study predicted $O^{2-}$–> $Fe^{2+}$ bands at 270 nm.

### 7.10.3 Cloutis et al

Cloutis et al. [88] reported that the most dominant $O^{2-}$–> $Fe^{3+}$ absorption band occurs at a shorter wavelength (~210-230 nm) than that of the $O^{2-}$–> $Fe^{2+}$band (~250-270 nm). They observed absorption maxima in hematite at 240, 280 and 345 nm. In the same study, goethite (FeOOH), a possible precursor to Martian hematite, showed absorption maxima at 240 and 330 nm, while a jarosite + goethite combination exhibited a reflectance minimum at 262 nm. Spectra of many iron oxides in their study show similar reflectance minima between 240 and 250 nm. Two important observations they made were that bands appear to be superimposed on a broad sloping continuum and that UV absorption intensity can be a function of grain size.

### 7.10.4 Sherman and Vergo

Sherman and Vergo [98] found bands in both montmorillonite and nontronite attributable to $Fe^{3+}$ around 220 nm. They also found bands around 260nm (montmorillionite) and 270 nm (nontronite) attributable to $Fe^{2+}$.

### 7.10.5 Burns

Roger Burns reported [76]LMCT transitions for $O^{2-}$–> $Fe^{3+}$ at 262 nm, 248 nm, and 229 nm. He also reported a single LMCT transition at 235 nm for $O^{2-}$–> $Fe^{2+}$.

## 7.11 Summary of UV absorption in transition metal bearing minerals and the implications for Raman usage on Mars

UV spectroscopy of transition metal bearing minerals shows intense absorption due to charge-transfer electronic transitions. The Laporte and spin allowed transition of an electron from an oxygen 2p orbital to a metal 3d orbital (ligand-metal charge transfer) is the most intense of these charge transfers absorption bands. These bands can be so broad that few, if any, well-defined bands can be observed [88].

Band broadness is caused by multiple decreases in degeneracy of the metal 3d orbitals. This is due to crystal field splitting, the Jahn-Teller effect, spin-orbit coupling, and asymmetric ligand site filling.

Intense and broad UV absorption in these minerals, coupled with the weakness of the inelastic scattering process, leads to poor UV Raman spectra for many Mars analogue minerals. Since jarosite is considered to be a main constituent of the global dust storms [62], one can expect that most of the Martian surface has some iron content. Noting that even trace amounts ($<$0.01 wt%) [88] of transition metals can eliminate the spectral signature from a sample, the use of UV Raman may prove difficult for Mars exploration. We note that Bell and Ansty [99] examined UV reflectance spectroscopy data from the Hubble Space Telescope as energetic as ~295 nm. Their data showed low reflectance from all Mars regions examined.

We close this section by mentioning that pelletizing our clays was attempted, but that preparation did not yield better Raman results.

# 8 Methodology II: Organic + mineral mixtures

## 8.1 Published parallel research

There have been previous studies concerning detection of organics within a mineral matrix. Certain aspects of the previous work overlap with this study. Vitek et al [34] used Raman spectroscopy to determine if low concentrations of beta-carotene could be identified through single crystals of gypsum. Beta-carotene is a UV-protective pigment which could be indicative of a survival strategy of microorganisms in an extreme habitat such as the high UV radiation environment of an ozone layer-lacking planet such as Mars.

Two more studies used Raman spectroscopy for organics detection in a planetary exploration context, Carrier et al at the Jet Propulsion Laboratory and Eshelman et al at York University. Carrier et al [55], examined phenylalanine and alanine in both gypsum and kaolinite at 248 nm. Eshelman et al [2] examined stearic acid in a simple quartz matrix using almost the same UV system as this study.

Instead of Raman spectroscopy, Richardson [40] used laser desorption Fourier transform mass spectrometry for biosignature detection in a mineral matrix. He examined stearic acid in the sodium sulphate, thenardite. Though thenardite is formed in much less acidic conditions than natrojarosite, similar to nartojarosite, it is highly soluble and representative of arid Martian conditions.

We believe that this study was the first to attempt to use Raman spectroscopy to detect stearic acid within Mars analogue phyllosilicates and hydrated sulphates. Also, while some other studies simply mixed the organics and minerals by hand using a mortar and pestle, our mixture making method used a rotary evaporator. This allows for a more homogeneous distribution of the stearic acid across each mineral substrate. This was required as a only fraction of the mixtures created would be removed from a container to be examined at the two laboratories (York University, Royal Ontario Museum) and on different days. It was a requirement that it did not matter what portion of the container contents were being examined from one experiment to the next.

## 8.2 Rotary Evaporation

A rotary evaporator removes excess solvents from non-volatile samples. This is done by heating a round bottom flask in a hot water bath. The flask is rotated to increase the surface area, thus increasing the rate of evaporation. A vacuum pump is used to reduce the pressure within the flask. The decreased pressure lowers the boiling point of the solvent which allows the solvent to evaporate at a temperature that is less likely to have an effect on the other materials that are in the solution. Evaporating solvents at high temperatures can cause chemical reactions. By lowering the pressure and therefore the boiling temperature, the solvent is removed without side reactions. In the context of this study, the process of rotary evaporation results in an even distribution of an organic across a mineral substrate.

For this study, homogeneous mixtures of Mars analogue minerals and stearic acid at varying concentrations were desired. Ethanol was used as the solvent since a study by Heryanto et al. [100] showed that ethanol and ethyl acetate were the best organic solvents for stearic acid. Ethanol, a simple organic compound, was chosen as it is not dangerous to work with and was available in abundance in our laboratory.

The solubility of a substance depends on properties of both the solvent and solute. These properties may change with the temperature and pressure of the solution. The polarity and hydrogen bonding properties of the combined organic solvent and fatty acid explain the solubility behaviour of this system. Chemists use the concept "like dissolve like." That is, similar compounds will dissolve one another well. Stearic acid is a relatively non-polar molecule and ethanol is only slightly polar. Also, ethanol also has relatively strong hydrogen bonding properties, as does stearic acid.

To confirm that boiling stearic acid in ethanol would not change the chemical structure (decomposition), a portion of stearic acid was dissolved in ethanol, boiled to remove the ethanol, and then the remaining material was examined by Raman spectroscopy to ascertain that it was indeed still stearic acid.

Mixtures were then made of stearic acid with each of the kaolinites (KGa1b and KGa2), two of the montmorillonites (SWy2 and STx1b), and each of our hydrated sulphates. The other two montmorillonites (SAz2 and SCa3) were similar enough in composition to the Texas montmorillonite (STx1b) that mixtures were not also made with them. Also, there was not enough quantity of the nontronite samples available to make mixtures with low uncertainty in their % composition and the samples had a large amount of quartz contamination. Therefore, those iron bearing smectites were not used in the mixture study.

> The following amounts of mineral and stearic acid for concentrations of 1%, 5%, 10%, and 20% were measured using a digital scale:
>
> 1%: Mineral 2.475 g, stearic 0.025 g
>
> 5%: Mineral 2.375 g, stearic 0.125 g
>
> 10%: Mineral 2.250 g, stearic 0.250 g
>
> 20%: Mineral 2.000 g, stearic 0.500 g
>
> *Uncertainty of digital scale +/- 0.0005 g

Though total organic carbon content in terrestrial clays rarely exceeds 1% by weight averaged over the spatial scales of a whole deposit, bio-marker bearing deposits are usually non-uniformly distributed[15]. Therefore, sediments with concentrations greater than a few percent are regularly found and anomalous concentrations with even greater concentrations can exist.

*Steps for using our rotary evaporator (shown in Figure 80):*

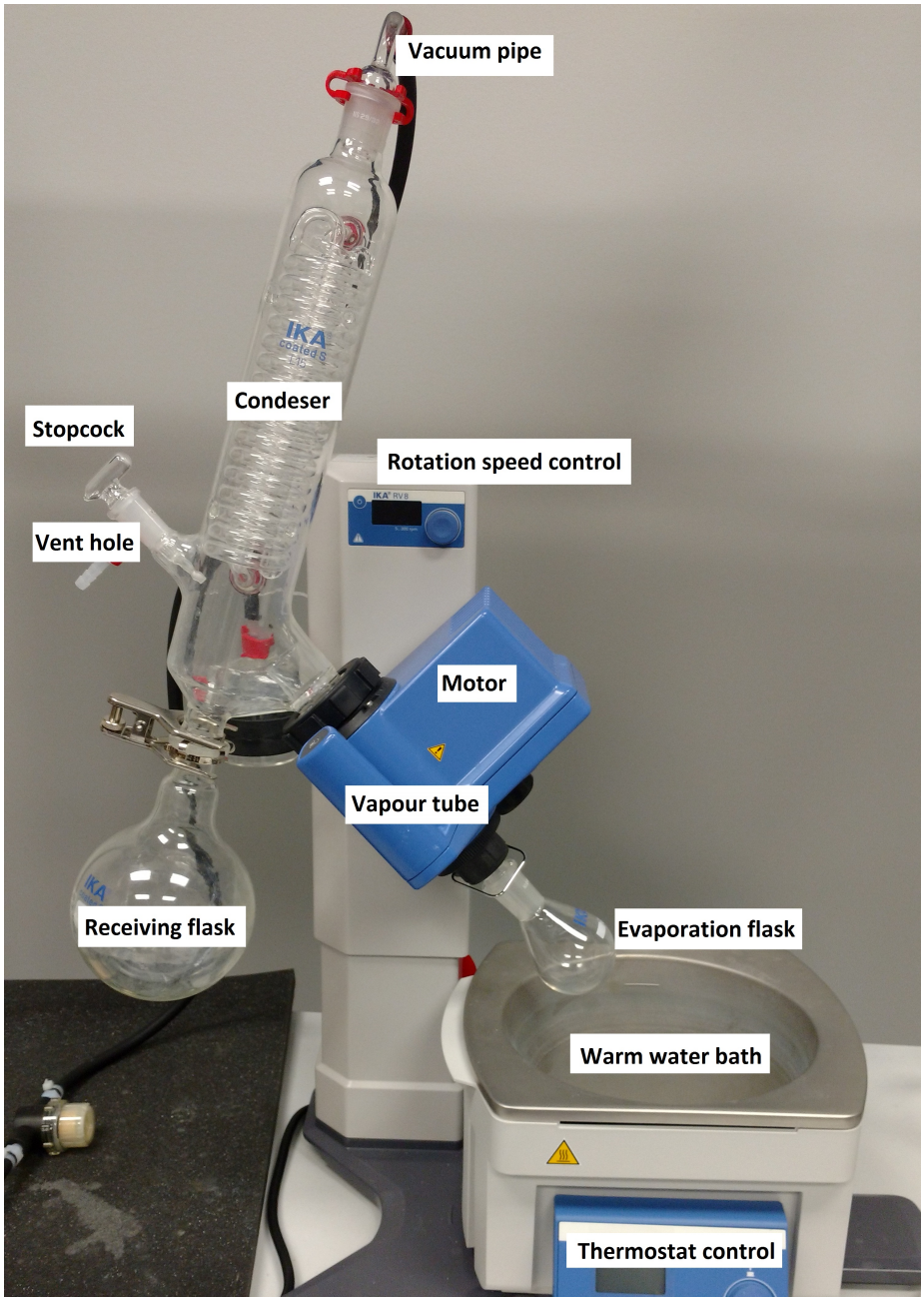


Figure 80: Ika RV8 rotary evaporator at the Planetary Exploration Instrumentation Laboratory at York University

1) Sample (solution of ethanol, stearic acid, and mineral substrate) was added to a round-bottomed evaporation flask. Flask was not more than half full with liquid.

2) Evaporation flask was attached to vapour tube.

3) Water bath was filled and turned on to heat water. Even though ethanol boils at 78.37 °C at atmospheric pressure, with the reduced pressure from the vacuum, our water bath could be set to 50 °C and still have the ethanol evaporate at a reasonable rate.

4) Rotary evaporator rotation was turned on.

5) Vacuum pump was turned on.

6) Vacuum was sealed by closing the valve on rotary evaporator condenser.

7) Flask was lowered into the hot water bath. Water level was set such that bath water just covered liquid level in flask.

8) Solvent was boiled off.

9) Rotary evaporator rotation was stopped.

10) Flask was lifted out of water bath.

11) Vacuum pump was turned off

12) Vacuum was broken by turning the stopcock, thereby opening the valve on the condenser.

13) Evaporation flask was removed so that contents could be examined with Raman spectroscopy.

14) Evaporated solvent was removed from collecting flask and disposed of.

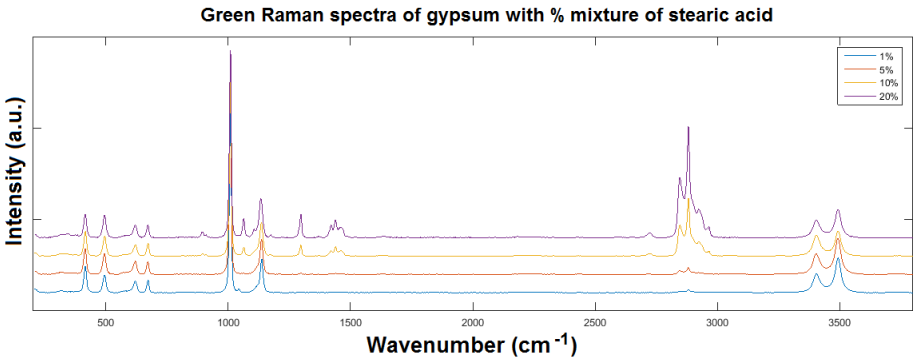


Figure 81: Raman spectra of stearic acid and gypsum at 532 nm excitation with a commercial Raman microscope.

# 9 Results of mixtures

## 9.1 Raman spectra of mixtures

This section presents the data acquired for mixtures of stearic acid with our minerals in 1%, 5%, 10%, and 20% concentrations. Data is presented raw and with background corrections to remove fluorescence where applicable. These corrections were done with a removal tool in CrystalSleuth, a free software provided by the RRUFF database.

We note how some samples with lower concentration of stearic acid produce slightly less fluorescence than those with the higher concentrations. This is important because it also means the smaller concentrations appear to have less noise once baseline corrected and therefore they also don't show as many introduced artifacts from the fluorescence removal process. Comparing the green Raman spectra of stearic with KGa2 in Figure 89 and Figure 90 demonstrates a clear example of this issue.

## 9.2 Organic detection

Table 8 lists all of the mixtures at all of the concentrations tested. The second column from the right answers the fairly qualitative question "were organics detected?" If answered yes, this means that a band was observed in a region that usually only has vibrations from organic molecules such as the C-H stretching region ~2900 $cm^{-1}$ , the disordered 'D band' ~ 1350 $cm^{-1}$ or the ordered 'G band' ~ 1610 $cm^{-1}$. Note that the 'D band' isn't as certain to be organic-only and that the 'G band' could overlap with molecular oxygen. It is mainly the C-H band that we are observing to answer this question. We note that C-H stretches in polycyclic aromatic hydrocarbons occur at different frequencies than aliphatic C-H stretches and therefore a peak ~2900 $cm^{-1}$is not only indicative of organics,

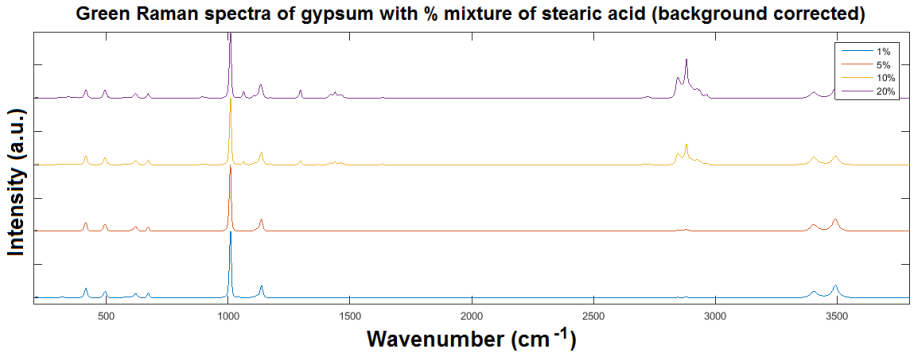


Figure 82: Raman spectra of stearic acid and gypsum at 532 nm excitation with a commercial Raman microscope, corrected for fluorescence.

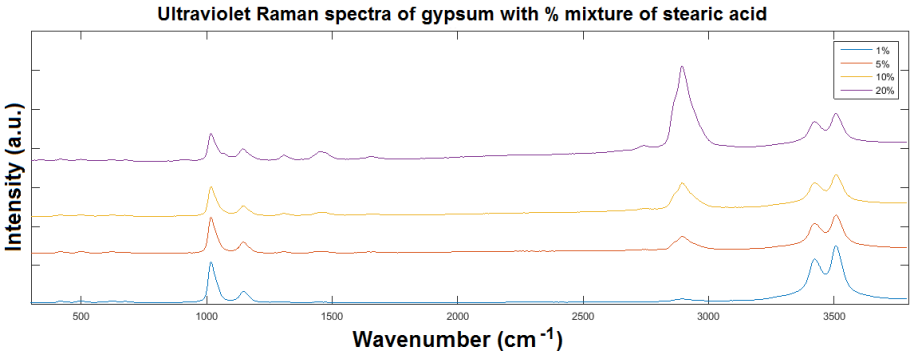


Figure 83: Raman spectra of mixtures of stearic acid and gypsum at 266 nm excitation with a prototype in-situ stand off Raman system.

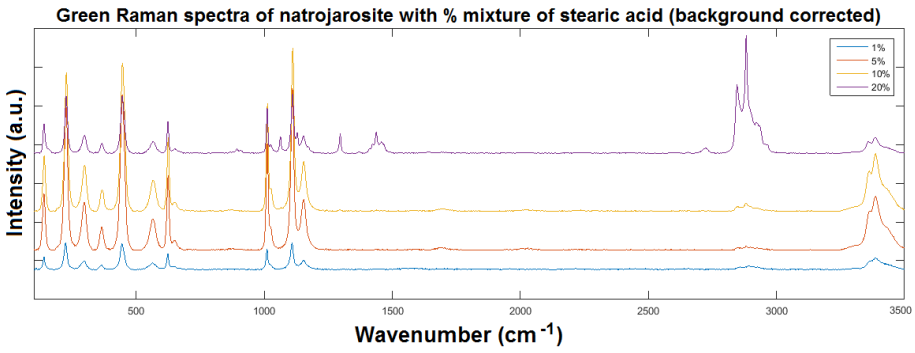


Figure 84: Raman spectra of stearic acid and natrojarosite at 532 nm excitation with a commercial Raman microscope, corrected for fluorescence..

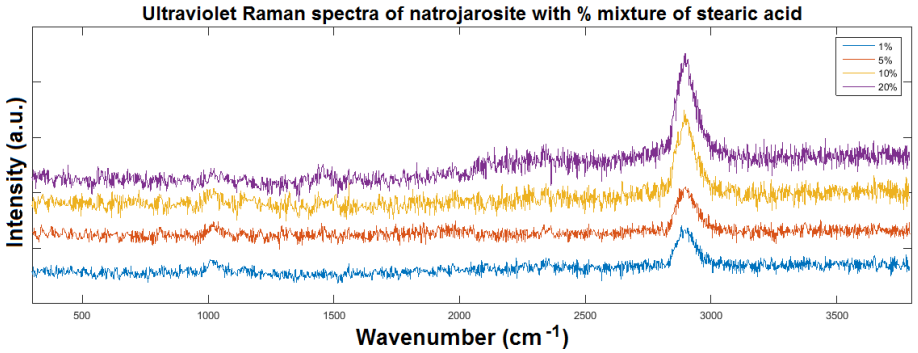


Figure 85: Raman spectra of mixtures of stearic acid and natrojarosite at 266 nm excitation with a prototype in-situ stand off Raman system.

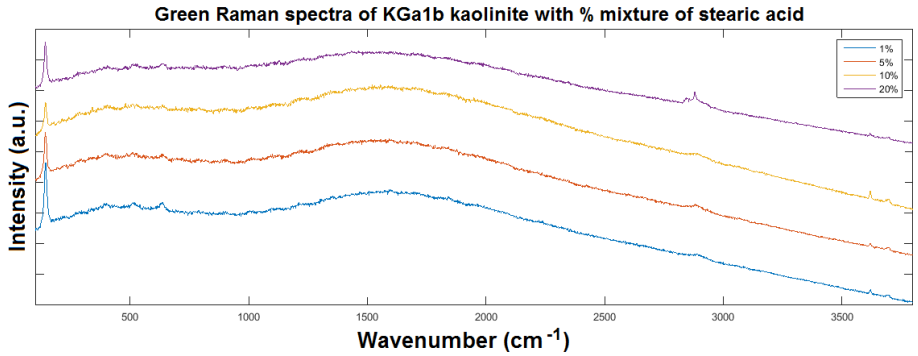


Figure 86: Raman spectra of stearic acid and kaolinite KGa1b at 532 nm excitation with a commercial Raman microscope.

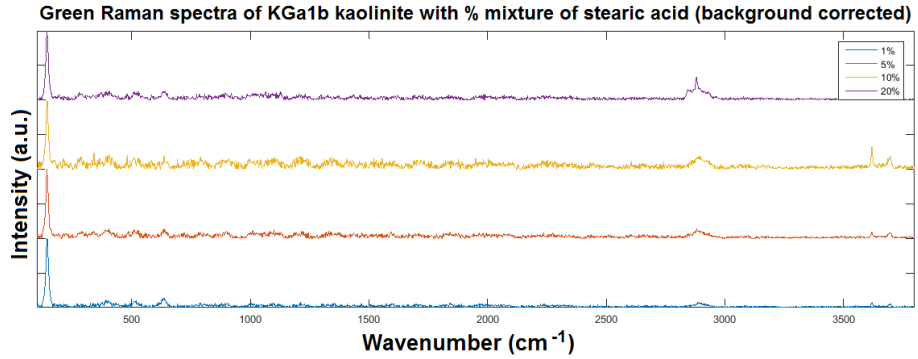


Figure 87: Raman spectra of stearic acid and kaolinite KGa1b at 532 nm excitation with a commercial Raman microscope, corrected for fluorescence.

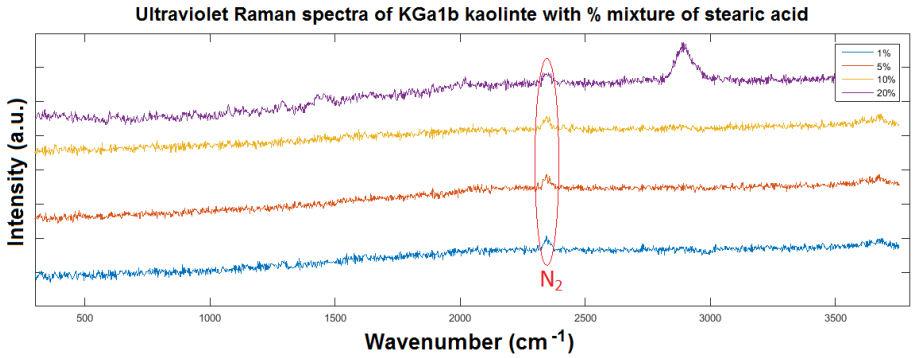


Figure 88: Raman spectra of mixtures of stearic acid and kaolinite KGa1b at 266 nm excitation with a prototype in-situ stand off Raman system.

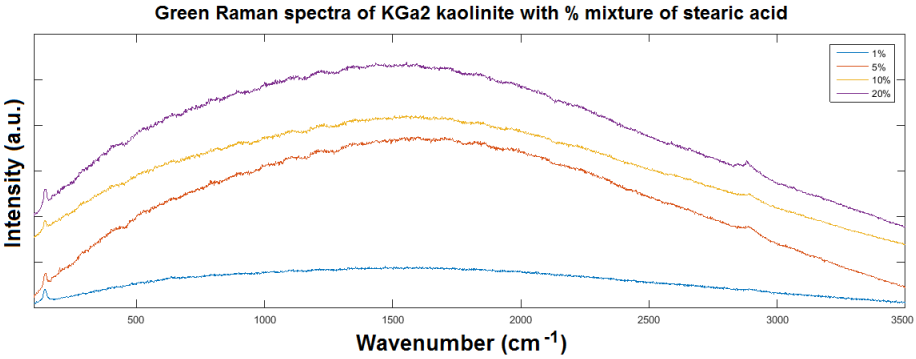


Figure 89: Raman spectra of stearic acid and kaolinite KGa2 at 532 nm excitation with a commercial Raman microscope.

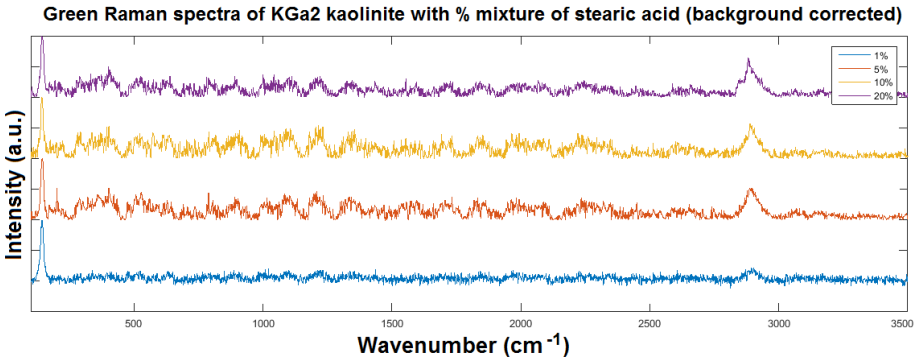


Figure 90: Raman spectra of stearic acid and kaolinite KGa2 at 532 nm excitation with a commercial Raman microscope., corrected for fluorescence.

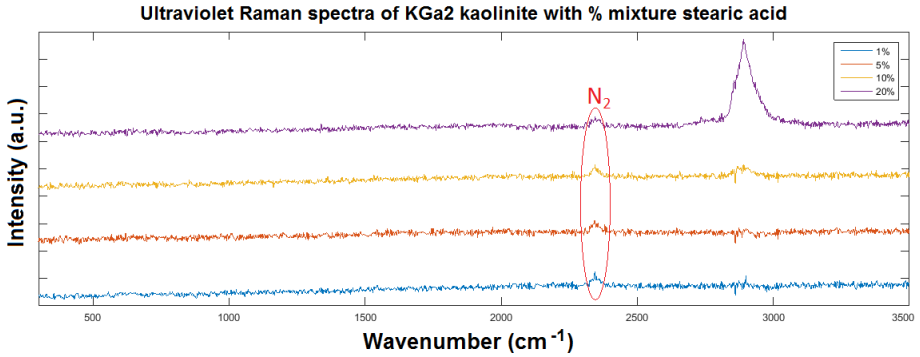


Figure 91: Raman spectra of mixtures of stearic acid and kaolinite KGa2 at 266 nm excitation with a prototype in-situ stand off Raman system.

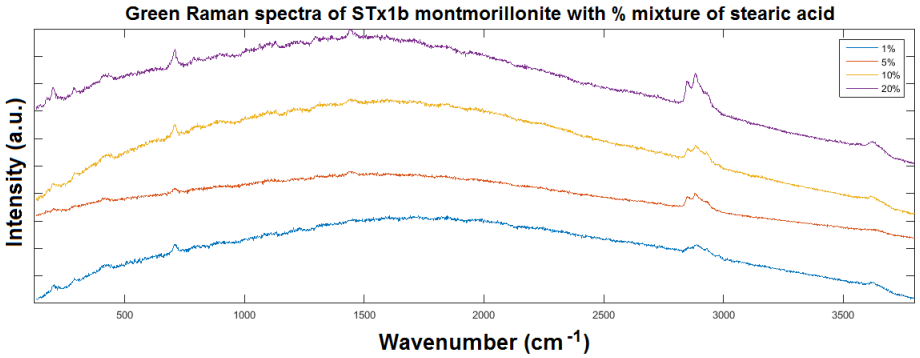


Figure 92: Raman spectra of stearic acid and montmorillonite STx1b at 532 nm excitation with a commercial Raman microscope.

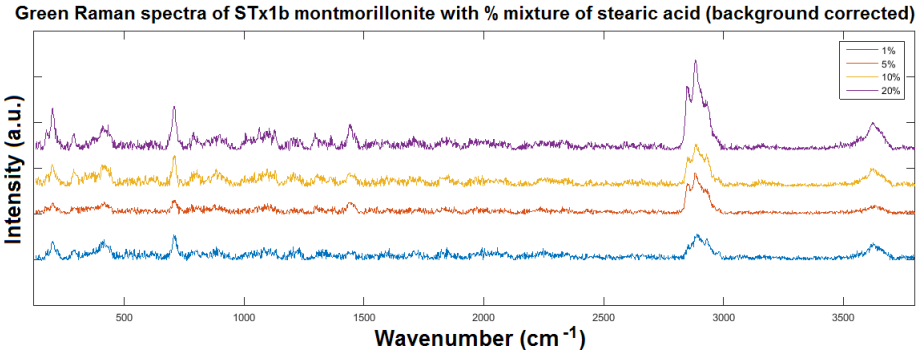


Figure 93: Raman spectra of stearic acid and montmorillonite STx1b at 532 nm excitation with a commercial Raman microscope, corrected for fluorescence.

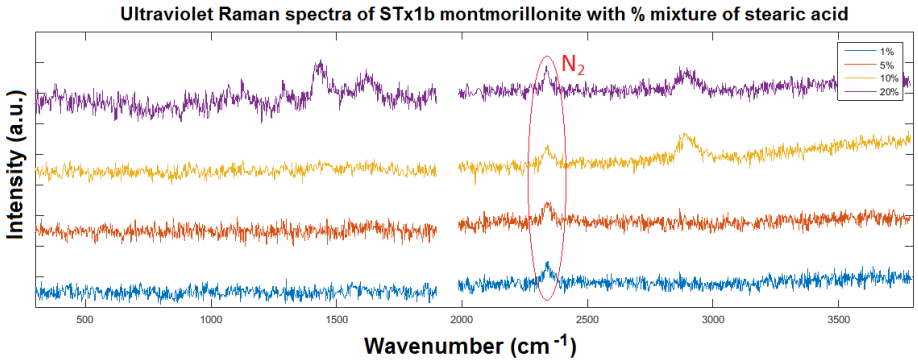


Figure 94: Raman spectra of mixtures of stearic acid and montmorillonite STx1b at 266 nm excitation with a prototype in-situ stand off Raman system.

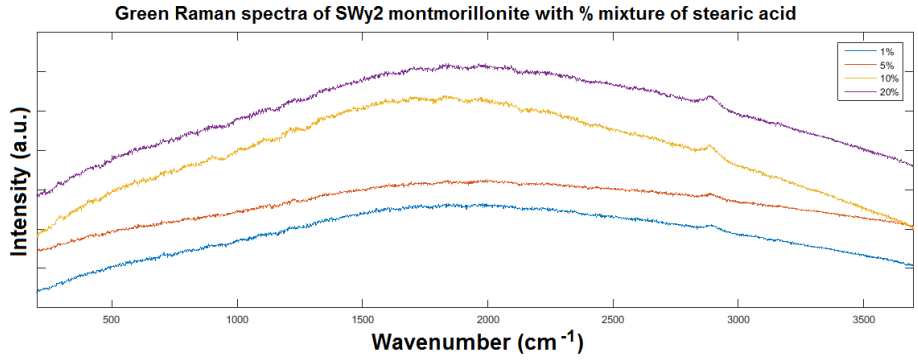


Figure 95: Raman spectra of stearic acid and montmorillonite SWy2 at 532 nm excitation with a commercial Raman microscope.

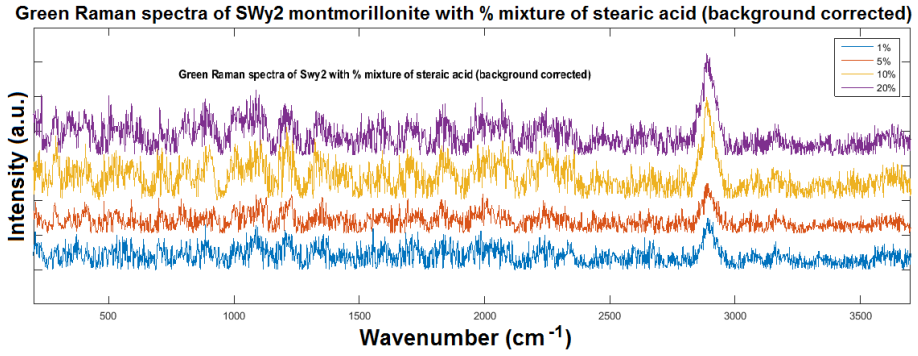


Figure 96: Raman spectra of stearic acid and montmorillonite SWy2 at 532 nm excitation with a commercial Raman microscope, corrected for fluorescence.

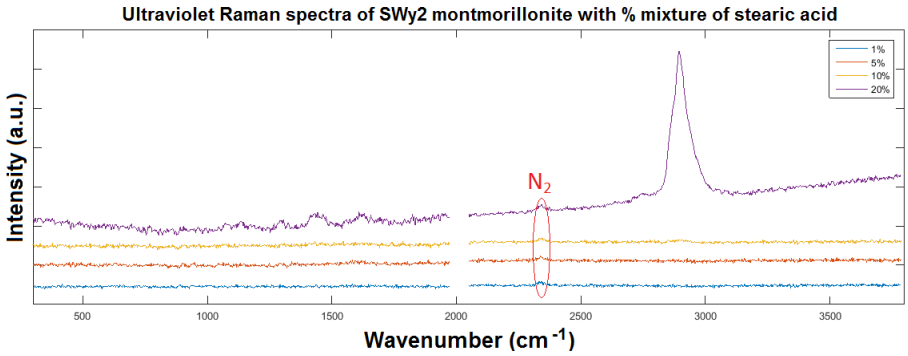


Figure 97: Raman spectra of mixtures of stearic acid and montmorillonite SWy2 at 266 nm excitation with a prototype in-situ stand off Raman system.

but specifically an organic with an aliphatic backbone. It was important in this study to keep track of which samples had prior organics contamination to differentiate between that content and newly observed content. Our clay samples in chapter 6 showed small, ill defined C-H peaks when viewed with green excitation prior to the introduction of stearic acid.

The final column on the right of Table 8 asks if the organic could be identified as a saturated fatty acid. For this, one should expect to see both a C=O stretch and C-OH stretch on top of aliphatic backbone vibrations. Both of these bonds are more polar than C-C or C-H bonds and therefore their Raman intensities are weaker. Using the relaxed requirement of Vitek et al[34] of only needing two bands for confirmation, we limit our observation requirement to only one of these two in addition to the C-H stretch. In almost all positive cases it was the C=O stretch which was observed as the second indicator. Mixtures which produced spectra with additional organics peaks than the main C-H stretch, but where those peaks were only attributed to other deformations of the aliphatic backbone, were not considered identifiable as a fatty acid.

The method used to select if a band was observable was to compare the intensity at the band location with the surrounding noise. If the intensity was more than 100 percent higher than the average value of the difference between the surrounding maximum noise and surrounding minimum noise, then the band was considered to be positively observed. Figure 98 shows the C=O stretching region both with noise and smoothed using the locally weighted polynomial regression function in Matlab. The smoothed curve clearly shows that the peak in the region is significant. One must be careful to note that the smoothing function can distort the location and relative intensities of the peaks. It is for this reason that our earlier plots did not present smoothed data.

There are researchers working on spectral matching software for organics, similar to what currently exists for minerals, but a free and accepted version is currently

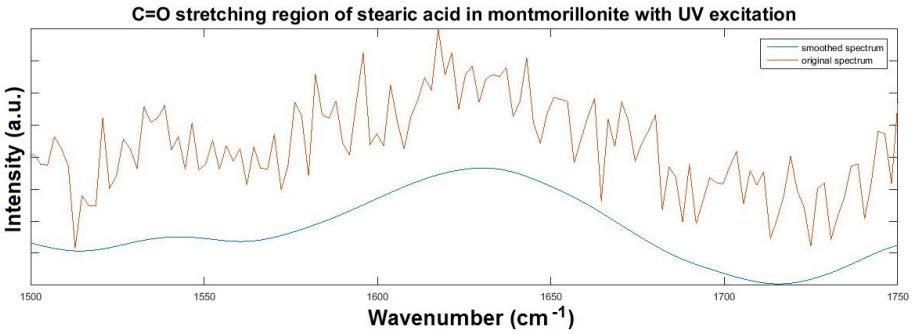


Figure 98: Raman spectra of mixtures of stearic acid and montmorillonite SWy2 at 266 nm excitation with a prototype in-situ stand off Raman system.

not publicly available. Once available, these new organics tools should allow a researcher using a Raman spectrometer with good resolution to positively identify organic type using mainly the bands $< 1100$ cm$^{-1}$ which represent deformations in the aliphatic chain. That is because these band locations may differ just enough in energy between organic types as to identify the molecule without observing the functional groups indicative of that organic group. The literature refers to the lower third of the usual Raman window as the 'fingerprinting' region.

The low frequency vibration which was suggested in chapter 5 as a possible sorting mechanism for chain lengths of saturated fatty acids was too weak of a band to be used. Only gypsum with stearic acid concentrations of 10% and above allowed us to clearly observe this band at both excitation wavelengths.

| Sample | % stearic acid | Laser (nm) | Organic? | Fatty acid? |
|---|---|---|---|---|
| Gypsum | 1 | 532 | Yes | Yes |
| Gypsum | 5 | 532 | Yes | Yes |
| Gypsum | 10 | 532 | Yes | Yes |
| Gypsum | 20 | 532 | Yes | Yes |
| Gypsum | 1 | 266 | Yes | Yes |
| Gypsum | 5 | 266 | Yes | Yes |
| Gypsum | 10 | 266 | Yes | Yes |
| Gypsum | 20 | 266 | Yes | Yes |
| Na-jarosite | 1 | 532 | Yes | No |
| Na-jarosite | 5 | 532 | Yes | Yes |
| Na-jarosite | 10 | 532 | Yes | Yes |
| Na-jarosite | 20 | 532 | Yes | Yes |
| Na-jarosite | 1 | 266 | Yes | No |
| Na-jarosite | 5 | 266 | Yes | No |
| Na-jarosite | 10 | 266 | Yes | No |
| Na-jarosite | 20 | 266 | Yes | No |
| KGa1b | 1 | 532 | No | No |
| KGa1b | 5 | 532 | No | No |
| KGa1b | 10 | 532 | Yes | No |
| KGa1b | 20 | 532 | Yes | No |
| KGa1b | 1 | 266 | No | No |
| KGa1b | 5 | 266 | No | No |
| KGa1b | 10 | 266 | No | No |
| KGa1b | 20 | 266 | Yes | No |
| KGa2 | 1 | 532 | No | No |
| KGa2 | 5 | 532 | Yes | No |
| KGa2 | 10 | 532 | Yes | No |
| KGa2 | 20 | 532 | Yes | No |
| KGa2 | 1 | 266 | No | No |
| KGa2 | 5 | 266 | No | No |
| KGa2 | 10 | 266 | Yes | No |
| KGa2 | 20 | 266 | Yes | No |
| STx1b | 1 | 532 | Yes | No |
| STx1b | 5 | 532 | Yes | No |
| STx1b | 10 | 532 | Yes | No |
| STx1b | 20 | 532 | Yes | No |
| STx1b | 1 | 266 | No | No |
| STx1b | 5 | 266 | No | No |
| STx1b | 10 | 266 | Yes | No |
| STx1b | 20 | 266 | Yes | Yes |
| SWy2 | 1 | 532 | No | No |
| SWy2 | 5 | 532 | No | No |
| SWy2 | 10 | 532 | Yes | No |
| SWy2 | 20 | 532 | Yes | No |
| SWy2 | 1 | 266 | No | No |
| SWy2 | 5 | 266 | No | No |
| SWy2 | 10 | 266 | No | No |
| SWy2 | 20 | 266 | Yes | Yes |

Table 8: Detection and identification of organics in mineral substrate.

# 10 Conclusion

A collection of aqueous alteration minerals were made into mixtures of varying concentrations with the molecular biosignature stearic acid. These mixtures were examined using Raman spectroscopy to determine if the biosignature could be detected within the mineral matrix. A comparison of the results lead to the conclusion that stearic acid was most easily detected in gypsum. The synthetic gypsum sample contained no transition metals and therefore produces weaker UV absorption than any of the other minerals. Also, even though the gypsum had a small grain size, it would not be as small as the phyllosilicates which have many reported problems with respect to optical spectroscopy due to their extremely small grain sizes [49][68].

The ability to definitively conclude that an organic is present is not the same as identifying which organic is present. A peak at ~2900 $cm^{-1}$ is indicative of aliphatic carbon as almost no minerals have Raman bands in this region, but Vitek et al [34]suggested a minimum of two peaks is required for unambiguous identification of an organic in a mineral mixture. While that may be true for a commercial Raman microscope with well resolved peaks, the less defined peaks observed using our prototype in-situ system would probably require more peaks to actually define organic type (i.e. fatty acid, amino acid) and additional peaks to narrow down to the exact molecule. From this new definition, we can say that the only mineral in which we were clearly able to confirm that stearic acid was the organic present at all concentrations examined was gypsum. It is likely that one could confirm generically that a saturated fatty acid was present in the higher concentration samples of the other minerals. However, determining the length of the aliphatic chain in those samples would be difficult with the green system and impossible with the UV system.

Raman spectroscopy is highly sensitive to organic compounds and is therefore a good method for investigating signs of life on Mars. However, since Raman scattering is a weak phenomenon, any factors that may deteriorate a Raman spectrum need to be avoided. Transition metal bearing minerals have intense and broad absorption in the ultraviolet region of the spectrum due to electronic transitions. It is therefore suggested that UV excitation be avoided for Raman explorations on planetary bodies with high transition metal content. This would include Mars.

Green excitation wavelength allows the avoidance of the most intense electronic absorptions, but is not necessarily the optimal wavelength for planetary exploration investigations. Fluorescence at green excitation is often much larger in magnitude than the Raman intensity. Yan et al[21] showed that fluorescence from extraterrestrial minerals was about two orders of magnitude lower than terrestrial samples of the same minerals. They suggest that the fluorescence problem in mineralogy is mostly due to organic contamination and would not be seen on Mars. Their interpretation is that if strong fluorescence is observed on Mars, that is a good thing because they believe it is indicative of organics. We mention here that the Raman spectra in this study were actually easier to interpret without the fluorescence removed because that process introduced too

many artifacts as the noise associated with the fluorescence was not eliminated during the removal process, nor were sharp changes in the fluorescence background due to the instrument. The noise which cannot be removed is called shot noise.

Certain aqueous alteration minerals in our sample suite definitely allowed for greater detection of biosignatures mixed within them than others. In some of the cases examined, it is suggested that self absorption makes it such that a molecule is saturated with the organics peak at some low concentration. Conversely, with other samples the organic could not even be detected until the concentration reached the maximum of our tested levels.

Organic detection in the Texas montmorillonite was much better than in the Wyoming sample. Note that the reported hematite content in the Texas sample was only 0.7%, while that of the Wyoming sample was 3.4%. We believe that this difference is significant enough to cause the observed difference in organic detection. Titanium content in the two kaolinite samples should have let us observe the effect of another transition metal, but unfortunately the percent content in the two kaolinite samples was too similar for an assessment.

Though phyllosilicates may be one of the optimal minerals for preserving organics by shielding them from destructive ionizing radiation and harmful oxidants, we conclude this study by suggesting that it may be difficult to use Raman spectroscopy to detect preserved organics within these clays.

**This study contributed to the field of planetary exploration and astrobiology in the following ways:**

1. The difficulty of using UV Raman for some planetary minerals was previously known, but no studies had explored the quantum mechanics of the problem. We believe that this is the first study to relate absorption due to charge transfers between orbitals in transition metal coordination complexes to Raman scattering from transition metal-bearing minerals.

2. A previous Raman study had examined stearic acid as a biosignature in a simple mineral matrix [5], but ours was the first Raman study to examine that biosignature in an assortment of complex minerals relevant to Martian astrobiology. The previous study showed that in a simple matrix, a wide range of organics are detectable at concentrations below 1%. However, here we show that using the same UV system as that study, but with our more complex clay mineral substrates, stearic acid is not even detectable at 5% concentration.

3. A previous Raman study had examined a biosignature in a mixture with gypsum [34], but that study used beta carotene which is a much different molecule than stearic acid. While beta carotene is unsaturated and contains no oxygen or hydroxyls, stearic acid is saturated and contains both. That means that stearic acid and beta carotene will be incorporated differently into mineral lattices and onto mineral surfaces.

4. A previous study examined stearic acid as a biosignature in a Mars analogue hydrated sulphate [40], but that was done using laser desorption mass spectroscopy. We believe this to be the first study to examine stearic acid in a hydrated sulphate using UV Raman spectroscopy.

5. A previous study had suggested that after phosphates, clays and sulphates are the next best minerals at preserving organic matter [15]. However, the results of this study showed that detecting organic matter using Raman spectroscopy is generally easier in hydrated sulphates than clays. We believe that this is the first study to make this conclusion.

6. A previous study examined kaolinite with various biosignatures using UV excitation [55]. However, that study used a less robust mixing procedure. We believe that the use of a rotary evaporator allowed our study to examine more homogeneous mixtures and therefore provide more accurate data.

7. Finally, we have shown here that to go beyond simply detecting an organic in a Martian clay and actually identifying a specific fatty acid using UV Raman spectroscopy, there needs to be an organic concentration higher than what is average in Earth clays ($<1\%$). This is likely not possible on the Martian surface due to radiation and oxidation. Therefore, this result further demonstrates that UV Raman investigations may need to explore the Martian subsurface or caves for both detection and identification of biosignatures.

# 11 Future work

We recommend here that further studies in this field carry out the following;

-Testing of similar mixtures with other excitation wavelengths;

-Performing the pre-treatment leaching process Carrier (non-published method, in person conversation) performed at Jet Propulsion Laboratory to remove organic contaminants in their mineral samples;

-Testing more concentrations to find closer approximations of detection limits; and,

-In addition to hydrated sulphates and phyllosilicates, Martian analogue phosphates should be examined as they have been suggested to be the best minerals at preserving organics[15] while also being potentially important to astrobiology due to their phosphorous content.

# 12 Appendices

## 12.1 Raman systems bound for Mars

### 12.1.1 Scanning Habitable Environments with Raman and Luminescence for Organics and Chemicals (SHERLOC)

The SHERLOC instrument plans to have a 50 micron spot size for their 248.9 nm laser. This is much larger than the viewing area of the commercial Raman microscope this study used for our green excitation work, but much smaller than that of the prototype in-situ system used for our UV observations. The SHERLOC team claims that the instrument will be able to detect and classify aqueous alteration minerals with grain sizes down to below 20 microns, but no hard limit has been announced. Unfortunately, almost all phyllosilicates that we are concerned with on Mars have average grain sizes below 2 microns. Since the SHERLOC team has yet to determine a floor for grain size detection, it is still unknown how that instrument will work for these important minerals. Carrier at al [55] have begun some work with the phyllosilicate kaolinite using the prototype SHERLOC instrument, but little data is publicly available at present.

### 12.1.2 SuperCam

The SuperCam team has announced their excitation wavelength of 532 nm, a 1.3 mm spot size at 2 m distance, and a claim that it will work at stand off distances of up to 12 m. We note here that although this current study does not examine fluorescence, both of the Raman instruments for the Mars2020 mission also have fluorescence spectroscopy capabilities. The SuperCam instrument will even have time resolved fluorescence capabilities which when combined with Raman spectroscopy could be an excellent system for biosignature detection[5].

### 12.1.3 Laser Raman Instrument (RLS)

The RLS Raman spectrometer team has announced that their Raman window will be from 150 $cm^{-1}$ to 3800 $cm^{-1}$, the instrument will have a spot size of 50 microns, an average resolution of ~7 $cm^{-1}$, and a spectral precision of $< 1$ $cm^{-1}$. This is a comparable Raman window to our study. It will have the same laser wavelength as SuperCam.

## 12.2 Detailed descriptions of phyllosilicate samples

*Kaolinite KGa1b*

This clay comes from Georgia, USA.. It is a powder that is off-white in colour. By weight, it is almost half silicon dioxide (44.2%), more than a third aluminum hydroxide (39.7%), a small fraction titanium dioxide (1.4%), and the remainder is trace amounts of other metal oxides. Structure:$(Mg_{.02}\ Ca_{.01}\ Na_{.01}\ K_{.01})[Al_{3.86}\ Fe(III)_{.02}Ti_{.11}][Si_{3.83}Al_{.17}]O_{10}(OH)_8$

*Kaolinite KGa2*

This clay also comes from Georgia, USA, but a different county than the KGa1b sample. It too is a powder that is off-white in colour. By weight, it is almost half silicon dioxide (43.9%), more than a third aluminum hydroxide (38.5%), a small fraction titanium dioxide (2.1%), a smaller fraction is hematite (1.0%), and the remainder is trace amounts of other metal oxides. The higher amount of both iron and titanium in this sample should, in theory, mean that it absorbs more in the ultraviolet region than KGa1b. Structure: $[Al_{3.66}\ Fe(III)_{.07}Ti_{.16}][Si_4]O_{10}(OH)_8$

*Note on kaolinite samples:*

The clay minerals society listed KGa1b as a low-defect sample and KGa2 as a high-defect sample. To determine what was meant here we used the x-ray diffraction instrument at the Royal Ontario Museum. The results showed that the low-defect sample had more distinct peaks, meaning that it was more crystalline, while the high-defect sample, though still technically kaolinite, was less crystalline with broader, less defined peaks.

*Montmorillonite SAz2 ( calcium + sodium dominant interlayer cations)*

This clay comes form Arizona, USA.. It is in a solid rock-like form that is white with small specs of purple. By weight, it is more than three fifths silicon dioxide (60.4%), less than a fifth aluminum hydroxide (17.6%), small fractions of magnesium oxide (6.5%), calcium oxide (2.8%), and hematite (1.4%). The remainder is trace amounts of other metal oxides. Structure:$(Ca_{.39}\ Na_{.36}\ K_{.02})[Al_{2.71}\ Mg_{1.11}\ Fe(III)_{.12}\ Mn_{.01}Ti_{.03}][Si_{8.00}]O_{20}(OH)_4$

*Montmorillonite STx-1 (calcium dominant interlayer cations)*

This clays comes from Texas, USA. It is a white powder. By weight, it is more than two thirds silicon dioxide (70.1%), less than a fifth aluminum hydroxide (16.0%), small fractions of magnesium oxide (3.7%), calcium oxide (1.6%), and hematite (0.7%). The remainder is trace amounts of other metal oxides. Trace amounts of carbonate were found in it. Structure:$(Ca_{.27}\ Na_{.04}\ K_{.01})[Al_{2.41}\ Fe(III)_{.09}\ Mg_{.71}Ti_{..03}][Si_8]O_{20}(OH)_4$

*Montmorillonite Sca-3 (calcium + sodium + magnesium dominant interlayer cations)*

This clay comes from California, USA. It is a solid rock like form that is white and light purple. By weight, it is more than half silicon dioxide (52.8%), less than a fifth aluminum hydroxide (15.7%), small fractions of magnesium oxide (8.0%), calcium oxide (1.0%), sodium oxide (0.9%), and hematite (1.1%). The remainder is trace amounts of other metal oxides. Structure:$(Mg_{.45}\ Ca_{.15}\ Na_{.26}\ K_{.01})[Al2.55\ Fe(III)_{.12}\ Mg_{1.31}\ Ti_{.02}\ ][Si_{7.81}\ A_{l.19}]O_{20}(OH)_{\ 4}$.

*Montmorillonite SWy-2 (sodium + calcium dominant interlayer cations)*

This clay comes from Wyoming, USA. It is a blue-ish-grey powder. By weight, it is more than three fifths silicon dioxide (62.9%), less than a fifth aluminum hydroxide (19.6%), small fractions of magnesium oxide (3.1%), calcium oxide (1.7%), sodium oxide (1.5%), and hematite (3.4%). Though that hematite content is a small percentage of the whole structure, it a significant amount in terms of what could affect optical spectroscopy. The remainder is trace amounts of other metal oxides. Trace amounts of carbonate were found

in it. Structure:$(Ca_{.12}\ Na_{.32}\ K_{.05})[Al_{3.01}\ Fe(III)_{.41}\ Mn_{.01}\ Mg_{.54}Ti_{.02}][Si_{7.98}\ Al_{.02}]O_{20}(OH)_4$

*Notes on montmorillonite samples:*

These samples have a significantly higher surface area than the kaolinites and also a greater capacity to exchange cations. Both of these features could make organics bind more easily to the mineral.

*Nontronite NG-1*

This clay comes from Hohen Hagen, Germany. It is a solid rock like form that is dark brown in colour. By weight, the nontronite is less than half silicon dioxide (45.8%), about a third hematite (32.2%), less than a tenth aluminum hydroxide (5.9%), small fractions of magnesium oxide (1.0%), calcium oxide (2.0%), and sodium oxide (0.9%). The remainder is trace amounts of other metal oxides. Structure:$(Mg_{.15}\ Ca_{.32}\ Na_{.01}\ K_{.03})[Fe(III)_{3.75}\ Al_{.17}\ Mg_{.08}Ti_{.01}][Si_{7.08}\ Al_{.92}]O_{20}(OH)_4$

*Nontronite NAu-1*

This clay comes from South Australia, Australia. It is a solid rock like form that is a bright yellowish-green. By weight, it is more than half silicon dioxide (53.3%), about a third hematite (34.2%), approximately a tenth aluminum hydroxide (10.2%), and a small fraction of calcium oxide (3.5%). The remainder is trace amounts of other metal oxides. Structure:$(Cation+_{1.0})[Si_{7.00}\ Al_{1.00}][Al_{.58}\ Fe_{3.38}\ Mg_{.05}]\ O_{20}(OH)_4$.

*Nontronite NAu-2*

This clay also comes from South Australia, Australia, but it is unclear whether it comes from area as sample NAu-1 as this is a large geographical region. It is a solid rock like form that is a light yellowish-brown. By weight, it is more than half silicon dioxide (57.0%), about two fifths hematite (37.4%), less than a twentieth aluminum hydroxide (3.4%), and a small fraction of calcium oxide (2.7%). The remainder is trace amounts of other metal oxides. Structure:$(Cation+_{.97})[Si_{7.57}\ Al_{.01}\ Fe_{.42}][Al_{.52}\ Fe_{3.32}\ Mg_{.7}]O_{20}(OH)_4$

*Notes on nontronite samples:*

The values given for the % composition breakdowns of the nontronite are for the nontronite components of the samples. These bulk samples provided by the Clay Minerals Society actually contain a large amount of crystalline quartz ($<$15% for the Australian samples, $>$ 75% for the German sample). Because of the high amount of quartz crystals in the sample, when using the small spot size Raman microscope at the Royal Ontario Museum, multiple sites had to be examined before finding one that was actually nontronite.

## 12.3 Additional information concerning the induced dipole moment and molecular polarizability tensor

If a neutral molecule is placed in an electric field, one might incorrectly guess that nothing would happen. The molecule may be neutral overall, but there is a negatively charged electron cloud and positively charged nuclei. The charged particles experience a force from the field. The nuclei are pushed in the direction of the field, while the electron cloud is pushed the opposite way. The two

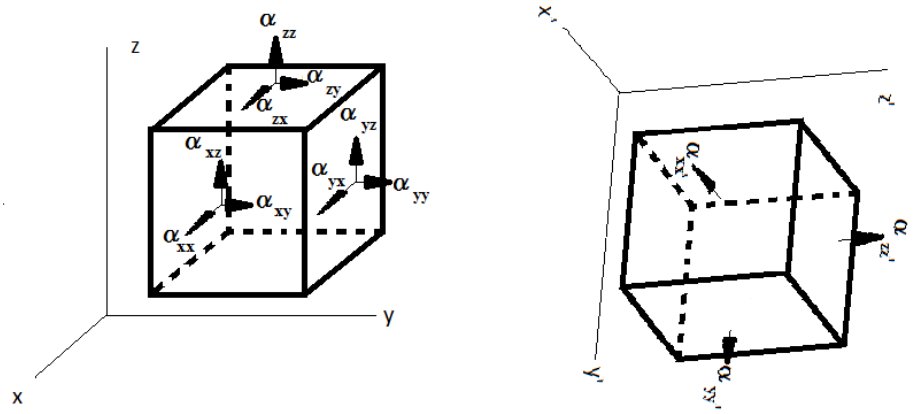


Figure 99: Polarizability tensor. a) 3x3 tensor with 9 elements, b) 3x3 tensor diagonalized with 3 elements in new coordinate systems

movements occur while the mutual attraction of the two charged regions draw them back together. The equilibrium position would result in there being some separation between the centre of the electron cloud and the centre of the nuclei.

An electric dipole moment, p, is a separation of positive and negative charge in a charge distribution. It has units of C·m (Coulomb-metre), is a vector, and is calculated as follows

$$p(x, y, z) = q \cdot d(x, y, z)$$

where d is the displacement vector from negative to positive charges and q is a positive scalar measured in coulombs.

In a molecule or crystal this polarity can form instantaneously as a dynamic response to an incident electric field. The name of this dynamic response is called the molecular polarizability. Molecules and crystals may polarize more easily along different directions. Therefore, the proportionality factor between the incident electric field and the induced dipole is a tensor.

$$P(x, y, z) = \tilde{\alpha} E(x, y, z)$$

The polarizability tensor,$\tilde{\alpha}$, has units of either $\mathrm{C \cdot m^2 \cdot V^{-1}}$ or $\mathrm{A^2 \cdot s^4 \cdot kg^{-1}}$.

It was mentioned in chapter two that a molecular polarizability tensor is symmetric and can therefore be diagonalized (as in the tensor shown above), leading to only three elements in a new coordinate system. A visual representation of this conversion is shown in Figure 104.

## 12.4 York University 266 nm Raman system

The system described in Eshelman et al [2] uses an ALPHALAS Nd:YAG laser (1064 nm frequency quadrupled for 266 nm) with a 0.6 ns pulse width. When operated at a pulse repetition frequency of 5 kHz, this laser provides ~1.5 mW of power at the sample location. The beam does not have a Gaussian profile. The shape is slightly off from elliptical, with a long axis at the sample of ~ 1 mm and a short axis of ~ 0.6 mm. Though this system has the capability to incorporate a microscope objective, it was decided that it would not be used so that the viewing region was as homogeneous as possible.

A quartz beam sampler causes a small amount of reflected light right out of the laser to be directed onto the gating photodiode. This unit sends a voltage signal to the CCD to initiate gate opening. The main portion of the laser beam passes through the quartz sampler and onto a path of many mirrors to extend the path length of the light before hitting the sample. This path length allows enough delay time for the gate to open right before the collected scattered light from the sample is incident upon the CCD.

After the incident light goes through the mirror path length, it is reflected 90 degrees using a dichroic beamsplitter and then onto the sample. One hundred and eighty degree scattered light then returns back to this splitter. A mirror then deflects the scattered light into the collection optics where it passes through an edge filter, cutting off Rayleigh scattered light while allowing through Raman scattered light.

Fibre optics bring the collected light to the Shamrock 163 spectrograph. Light passes through a slit and onto a mirror which collimates the light. The collimated light is then directed at a 3600 lines/mm diffraction grating where it is wavelength separated and directed at a focusing mirror. Focused, wavelength separated light is then incident upon the camera, an Andor iStar DH334t.

The Andor iStar camera consumes 85 watts of power continuously. It contains a charge coupled device (CCD) sensor, a gated image intensifier tube, a digital delay generator, and a thermoelectric cooling interface. The CCD is a semiconductor with a two-dimensional array of photo-sensors (pixels). There are a total of 1024 x 1024 pixels. Each pixel has an effective area of 19.5 x 19.5 microns. The effective area of the CCD is 13.3 x 13.3 mm.

The gated image intensifier amplifies the intensity of the incoming signal. It has three main components including the photocathode, the micro-channel plate, and the output phosphor screen. Depending on the quantum efficiency of the photocathode, it may generate a photoelectron when a photon strikes its surface. An electric field accelerates this photoelectron across a gap to the micro-channel plate. The potential difference between the photocathode and the micro-channel plate can be toggled between two levels, one which allows photoelectrons to leave the photocathode and one that does not. This toggling can be done rapidly and is how the gating of the camera is controlled. The micro-channel plate has such a large potential difference across it that incident photoelectrons produce secondary electrons (impact ionization) which are then incident on the phosphor. By varying the potential difference across the plates,

the gain of the intensifier can be adjusted. The phosphor converts the incident electron pattern into a light pattern. This light pattern can then be detected by the CCD as the output of the image intensifier is coupled to the CCD sensor via a fibre optic cable.

A option for the CCD called full vertical binning combines the charges from each column of pixels in the 1024 x 1024 matrix to give one single value per column. This process which benefits from noise averaging, turns the CCD chip into a linear image sensor which is used for spectroscopy applications. Light falls on an element and photoelectrons are produced. The resulting electrons are confined to their pixel. The charge is then transferred off the chip, one row at a time, to the shift register. The shift register transfers the charge packets to the amplifier. The amplifier output then goes to the analog to digital converter (ADC). This component converts the analog signal into a 16-bit binary number that is sent to the laptop running Andor Solis © software.

## 12.5 No deconvolution of C-H stretching region

It is assumed that the output spectrum from a detector is a convolved signal of the actual spectrum and a response function of the system. Deconvolution is a procedure to resolve a spectrum into individual bands. To do so properly one needs to estimate both the number of bands in the convolved signal and their bandwidths. However, as Vandenabeele stated[3].

> "When several bands are overlapping and shoulders are present, it is impossible to determine the exact band position."

The C-H stretching region for stearic acid is definitely an overlap of many bands. In the green Raman spectrum in Figure 13, there are at least 4 major peaks, multiple shoulders, and a significant asymmetry to the main large peak. Since the C-H region includes stretches from methyl groups, methylene groups, overtone deformation bands (both regular and Fermi resonance), and finally, low intensity combination bands, there is no way to know exactly how many bands are producing the final convolved overlapping band. The C-H stretching bands alone should account for over a third of the 162 first order vibrations in a stearic acid Raman signal. Theoretically, there could be close to 100 bands in the region from 2700 $cm^{-1}$ to 3100 $cm^{-1}$, with the majority of these between 2800 $cm^{-1}$ to 3000 $cm^{-1}$. Though true that many are degenerate, there is still a large number of different peaks contributing the observed band.

# References


[1] Mars Exploration Program Analysis Group (MEPAG). Mars science goals, objectives, investigations, and priorities: 2015 version. http://mepag.nasa.gov/reports.cfm., June 2015.

[2] E. Eshelman, M.G. Daly, G. Slater, P. Dietrich, and J.-F. Gravel. An ultraviolet raman wavelength for the in-situ analysis of organic compounds relevant to astrobiology. *Planetary and Space Science*, 93-94:65–70, 2014.

[3] Peter Vandenabeele. *Practical Raman Spectroscopy: An Introduction*. Eiley, 2013.

[4] Peter J. Larkin. *IR and Raman Spectroscopy: Principles and Spectral Interpretation*. Elsevier, 2011.

[5] Evan Eshelman. *Stand-off detection of organic compounds on Mars using ultraviolet Raman spectroscopy and Time-resolved laser-induced fluorescence*. PhD thesis, York University, 2016.

[6] N. Krishnamurthy and V. Soots. Raman spectrum of gypsum. *Canadian Journal of Physics*, 49, 1970.

[7] Chemical Education Digital Library. Chemed digital library. http://www.chemeddl.org/, 2016.

[8] R.T. Downs and M. Hall-Wallace. The american mineralogist crystal structure database. *American Mineralogist*, 88:247–250, 2003.

[9] Ed Cloutis and Matt Izawa. Data master sedimentary. Excel file of reflectance spectral data for sedimentary minerals. In person permission to utilize this data set.

[10] Janice L. Bishop, Damien Loizeau, Nancy K. McKeown, Lee Saper, M. Darby Dyar, David J. Des Marais, Mario Parente, and Scott L. Murchie. What the ancient phyllosilicates at mawrth vallis can tell us about possible habitability on early mars. *Planetary and Space Science*, 86:130–149, 2013.

[11] A. S. Burton, M. P. Callahan, J. E. Elsila, E. M. Baker, K. E. Smith, D. P. Glavin, and J. P. Dworkin. Amino acids from mars? clues from the martian shergottite roberts massif (rbt) 04262. *44th Lunar and Planetary Science Conference*, 2013.

[12] D. Catling and D. Bergsman. Chemical disequilibrium in planetary atmospheres as a way to look for life or its absence. *Goldschmidt Conference*, 2014. California.

[13] F. Rull. The laser raman instrument (rls) for exomars 2018 mission and the scientific operation on mars. *Eighth International conference on Mars*, 2014.

[14] Lujendra Ojha, Marry Beth Wilhelm, Scott L. Murchie, Alfred S. McEwen, James J. Wray, Jennifer Hanley, Marion Masse, and Matt Chojnacki. Spectral evidence for hydrated salts in recurring slope lineae on mars. *Nature Geoscience*, 8:829–832, 2015.

[15] Roger E. Summons, Jan P. Amend, David Bish, Roger Buick, George D. Cody, David J. Des Marais, Gilles Dromart, Jennifer L. Eigenbrode, Andrew H. Knoll, and Dawn Y. Sumner. Preservation of martian organic and environment record: Final report of the mars biosignature working group. *Astrobiology*, 11(2), 2011.

[16] D. N. Thomas and G. S. Dieckmann. Antarctic sea ice–a habitat for extremophiles. *Science*, 295(5555):641–644, 2002.

[17] L. Rothschild and R. Mancinelli. Life in extreme environments. *Nature*, 409:1092–1101, 2001.

[18] M. Skulinova, C. Lefebvre, P. Sobrona, E. Eshelman, M. Daly, J.-F. Gravel, J.-F. Cormier, F. Chateauneuf, G. Slater, W. Zhenga, A. Koujeleva, and R. Leveille. Time-resolved stand-off raman spectroscopy for planetary exploration. *Planetary and Space Science*, 92:88–100, 2014.

[19] Los Alamos National Laboratory. Los alamos laser selected for 2020 mars mission. Press release, July 2014.

[20] L.W. Beegle, R. Bhartia, L. DeFlores, M. Darrach, R.D. Kidd, W. Abbey, S. Asher, A. Burton, S. Clegg, P.G. Conrad, K. Edgett, B. Ehlmann, F. Langenhorst, M. Fries, W. Hug, K. Nealson, J. Popp, P. Sobronvand A. Steele, R. Wiens, and K. Williford. Sherloc: Scanning habitable environments with raman & luminescence for organics & chemicals, an investigation for 2020. *45th Lunar and Planetary Science Conference*, 2014.

[21] Y. Yan, Alian Wang, and J. Wei. Shifted excitation raman differentiated spectroscopy (serds) for planetary surface exploration. *47th Lunar and Planetary Science Conference*, 2016.

[22] A.S. Rivkin, E.L. Volquardsen, and B.E. Clark. The surface composition of ceres: Discovery of carbonates and iron rich clays. *Icarus*, 185:563–567, 2006.

[23] A. Ali, E.C. Stitler Jr., D. Chomray, B.R. Rowec, and C. Puzzarinid. Organic chemistry in titans upper atmosphere and its astrobiological consequences: Views towards cassini plasma spectrometer (caps) and ion neutral mass spectrometer (inms) experiments in space. *Planetary and Space Science*, 109-110:46–63, 2015.

[24] James P. Ferris. Genesis: Rocks, minerals, and the geochemical origin of life: Mineral catalysis and prebiotic synthesis: Montmorillonite-catalyzed formation of rna. *Elements*, 1:145–149, 2005.

[25] John I. Hedges, Feng Sheng Hu, Allan H. Devol, Hilairy E. Hartnett, Elizabeth Tsamakis, and Richard G. Keil. Sedimentary organic matter preservation: A test for selective degradation under oxic conditions. *American Journal of Science*, pages 529–555, 1999.

[26] John I. Hedges and Richard G. Keil. Sedimentary organic matter preservation: an assessment and speculative synthesis. *Marine Chemistry*, 49:81–115, 1995.

[27] Birgit Kohler, Arieh Singer, and Peter Stoffers. Biogenic nontronite from marine white smoker chimneys. *Clays and Clay Minerals*, 42(6):689–701, 1994.

[28] Jean-Pierre Bibring, Yves Langevin, Aline Gendrin, Brigitte Gondet, Francois Poulet, Michel Berthe, Alain Soufflot, Ray Arvidson, Nicolas Mangold, John Mustard, and P. Drossard. Mars surface diversity as revealed by the omega/mars express observations. *Science*, 307(5715):1576–1581, 2005.

[29] G. Klingelhofer, R. V. Morris, B. Bernhardt, C. Schroder, D. S. Rodionov, P. A. de Souza Jr., A. Yen, R. Gellert, E. N. Evlanov, B. Zubkov, J. Foh, U. Bonnes, E. Kankeleit, P. GÃŒtlich, D. W. Ming, F. Renz, T. Wdowiak, S. W. Squyres, and R. E. Arvidson. Jarosite and hematite at meridiani planum from opportunity's mossbauer spectrometer. *Science*, 306:1740–1745, 2005.

[30] Nancy K. McKeown, Janice L. Bishop, E.Z. Noe Dobrea, B.L. Ehlmann, M. Parente, J.F. Mustard, S.L. Murchie, G.A. Swayze, J.-P. Bibring, and E.A. Silver. Characterization of phyllosilicates observed in the central marwrth vallis region, mars, their potential foformation processes and implications for past climate. *Journal of geophysical research*, 114(E00D10):1–20, 2009.

[31] Partick Thollot, Nical Mangold, Veronique Ansan, Stephane Le Mouelic, Ralph E. Milliken, Janice L. Bishop, Catherine M. Weitz, Leah H. Roach, John F. Mustard, and Scott L. Murchie. Most mars minerals in a nutshell: Various alteration phases formed in a single environment in noctis labrynthus. *Journal of geophysical research*, 117(E00J06):1–28, 2012.

[32] Howard Anton and Chris Rorres. *Elementary Linear Algebra: Applications Version*. John Wiley and Sons, 2005.

[33] Jie Wei, Alian Wang, Yanli Lu, Kathryn Connor, Alex Bradley, Craig Marshall, and Andrew Steele. The detection of biosignatures by laser raman spectroscopy for mars exploration. *International GeoRaman Conference*, 2014.

[34] Petr Vtikek, Jan Jehlicka, H.G. Edwards, and K. Osterrothova. Identification of beta-carotene in an evaporitic matrix - evaluation of raman

spectropscopic analysis for astrobiological research on mars. *Analytical bioanalysis and chemistry*, 393:1967–1975, 2009.

[35] Alian Wang, L.A. Haskin, S. W. Squyres, B.L. Jolliff, L. Crumpler, Ralf Gellert, C. Schroder, K. Herkenhoff, J. Hurowitz, N.J. Tosca, W. H. Farrand, R. Anderson, and A.T. Knudson. Sulfate deposition in subsurface regolith in gusev crater, mars. *Journal of Geophysical Research*, 111(E02S17):1–19, 2006.

[36] M. H. Hecht, S. P. Kounaves, R. C. Quinn, S. J. West, S. M. M. Young, D. W. Ming, D. C. Catling, B. C. Clark, W. V. Boynton, J. Hoffman, L. P. DeFlores, K. Gospodinova, J. Kapit, and P. H. Smith. Detection of perchlorate and the soluble chemistry of martian soil at the phoenix lander site. *Science*, 325(5936):64–67, 2009.

[37] G.E Cushing, T.N. Titus, J. J. Wynne, and P. R. Christensen. Themis observes possible cave skylights on mars. *Lunar and Planetary Science Conference XXXVIII*, 2007.

[38] C. A. Drost, J. J. Wynne, M. G. Chapman, J. S. Kargel, T. N. Titus, and R. S. Toomey. Remotely sensed cave detection on earth and mars. *Lunar and Planetary Science Conference XXXVII*, 2006.

[39] Jonathan I. Lunine. *Astrobiology: A Multidisciplinary Approach*. Pearson Addison Wesley, 2005.

[40] Charles Doc Richardson. *Bio/organic compound detection using sodium sulfate minerals: Implications in the search for life on Mars and Europa*. PhD thesis, University of Montana, 2010.

[41] Eva Weber and Boaz Pokroy. Intracrystalline inclusions within single crystalline hosts: from biomineralization to bio-inspired crystal growth. *CrystEngComm*, 17:5873–5883, 2015.

[42] Jack D. Farmer and David J. Des Marais. Exploring for a record of ancient martian life. *Journal of Geophysical Research*, 104(E11):26977–26995, 1999.

[43] O.V Lotareva and A. A. Prozorov. Effect of the clay minerals montmorillonite and kalonite on the genetic transtransform of competent bacillus subtilis cells. *Microbiology*, 69(5):571–574, 2000.

[44] Mumma, M.J. and Villaneuva, G.L. and Campbell, R. and Lyke, J. and Conrad, A. and Encrenaz, T., and Hartogh, P. and Kauefl, U. Tracing the origin of methane and water on mars: Mapping regions of active release at ultra-high spatial resolution using keck and vlt under ao control. *American Astronomical Society, DPS meeting 41*, (id. 44.02), 2009.

[45] C. R. Webster, P. R. Mahaffy, S. K. Atreya, G. J. Flesch, L. E. Christensen, and K. A. Farley. Measurements of mars methane at gale crater by the sam tunable laser spectrometer on the curiosity rover. *44th Lunar and Planetary Science Conference*, 2013.

[46] Schuerger, A., and Moores, J.E. and Clausen, C. and Barlow, N. and Britt, D. Methane from uv-irradiated carbonaceous chondrites under simulated martian conditions. *Journal of geophysical research*, 117(E08007), 2012.

[47] C. Freissinet, D. P. Glavin, P. R. Mahaffy, K. E. Miller, J. L. Eigenbrode, R. E. Summons, A. E. Brunner, A. Buch, C. Szopa, P. D. Archer, H. B. Franz, S. K. Atreya, W. B. Brinckerhoff, M. Cabane, P. Coll, P. G. Conrad, D. J. Des Marais, J. P. Dworkin, A. G. Fairen, P. Francois, J. P. Grotzinger, S. Kashyap, I. L. ten Kate, L. A. Leshin, C. A. Malespin, M. G. Martin, F. J. Martin-Torres, A. C. McAdam, D. W. Ming, R. Navarro-Gonzalez, A. A. Pavlov, B. D. Prats, S. W. Squyres, A. Steele, J. C. Stern, D. Y. Sumner, B. Sutter, M.-P. Zorzano, and the MSL Science Team. Organic molecules in the sheepbed mudstone, gale crater, mars. *Journal of Geophysical Research: Planets*, 120(3):495–514, 2015. 2014JE004737.

[48] Ray Frost, Thu Ha Tran, and Janos Kristof. Raman spectroscopy of the lattice region of kaolinite and its intercalates. *Vibrational Spectroscopy*, 13:175–186, 1997.

[49] Frank Friedrich. *Spectroscopic investigations of delaminated and intercalated phyllosilicates*. PhD thesis, Karlsruher Mineralogische und Geochemische Hefte: Schriftenreihe des Instituts fur Mineralogie und Geochemie, 2005.

[50] D. Hamilton, M.G. Daly, E.A. Cloutis, and K. Tait. A raman spectroscopy comparison of an iron-bearing and a non-iron-bearing sulphate at both green and uv excitation wavelengths. *47th Lunar and Planetary Science Conference*, 2016.

[51] Zongcheng Ling, Fengke Cao, Yuheng Ni, Zhongchen Wu, Jiang Zhang, and Bo Li. Raman spectroscopic study of the k-na jarosite solid solutions. *46th Lunar and Planetary Science Conference*, 2015.

[52] Ray L. Frost, Rachael-Anne Willis, Matt L. Weier, and Wayde N. Martens. Comparison of the raman spectra of natural and synthetic k- and nna-jarosite at 298 and 77k. *Journal of Raman Spectroscopy*, 36:435–444, 2005.

[53] Clay Minerals Society. Source clay physical/chemical data. Website (http://www.clays.org/SOURCE

[54] Tanya Harrison. Experimental vnir reflectance spectroscopy of gypsum dehydration: Investigating the gypsum to bassanite transition. *American Mineralogist*, 97:598–609, 2012.

[55] B. Carrier, L. Beegle, R. Bhartia, and W. J. Abbey. Measurement of uv fluorescence and raman signatures of organic compounds in the subsurface of mars relevant minerals to constrain detection depth for the sherloc mars 2020 instrument. *47th Lunar and Planetary Science Conference*, 2016.

[56] M. Gargaud, R. Amils, and et al. *Encyclopedia of Astrobiology*. Springer, 2015.

[57] Kevin W. Plaxco and Michael Gross. *Astrobiology: A brief Introduction, 2nd edition*. John Hopkins University Press, 2011.

[58] J.L. Beare-Rogers, A. Deiffenbacher, and J.V. Holm. Lexicon of lipid nutrition (iupac technical report). *Pure and Applied Chemistry*, 73(4):685–744, 2009.

[59] Walter P. Gibble and Jr. Edwin B. Kurtz. The synthesis of long-chain fatty acids from acetatein flax, linum usitatissimum l.l. *Archives of biochemistry and biophysics*, 64:1–5, 1956.

[60] C. Doc Richardson, Nancy W. Hinman, Timothy R. McJunkin, J. Michelle Kotler, and Jill R. Scott. Exploring biosignatures associated with thenardite by geomatrix-assisted laser desorption/ionization fourier transform ion cyclotron resonance mass spectrometry. *Geomicrobiology Journal*, 25:432–330, 2008.

[61] M. Saggu, J. Liu, and A. Patel. Identification of subvisible particles in biopharmaceutical formulations using raman spectroscopy provides insight into polysorbate 20 degradation pathway. *Pharmaceutical Research*, 32(9):2877–2888, 2015.

[62] Roger G. Burns. Ferric sulfates on mars. *Journal of geophysical research*, 92(B4):E570–E574, 1987.

[63] Alian Wang, Randy L. Korotev, B.L. Jolliff, L.A. Haskin, L. Crumpler, W. H. Farrand, K. E. Herkenhoff Jr., A.G. Kusack, J.A. Hurowitz, and N.J. Tosca. Evidence of phyllosilicates in wooly patch, an altered rock encountered at west spur, columbia hills, by the spirit rover in gusev crater, mars. *Journal of geophysical research*, 111(E02S16):1–22, 2006.

[64] F. Poulet, N. Mangold, D. Loizeau, J.P. Bibring, Y. Langevin, J. Michalski, and B. Gondet. Abundance of minerals in the phyllosilicate-rich units on mars. *Astronomy and Astrophysics*, 487:L41–L44, 2008.

[65] Stanley L. Miller. A production of amino acids under possible primitive earth conditions. *Science*, 117(3046):528–529, 1953.

[66] Andrew Aubrey, H. James Cleaves, John H. Chalmers, Alison M. Skelley, Richard A. Mathies, Frank J. Grunthaner, Pascale Ehrenfreund, and Jeffrey L. Bada. Sulfate minerals and organic compounds on mars. *Geology*, 34(5):357–360, 2004.

[67] W.G. Kong, M.P Zheng, F.J. Kong, and W.X. Chen. Sulfate-bearing deposits at dalangtan playa and their implication for the formation and preservation: of maritian salts. *American Mineralogist*, 99:283–290, 2014.

[68] William D. Nesse. *Introduction to Optical Mineralogy*. Oxford University Press, 2004.

[69] Ewen Smith and Geoffrey Dent. *Modern Raman Spectroscopy: A Practical Approach*. Wiley, 2005.

[70] George Robinson. *Minerals*. Simon and Schuster, 1994.

[71] B. E. McKeeby, S. Mahmood, M. Lowe, and J. P. Greenwood. An investigation of jarosite and associated alteration mineralogy in martian meteorite roberts massif 04262 using micro-raman spectroscopy. *47th Lunar and Planetary Science Conference*, 2016.

[72] Ray L. Frost, Rachael-Anne Willis, Matt L. Weier, and Wayde Martens. A raman spectroscopic study of selected natural jarosites. *Spectrochimica Acta*, 63:1–8, 2006.

[73] Yang Liu and Alian Wang. Dehydration of na-jarosite, ferricopiapite, and rhomboclase at termperatures of 50 and 95 degrees c: Implications for martian ferric sulfates. *Spectroscopy*, pages 493–500, 2015.

[74] Keiko Sasaki, Osamu Tanaike, and Jidetaka Konno. Distinction of jarosite-group compounds by raman spectroscopy. *Canadian Mineralogist*, 36:1225–1235, 1998.

[75] Ming Wu, Mark Ray, K. Hang Fung, Mark W. Ruckman, David Harder, and Arthur J. Sedlacek. Stand-off detection of chemicals by uv raman spectroscopy. *Applied spectroscopy*, 54(6):800–806, 2000.

[76] Roger G. Burns. *Mineralogical applications of crystal field theory*. Cambridge University Press, 2nd edition edition, 1993.

[77] Herve Chamley. *Clay Sedimentology*. Springer, 1989.

[78] Ursula Johansson, Ray Frost, Willis Forsling, and Theo Kolprogge. Raman spectroscopy of the kaolinite hydroxyls at 77 k. *Applied spectroscopy*, 52(10), 1998.

[79] Ray Frost. Fourier transform raman spectroscopy of kaolinite, dickite and halloysite. *Clays and Clay Minerals*, 43(2), 1995.

[80] Quant T. Nguyen and Donald G. Baird. Preparation of polymer-clay nanocomposites and their properties. *Advances in Polymer Technology*, 25:270–285, 2006.

[81] Alian Wang, John J. Freeman, and Bradley L. Jolliff. Understanding the raman spectral features of phyllosilicates. *Journal of Raman Spectroscopy*, 2015.

[82] C. Rinaudo, M. Roz, V. Boero, and M. Franchini-Angela. Ft-raman spectroscopy on several di- and tri- octahedral t-o-t phyllosilicates. *Neues Jahrbuch fÃŒr Mineralogie - Monatshefte*, 12:537–554, 2004.

[83] Ray L. Frost and Llew Rintoul. Lattice vibrations of montmorillonite: an ft raman and x-ray diffraction study. *Applied clay science*, 11:171–183, 1996.

[84] C. Che, S. Parvez, and T.D Glotch. Spectroscopic study of biosignatures in clay-rich sediments: Implications for martian astrobiological exploration. *47th Lunar and Planetary Science Conference*, 2016.

[85] Ray L. Frost and J. Theo Kloprogge. Vibrational spectroscopy of ferruginous smectite and nontronite. *Spectrochimica Acta*, 56:2177–2189, 2000.

[86] David Des Marais. Preservation of evidence of ancient environment and life on mars. 4th MSL Landing Site Workshop, 2010.

[87] K. McCormack, E. Cloutis, J.F. Bell III, L. Stewart, L Kaletzke, and M. Craig. Determining mineral composition in the ultraviolet spectral region from 200 to 400 nanometres. *Lunar and Planetary Science XXXVII*, 2006.

[88] E. Cloutis, Kaitlyn A. McMormack, James F. Bell, Amanda R. Hendrixc, Daniel T. Baileya, Michael A. Craig, Stanley A. Mertzmand, Mark S. Robinsone, and Miriam A. Rinere. Ultraviolet spectral reflectance properties of common planetary minerals. *Icarus*, 197:321–347, 2008.

[89] Carlton C. Allen, Richard V. Morris, Karen M. Jager, D. C. Golden, David J. Lindstrom, Marilyn M. Lindstrom, and John P. Lockwood. Martian regolith simulant jsc mars-1. *Lunar and Planetary Science XXIX*, 1998.

[90] Alan Heyduk. Chemistry 107: Inorganic chemistry uc irvine opencourseware. Youtube, 2014.

[91] D. Ray. Co-ordination chemistry (chemistry of transition elements) department of chemistry and biochemistry, iit kharagpur. Youtube, 2014.

[92] Brian Henderson and Ralph H. Bartram. *Crystal-field engineering solid-state laser materials*. Cambridge University Press, 2005.

[93] Roger G. Burns. Intervalence ttransition in mixed valence minerals of iron and titanium. *Annual Review of Earth and Planetary Science*, 9:345–383, 1981.

[94] Bruce Hapke. *Theory of Reflectance and Emittance Spectroscopy*. Cambridge University Press, 2012.

[95] Jeffrey K. Wagner, Bruce W. Hapke, and Eddie N. Wells. Atlas of reflectance spectra of terrestrial, lunar, and meteoritic powders and frosts ffrom 92 to 1800 nm. *Icarus*, 69:14–28, 1987.

[96] Ed Wells and Bruce W. Hapke. Lunar soil: Iron and the titanium bands in the glass fraction. *Science*, 195(4282):977–979, 1977.

[97] Bruce M. Loeffler, Roger G. Burns, K. H. Johnson, J. A. Tossell, and D.J. Vaughan. Charge transfer in lunar materials: Interpretation of ultraviolet-visible spectral properties of the moon. *Proceedings of the 5th Lunar Conference*, 3:3007–3016, 1974.

[98] Sherman and Vergo. Optical (diffuse reflectance) and mossbauer spectroscopic studies of nontronite and related fe-bearing smectites. *American Mineralogist*, 73:1346–1354, 1988.

[99] J. F. Bell and T.M Ansty. High spectral resolution uv to near-ir observations of mars using hst/stis. *Icar*, 191:581–602, 2007.

[100] Rudi Heryanto, Masitah Hasan, Ezzat Chan Abdullaha, and Andri Cahyo Kumoro. Solubility of stearic acid in various organic solvents and it s prediction using non-ideal solution models. *ScienceAsia*, 33:469–472, 2007.